NASA CR-72712
PWA FR-3704
VOLUME III

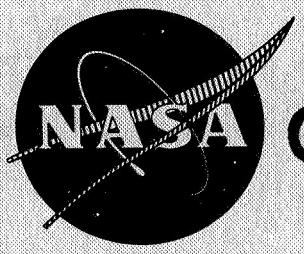

FINAL REPORT

STUDY OF INDUCER LOAD AND STRESS

By: L. L. Coons, J. M. Reddecliff,
A. E. Wemmell, and W. E. Young

Pratt & Whitney Aircraft
FLORIDA RESEARCH AND DEVELOPMENT CENTER
BOX 2691, WEST PALM BEACH, FLORIDA 33402

Prepared for
NATIONAL AERONAUTICS
AND
SPACE ADMINISTRATION

NASA Lewis Research Center
Contract NAS3-11216

1. Report No.	2. Government Accession No.	3. Recipient's Catalog No.
NASA CR 72712 Vol. III		

4. Title and Subtitle	5. Report Date
Study of Inducer Load and Stress	November, 1972
	6. Performing Organization Code

7. Author(s)	8. Performing Organization Report No.
L. L. Coons, J. M. Reddecliff, A. E. Wemmell, W. E. Young	PWA FR-3704 Vol. III
	10. Work Unit No.

9. Performing Organization Name and Address	11. Contract or Grant No.
Pratt & Whitney Aircraft Florida Research and Development Center West Palm Beach, Florida 33402	NAS 3-11216
	13. Type of Report and Period Covered
12. Sponsoring Agency Name and Address	Contractor Report
National Aeronautics and Space Administration Washington, D.C. 20546	14. Sponsoring Agency Code

15. Supplementary Notes

Project Manager, Dean D. Scheer, Chemical Propulsion Division,
NASA Lewis Research Center, Cleveland, Ohio

16. Abstract

An analytical and experimental investigation into the effects of blade tip clearance on inducer performance and of leading edge sweepback on both blade pressure loading and performance was performed. Tip clearance flow was represented with a vortex flow model and measured data from previous inducer tests at three clearances were correlated with model predictions. A leading edge model was added to an existing inducer internal flow analysis, tests with two sweepbacks were conducted, and blade pressure and performance predictions were correlated with measured data.

17. Key Words (Suggested by Author(s))		18. Distribution Statement
Inducer	Hydrodynamic Load	Unclassified - Unlimited
Hydrodynamics	Sweepback	
Tip Clearance	Internal Flow	
Cavitation	Blade Loading	

19. Security Classif. (of this report)	20. Security Classif. (of this page)	21. No. of Pages	22. Price*
Unclassified	Unclassified	134	$3.00

* For sale by the National Technical Information Service, Springfield, Virginia 22151

FOREWORD

This volume (III) documents the work performed under Contract NAS3-11216, Modification Number 3, during the period February 1971 through June 1972. The work is additional to that reported in Volume I. Volume II, Computer Programs, is being updated and reissued with this volume.

The work was sponsored by the Lewis Research Center, National Aeronautics and Space Administration, Cleveland, Ohio and was administrated under the technical direction of the Chemical Rocket Division with Mr. D. D. Scheer, Project Manager.

Pratt & Whitney Aircraft's Florida Research and Development Center at West Palm Beach, Florida, was the contractor, and Mr. W. E. Young was the Program Manager. The following Pratt & Whitney personnel contributed to the program:

Mr. R. E. Davis supervised the analytic effort,

Mr. C. G. Roberts assisted in the analytic work.

CONTENTS

CONTENTS

ILLUSTRATIONS

ILLUSTRATIONS (Continued)

ILLUSTRATIONS (Continued)

ILLUSTRATIONS (Continued)

TABLES

TABLES (Continued)

SUMMARY

An analytic and experimental investigation into the effects of blade tip clearance on inducer performance, and of leading edge sweepback on both blade pressure loading and performance was performed.

A tip vortex flow model was incorporated into a previously developed inducer internal flow analysis to represent tip clearance effects. Calculated vortex circulation from the basic analysis was found to be unrealistically large and the circulation was reduced empirically to improve the correlation between predicted and measured ideal head data. The empirical correction was consistent with the work of other investigators. Tip clearance losses were predicted with a semi-empirical relationship which was obtained from previous work. Measured inducer non cavitating performance data at these different tip clearances, which were available from a previous program, were correlated against predictions. The correlation of ideal head rise vs. tip clearance data was excellent. Measured loss data indicated the existence of an optimum tip clearance which cannot be predicted by the flow model, but, in general, correlation of the loss data was reasonably good. Complete cavitating performance data at the three tip clearances were not available and no predicted vs. measured correlation was performed.

The leading edge sweepback flow model had been previously incorporated in the inducer flow analysis. Two inducer test series were conducted during which inducer blade pressures and performance were measured at two leading edge sweepbacks. Blade pressure data correlated well with predictions when cavitation cavities were less than 30% of inducer axial length indicating that the flow model is adequate for use in blade stress calculations. When cavities were longer than 30% length predictions generally agreed with the measured data for the 8 deg (.14 rad) and were longer than measured for the 16 deg. (.28 rad) sweepbacks. Noncavitating ideal head predictions were in good agreement with measured data, but loss data correlation was poor, probably because of cavitation cavity associated losses. Measured cavitating performance data showed an increase in suction capability with increasing sweepback and the measured cavitating performance data correlated closely with the predicted data.

SECTION I
INTRODUCTION

Pump fed liquid propellant rocket engines depend on high speed lightweight turbopumps to supply the required pressure/flow conditions to the chamber. In order for these pumps to perform satisfactorily, propellants must be delivered to the inlets at conditions that are compatible with the capabilities of the pumping elements, that is, at pressure levels reasonably above the vapor pressure of the respective propellants so as to minimize pump cavitation and performance degradation. This can be accomplished by utilizing inducers capable of transient and steady state operation at varying degrees of cavitating conditions.

These inducer performance requirements lead to the design of high solidity (2-3) axial blade rows utilizing blades with thin leading edges to minimize local fluid accelerations and achieve maximum cavitation performance. The prediction of loads, stresses, and vibration resonant frequencies of such blades are necessary functions in the design of the blading. The goals of this NASA funded program were to develop and experimentally substantiate computer programs for the prediction of inducer blade loads, stresses and vibration characteristics.

Analyses of inducer blade hydrodynamic loading, stresses, and vibration characteristics were prepared, and a test program was conducted in which blade surface pressures and stresses were measured on an operating inducer. Data from these tests were then correlated with predictions and the correlated data indicated that the inducer internal flow analysis accurately predicted blade loads for the one inducer tested. The flow analysis also predicted inducer performance accurately. Predictions from the stress and vibration programs also agreed very closely with test data. The flow analysis accounted for blade leading edge sweepback, which affects both blade loading and performance, but no test data were available for correlation. Tip clearance effects, which were seen to have a significant effect on performance during the testing phase of the program were not accounted for in the analysis. These areas were selected for further study and the results of this effort are reported in this volume. The previous work is reported in Volume I (1)* and the computer programs are listed and described in Volume II (2). Volume II is being updated with the latest computer program changes and re-issued with this volume.

---

* Underlined numbers in parentheses refer to references which are listed in Section VII

The objectives of the work reported herin were to expand the original inducer internal flow analysis to include the capability of predicting the effects of tip clearance on performance, and of leading edge sweep on both performance and blade loading; and to demonstrate these capabilities by correlating predicted data with test data. The work consisted of the following two tasks, which are numbered consecutively from the original program tasks.

Task VII - Tip Clearance Model

The previous analytic treatment of the blade tip wall, or housing, as a rotating shroud was revised to treat the wall as a stationary member and to consider the effect of blade tip leakage on the boundary layer and on the main flow. Predicted data were correlated with inducer head rise and hydrodynamic efficiency measurements from the Task VI testing.

Task VIII - Blade Leading Edge Sweepback

The inducer from the original program was reoperated to an 8 deg (.14 rad) and a 16 deg (.28 rad) cone angle leading edge sweep and tested at each sweep angle to obtain measured performance and blade pressure data. Measured blade pressure and performance data were correlated with the analytic predictions.

Details of these efforts are discussed in this volume under the function section headings of "Test Apparatus and Procedure, Test Results, Analysis, etc". In areas where the previous effort was duplicated, such as the test apparatus, instrumentation, and procedure, only a brief description is given in the interest of completeness. Reference is made to Volume I for detail. Test data from Volume I, which were used in the data correlations, are repeated in this volume.

SECTION II
TEST APPARATUS AND PROCEDURE

A. Inducer

The inducer used in the follow-on work was designed in Task III and fabricated in Task V of the original program and these efforts are reported in (1). The inducer has a constant tip diameter, variable hub diameter, and J-blade type of blading (helical front portion, cambered rear portion). The inlet section is helical through a solidity of approximately 1.0. Basic design parameters are listed in Table 1 and the hub and blade tip contours are shown in figure 1. The inducer was machined from titanium and is pictured, with instrumentation grooves on the blades, in figure 2.

Table 1. Basic Inducer Design Parameters

	Inlet	Exit
Hub Diameter, in. (cm)	2.8 (7.1)	3.74 (9.5)
Blade Angle-Tip, deg (rad)	8 (0.14)	10 (0.18)
Blade Angle-Hub, deg (rad)	19.35(0.339)	18.25 (0.318)
Tip Diameter, in. (cm)	7.0 (17.8)	
Blade Thickness, in. (cm)	0.130 (0.330)	
Number of Blades	3	
Flow Coefficient	0.07	
Head Coefficient	0.24	
Suction Specific Speed (100% Head Falloff)	30,000 (min)	
Flow Rate, Gpm (m^3/S)	1060 (0.067)	
Rotor Speed, rpm (rad/s)	4900 (513)	

The inducer was reoperated to an 8 deg (.14 rad) leading edge sweep and then a 16 deg. (.28 rad) leading edge sweep for testing in this program. Leading edge sweep angle (α) is defined as shown in figure 3. The leading edge suction surface was machined parallel to the tangential direction for each sweep angle as shown in the tip section drawing of figure 3. Sweep angles were selected to provide test data over over what was considered to be the maximum range of interest in inducer design. Quantitative parametric data concerning optimum sweep angle for best performance are not available, but 16 degrees (.24 rad) is approximately the maximum that has been used in engine applications. Eight degrees (.14 rad) was selected as the other sweep angle to be tested. Photographs of the inducer with the two sweeps are shown in figures 4 and 5.

Blade tip wrap angles which correspond to the 8 and 16 degree cone angles are approximately 35 and 75 degrees (.61 and 1.31 rad) respectively.

The location of the tip leading edge for the two sweep-backs is indicated on the contour curve of figure 1. Both sweep angles were within the helical inlet section of the blading and, as a result, blade inlet metal angle was unchanged.

B. Test Facility

The sweptback inducers were tested in the same water loop that was used in the previous testing of the radial leading edge inducer. A schematic of the test facility (D-34) is shown in Figure 6. The 5 inch (12.70 cm) diameter leg was used during the contract testing, with the two 8 inch (20 cm) legs blocked off. Flow rate was regulated with a motorized throttling valve. Inlet pressure was controlled with a water accumulator located approximately 12 feet (3.65m) upstream of the test rig. Screens were installed just downstream of the accumulator for less than atmospheric inlet pressure test points. This provided the additional pressure drop necessary for the regulation of inlet pressure down to approximately 4 psi ($3N/cm^2$) absolute.

The test rig in which the sweptback configurations were tested also remained the same as that previously used with the radial inducer. The rig was designed in task III as reported in (1) and is shown in Figure 7. The design allowed for the installation of the pressure scanning valve in the inducer hub and the routing of all pressure tubing and electrical connections necessary for its operation. Figure 8 shows the test rig as it appeared installed in the test loop.

C. Instrumentation

Both performance and blade surface pressure data were taken for each inducer configuration tested. Instrumentation was essentially the same as that used in the initial testing and is described briefly in the following paragraphs.

1. Performance Instrumentation

Pressures were measured from wall taps and probes that were located as shown in Figure 9. All pressures were read from precision, ($\pm$ 0.2% F.S.), Heise pressure gages. Inlet total pressure was measured with Kiel probes on the pipe centerline upstream of the inducer. Inlet and exit flow distributions were measured with wedge type total-static probes installed in manual traverse fixtures. These wedge probes were nulled using a differential pressure gage connected across the two static taps. Probe traverse depth and flow angle were read off verniers on the fixture. The wedge probes were all calibrated prior to use and this data was utilized to correct measured static pressures.

Flow was measured with a turbine flow meter located in the 5 inch (12.70 cm) leg of the loop. Temperature was measured using a chromel-alumel thermocouple in the inlet line. Speed was measured by electronically counting the output of a magnetic transducer which sensed the passing frequency of a 60 tooth gear on the rig drive shaft. Table 2 lists a summary of the performance instrumentation and the maximum error which was estimated for each reading.

2. Blade & Hub Pressure Instrumentation

Inducer blade and hub static pressures were measured using a pressure scanning valve transducer assembly* located in the inducer hub as shown in figure 10. Blade pressure taps were drilled into .040 dia. (1.016 mm) tubes which were recessed into the blade surfaces. These tubes were routed to the front of the inducer and connected to the pressure scanning valve-transducer assembly. The scanning valve rotated in 48 steps, sequentially connecting each pressure tube to the single transducer which was located on the valve and inducer centerline. The scanning valve-transducer assembly is shown in Figure 11. The pressure scanning valve was modified to provide a purge supply to each tube as the valve rotated. Without the purge, water would back up into each tube until the centrifugal head developed by rotation of the inducer equaled the pressure on the surface of the blade. The transducer in the scanning valve would sense a pressure lower than surface pressure by the amount of centrifugal head. To eliminate this problem, the valve case was sealed so it could be pressurized and a purge hole was added to the rotor immediately ahead of the sensing groove. The case was pressurized from an air supply to a value higher than the highest anticipated blade surface pressure. As the rotor advanced each tube was purged and the water blown out. When the transducer was connected to a tube and the purge cut-off to that tube, the air in the tube remained at the pressure on the surface of the blade.

Blade pressure tap locations for the two swept leading edge test series are shown in Figure 12 and coordinates are listed in Table 3. Two of the blade angular pressure tap locations were eliminated from the pressure surface and three from the suction surface when the blades were swept back to 8^{o}. These taps were relocated to provide additional suction surface pressures. The removed and relocated positions are indicated on Figure 12. Two test series were conducted for each sweep back configuration, one with pressure taps near the tip and one with them at midspan (R1 and R2 of Figure 12). The shape of the leading edge prevented some of the blade pressure taps from being located on a

---

* Scanivalve Corporation, San Diego, California, Model 48D9 Special

design streamline and these are indicated on Table 3. Data which were obtained from these "off-streamline" positions were used for reference. The pressure tap instrumentation can be seen on the blades in figures 4 and 5.

Hub pressure tap locations were the same as for previous tests, the first at .25 in (.63 cm) axially inside the leading edge plane and four more spaced at .75 in (1.91 cm) increments.

Figure 13 shows an exploded view of the inducer, scanning valve, and related hardware in the order in which it was installed in the rig. Table 4 summarizes the instrumentation that was used to measure blade pressures and calculate operating conditions.

D. Test Procedure

1. Performance Tests

Non cavitating performance tests were conducted by setting a speed, flow, and inlet pressure and manually traversing the flow at the inducer inlet and exit. Total and static pressure and flow angle were measured at each of seven radial stations (spaced at equal area increments). Measurements from the probes and from other instrumentation (Table 2) were recorded on the test log sheet.

Cavitating tests were conducted by setting a speed and a flow, and reducing inlet pressure in four or five steps until inducer pressure rise dropped at least ten percent. A complete set of data was manually recorded at each inlet pressure setting. The inlet traverse probe was completely removed for these tests and the discharge traverse probe was set at the radial traverse station which was found to be most representative of mass averaged total head during the non cavitating tests.

2. Blade Pressure Tests

Blade pressure test data were also taken with the inlet traverse probe removed and the discharge probe set at the mass average representative station. Non cavitating and cavitating tests were conducted in the same manner as performance tests. The recording procedure included setting the test point conditions (speed, flow and inlet pressure), applying the purge air to the pressure scanning valve, starting the FM tape recorder, and then actuating the pressure scanning valve. The valve automatically made one complete revolution, at approximately one port per second. Valve purge pressure was set as high as possible to insure that no blade pressure data were lost because of water in the tap line. The valve operating limits were increased by 25% to 100 psia (69 N/Cm^2) maximum case pressure and 100 psia (69 N/Cm^2) maximum case to sensing port differential over the previous radial inducer tests and purge pressures.

E. Data Reduction

1. Performance

Performance data were calculated from manually recorded pressure, temperature, flow, rotative speed, and flow angle using the equations in Table 5. Gage height above the inducer axis and probe static pressure errors from all calibrations were taken into account before fluid heads were calculated. Inducer overall performance was calculated from an upstream station (PTUP in Figure 9) to the exit traverse station. The upstream stations was used in preference to the inlet traverse station to prevent inaccuracies in the inlet traverse data from affecting calculated performance.

Figure 14 gives the relative errors of the integrated to measured flows for the 8° and 16° (.14 and .28 rad) sweepback inducers. The agreement is generally within 5%, indicating that the overall accuracy of the performance data is good.

2. Blade Pressure

It was originally intended to reduce the blade pressure distribution data automatically from the FM data tapes, using the equations of table 5. Different tape recorders and recording setups had been used during the course of the program as various pieces of equipment were freed for this work and other in-use pieces were required elsewhere. This fact, coupled with missed sequences of the pressure scanning valve and various other tape irregularities, necessitated a rework of the automatic data reduction system between almost every run. Subsequent to the reduction of data from two tests in this manner, it was concluded that the automatic system was too costly in terms of the degree of increased accuracy as compared to manually reduced oscillograph data. Tape work was therefore discontinued and all data was reduced from the oscillograph traces. Data from the oscillographs were manually converted to pressures and head coefficients using calculators.

Table 2. Performance Test Instrumentation

Symbol	Parameter	Sensor	Readout	Range	Max Error
AN	Speed	Magnetic Transducer	Counter	-	1 rpm (0.1 rad/s)
Q	Flow	Turbine Flowmeter	Counter	1500 gpm (94,600 cu^3/s)	2%
T	Temperature	Thermocouple	Meter	-	2^oF (1.1^oK)
PSUP	Pressure-Static, Upstream	Wall Tap	Gage	100 psia (69 N/cm^2)	0.25% F.S.
PTUP	Pressure-Total, Upstream	Kiel Probe	Gage	100 psia (69 N/cm^2)	0.25% F.S.
PSIP	Pressure-Static, Inlet	Wall Tap	Gage	100 psia (69 N/cm^2)	0.25% F.S.
PTIP	Pressure-Total, Inlet	Kiel Probe	Gage	100 psia (69 N/cm^2)	0.25% F.S.
PSGW1	Pressure-Static, Wall	Wall Tap	Gage	100 psia (69 N/cm^2)	0.25% F.S.
PSGW2	Pressure-Static, Wall	Wall Tap	Gage	100 psig (69 N/cm^2)	0.25% F.S.
PSGW11	Pressure-Static, Wall	Wall Tap	Gage	100 psig (69 N/cm^2)	0.25% F.S.

Table 2. Performance Test Instrumentation (Continued)

Symbol	Parameter	Sensor	Readout	Range	Max Error
PSGW12	Pressure-Static, Wall	Wall Tap	Gage	100 psig (69 N/cm^2)	0.25% F.S.
PSGW13	Pressure-Static, Wall	Wall Tap	Gage	100 psig (69 N/cm^2)	0.25% F.S.
PSGW14	Pressure-Static, Wall	Wall Tap	Gage	100 psig (69 N/cm^2)	0.25% F.S.
PSGW15	Pressure-Static, Wall	Wall Tap	Gage	100 psig (69 N/cm^2)	0.25% F.S.
PSG1J	Pressure-Static, Inlet Trav.	Wedge Probe	Gage	100 psia (69 N/cm^2)	0.25% F.S.
PTG1J	Pressure-Total, Inlet Trav.	Wedge Probe	Gage	100 psia (69 N/cm^2)	0.25% F.S.
PSG2J	Pressure-Static, Exit Trav.	Wedge Probe	Gage	160 PSIA (110 N/cm^2)	0.25% F.S.
PTG2J	Pressure-Total, Exit Trav.	Wedge Probe	Gage	160 psia (110 N/cm^2)	0.25% F.S.
QAB1J	Pressure-Dynamic, Inlet Trav.	Wedge Probe	Transducer, VTVM	15 psid (10 N/cm^2)	0.20% F.S.
QAB2J	Pressure-Dynamic, Exit Trav.	Wedge Probe	Transducer, VTVM	50 psid (34 N/cm^2)	0.20% F.S.
BAB1J	Flow Angle-Inlet Trav.	Wedge Probe	Vernier	360° (6.3 rad)	0.5° (0.09 rad)
BAB2J	Flow Angle-Exit Trav.	Wedge Probe	Vernier	360° (6.3 rad)	0.5° (0.09 rad)

Table 3. Blade Surface Pressure Tap Locations

Angular Location			8 deg. (.14 rad) Leading Edge Sweepback Inducer				16 deg. (.28 rad) Leading Edge Sweepback Inducer			
			Radial Location-R Suction Side		Radial Location-R Pressure Side		Radial Location-R Suction Side		Radial Location-R Pressure Side	
Position	Deg.	Rad.	1	2	1	2.	1	2	1	2
			in. cm.	in. cm.	in. cm.	in. cm.	in. cm.	in. cm.	in. cm.	in. cm.
1	21.3	.3718	2.398*6.091	2.398 6.091	2.398*6.091	2.398 6.091	1.670*4.242	1.670*4.242	- -	- -
2	29.5	.5149	2.398*6.091	2.398 6.091	2.398*6.091	2.398 6.091	1.890*4.801	1.890*4.801	2.240*5.690	2.240*5.690
3	37.7	.6580	2.398*6.091	2.398 6.091	3.305 8.395	2.398 6.091	2.130*5.410	2.130*5.410	2.320*5.893	2.320*5.893
4	45.9	.8011	3.305 8.395	2.398 6.091	3.305 8.395	2.398 6.091	2.370*6.020	2.370*6.020	2.720*6.909	2.398 6.091
5	54.1	.9442	3.305 8.395	2.398 6.091	3.305 8.395	2.398 6.091	2.670*6.782	2.398 6.091	2.930*7.442	2.398 6.091
6	66.35	1.1580	3.305 8.395	2.398 6.091	3.305 8.395	2.398 6.091	3.065*7.785	2.398 6.091	3.305 8.395	2.398 6.091
7	78.6	1.3718	3.305 8.395	2.398 6.091	3.305 8.395	2.398 6.091	3.305 8.395	2.398 6.091	3.305 8.395	2.398 6.091
8	90.85	1.5856	3.305 8.395	2.398 6.091	3.305 8.395	2.398 6.091	3.305 8.395	2.398 6.091	3.305 8.395	2.398 6.091
9	103.1	1.7994	3.305 8.395	2.398 6.091	3.305 8.395	2.398 6.091	3.305 8.395	2.398 6.091	3.305 8.395	2.398 6.091
10	114.8	2.0036	3.305 8.395	2.398 6.091	- -	- -	3.305 8.395	2.398 6.091	- -	- -
11	126.5	2.2078	3.305 8.395	2.398 6.091	- -	- -	3.305 8.395	2.398 6.091	- -	- -
12	138.2	2.4120	3.305 8.395	2.398 6.091	- -	- -	3.305 8.395	2.398 6.091	- -	- -
13	150.0	2.6180	3.309 8.405	2.428 6.167	3.309 8.405	2.428 6.167	3.309 8.405	2.428 6.167	3.309 8.405	2.428 6.167
14	185.0	3.2289	3.312 8.413	2.443 6.206	3.312 8.413	2.443 6.206	3.312 8.413	2.443 6.206	3.312 8.413	2.443 6.206
15	220.0	3.8397	3.316 8.423	2.471 6.276	3.316 8.423	2.471 6.276	3.316 8.423	2.471 6.276	3.316 8.423	2.471 6.276
16	255.0	4.4506	3.320 8.433	2.500 6.350	3.320 8.433	2.500 6.350	3.320 8.433	2.500 6.350	3.320 8.433	2.500 6.350
17	344.0	6.0039	3.324 8.443	2.570 6.528	3.324 8.443	2.570 6.528	3.324 8.443	2.570 6.528	3.324 8.443	2.570 6.528
18	352.0	6.1436	3.328 8.453	2.578 6.548	3.328 8.453	2.578 6.548	3.328 8.453	2.578 6.548	3.328 8.453	2.578 6.548
19	360.4	6.2902	3.332 8.463	2.587 6.571	3.332 8.463	2.587 6.571	3.332 8.463	2.587 6.571	3.332 8.463	2.587 6.571
20	368.6	6.4333	3.336 8.473	2.595 6.591	3.336 8.473	2.595 6.591	3.336 8.473	2.595 6.591	3.336 8.473	2.595 6.591

* Tap not located on Design Streamline

Table 4. Blade Pressure Test Instrumentation

Symbol	Parameter	Sensor	Readout	Range	Max Error
PTUP	Pressure-Total, Upstream	Kiel Probe, S.G. Transducer	Gage and Tape(1)	100 psia (69 N/cm^2)	3% F.S.
PTG2J	Pressure-Total, Exit	Wedge Probe, S.G. Transducer	Gage and Tape(1)	150 psia (103 N/cm^2)	3% F.S.
PO-P47	Pressure-Static, Blade	Press. Scan. Valve, S.G. Transducer	Tape	150 psia (103 N/cm^2)	3% F.S.
PSBP	Position-Press. Scan Valve	Potentiometer	Tape	48	-
BDRP	Data Recording Pulse		Tape	—	-

(1) Range and error are for tape recorded data.

Table 5. Performance Data Reduction Equations

A. Blade Element Performance

Fluid Velocity: $V = \sqrt{2g(H_{i,j} - h_{i,j})}$

Fluid Axial Velocity: $V_z = V \sin \alpha$

Fluid Tangential Velocity: $V_u = V \cos \alpha$

Ideal Head Rise: $HI = \frac{U_e V_{ue}}{g}$ (Assumes $V_{uo} = 0$)

Actual Head Rise: $H = \frac{1}{\rho} P_T - H_\infty$

Head Rise Coefficient: $\psi = \frac{g}{\rho} \frac{\Delta P_T}{U_T^2}$

Head Loss Coefficient: $\psi_\ell = \frac{g(HI - H)}{U_T^2}$

Flow Coefficient: $\phi = \frac{V_z}{U_T}$

Efficiency: $\eta = \frac{H}{HI}$

Net Positive Suction Head: $NPSH = H_\infty - h_v$

B. Overall Performance

Average Total Head at an Axial Station: $\overline{H} = \left(\overline{\frac{P_T}{\rho}}\right)_j = \frac{\sum_{R_H}^{R_T} V_z \, R \frac{P_T}{\rho} \, \Delta R}{\sum_{R_H}^{R_T} V_z \, R \, \Delta R}$

Average Ideal Head at an Axial Station: $\overline{HI}_j = \frac{\sum_{R_H}^{R_T} V_z \, R \frac{U V_u}{g} \, \Delta R}{\sum_{R_H}^{R_T} V_z \, R \, \Delta R}$

Average Inlet Velocity: $\overline{V}_{zo} = \frac{Q}{\pi(R_T^2 - R_H^2)}$

Average Flow Coefficient: $\overline{\phi} = \frac{\overline{V}_{zo}}{U_T}$

Average Head Coefficient: $\overline{\psi} = \frac{g\overline{H}}{U_T^2}$

Average Efficiency: $\overline{\eta} = \frac{\overline{H}}{HI}$

Average Inlet Static Head: $\overline{h} = \overline{H}_o - \frac{\overline{V}_z^2}{2g}$

Cavitation Number: $\overline{K} = \frac{2g(h_o - h_v)}{\overline{V}_{zo}^2 + U_T^2}$

Static Head Coefficient: $\psi_s = \frac{g(h - H)}{U_T^2}$

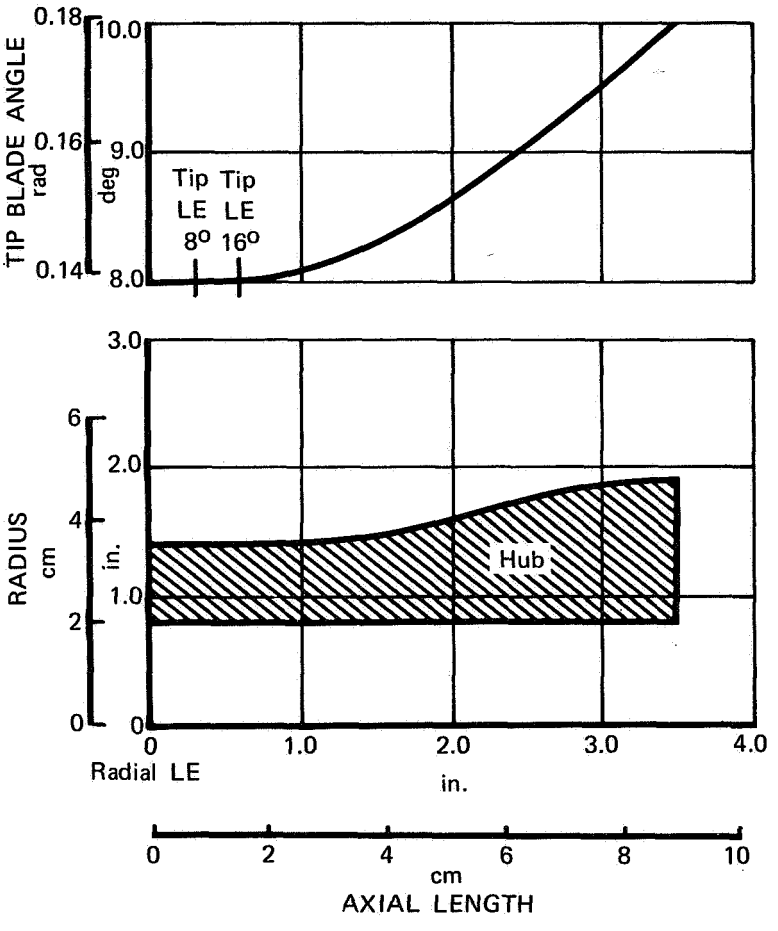

Figure 1. Inducer Flow Path and Blade Angle Distribution FD 25798B

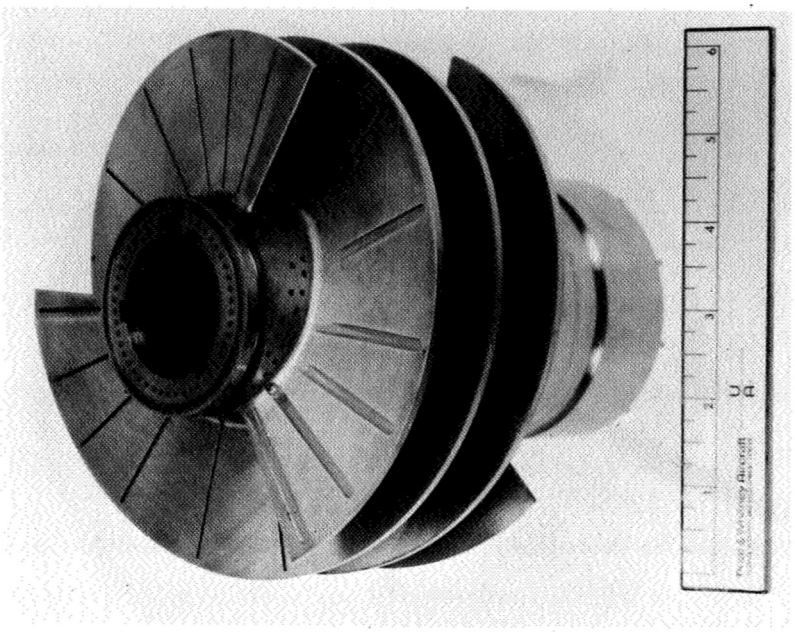

Figure 2. View of Radial Leading Edge Inducer After Machining and Before Installation of Pressure Tubing FE 88107

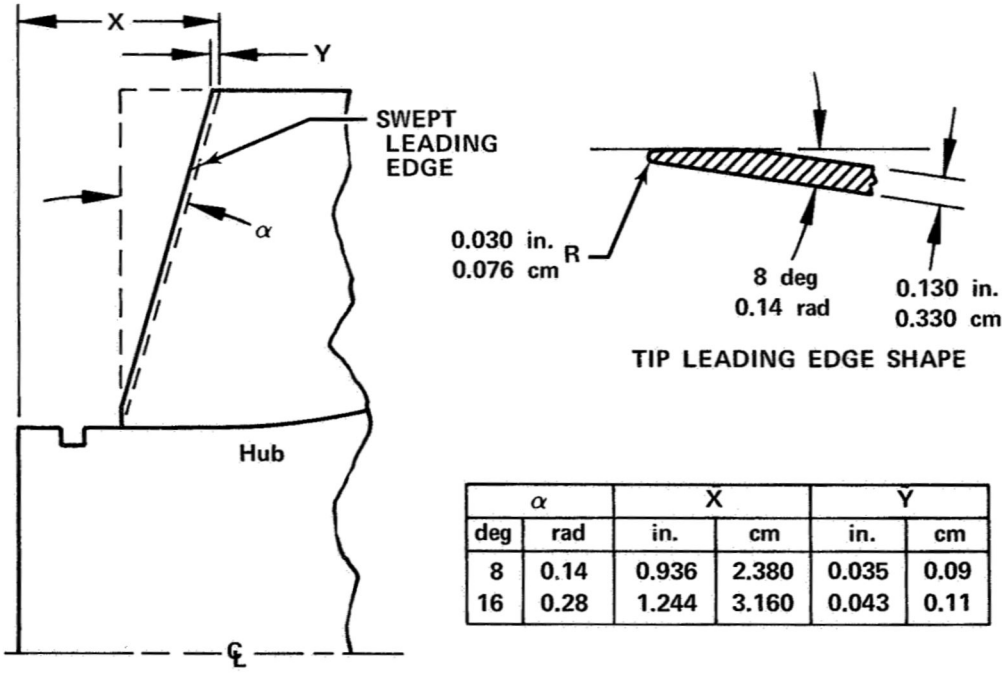

α		X		Y	
deg	rad	in.	cm	in.	cm
8	0.14	0.936	2.380	0.035	0.09
16	0.28	1.244	3.160	0.043	0.11

Figure 3. Definition of Leading Edge Sweep Angle FD 61210

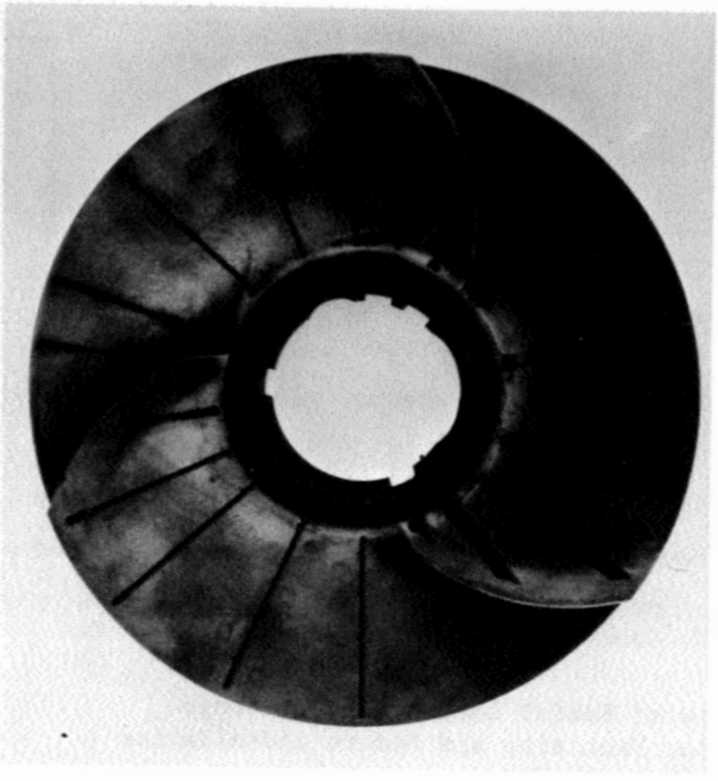

Figure 4. 8 Degree (0.14 radian) Leading Edge Sweepback Inducer FE 107221

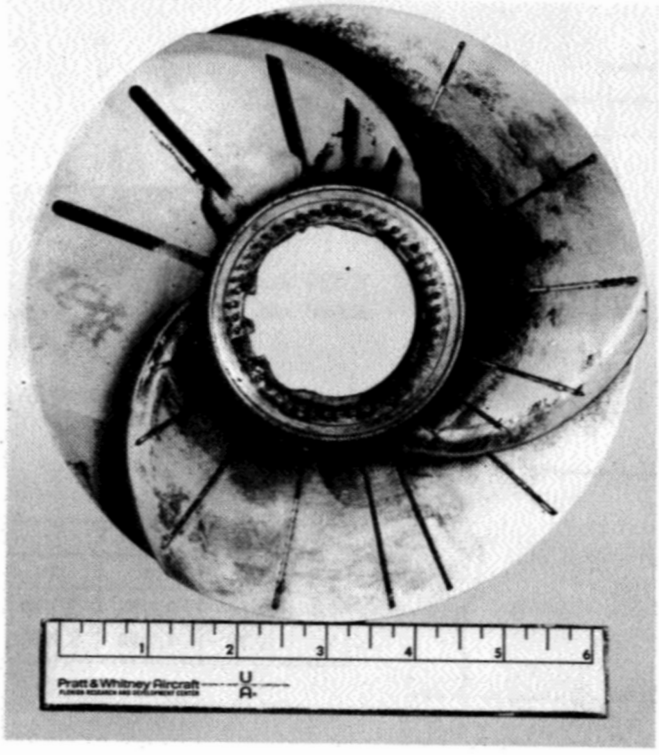

Figure 5. 16 Degree (0.28 radian) Leading Edge Sweepback Inducer FE 113407

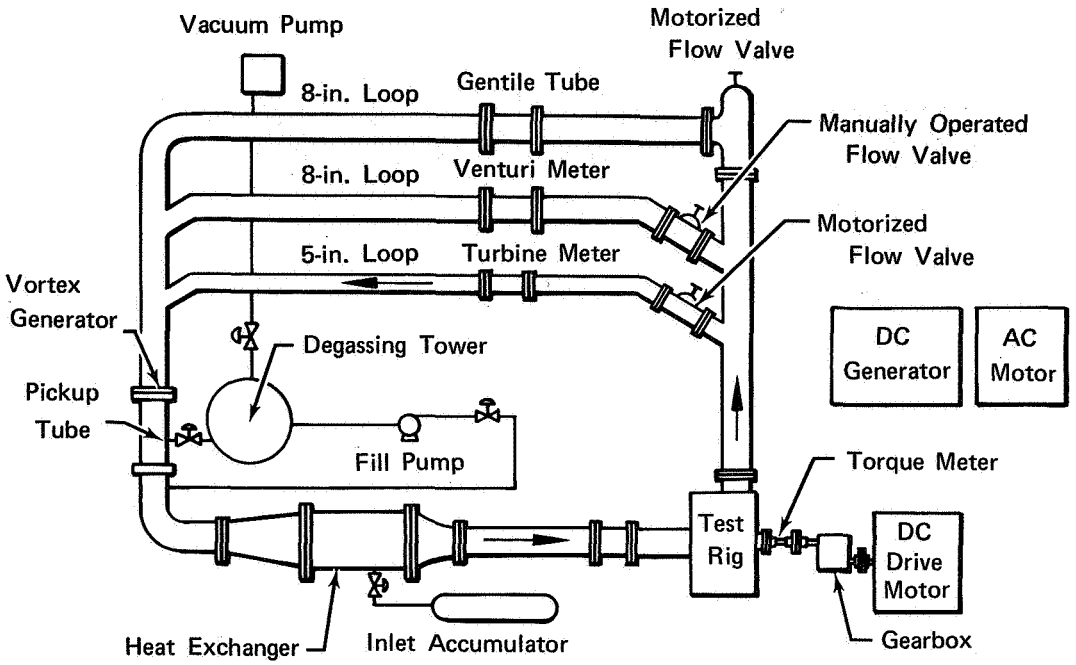

Figure 6. Schematic of Water Flow Loop FD 19703E

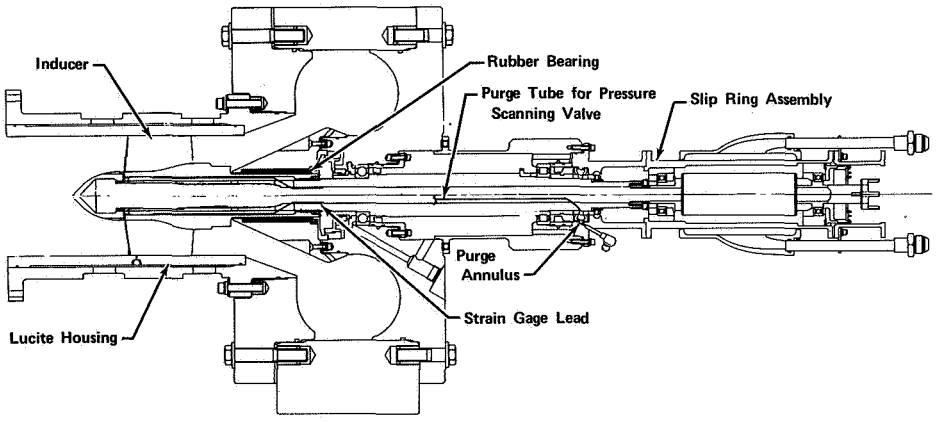

Figure 7. Inducer Test Rig FD 21423C

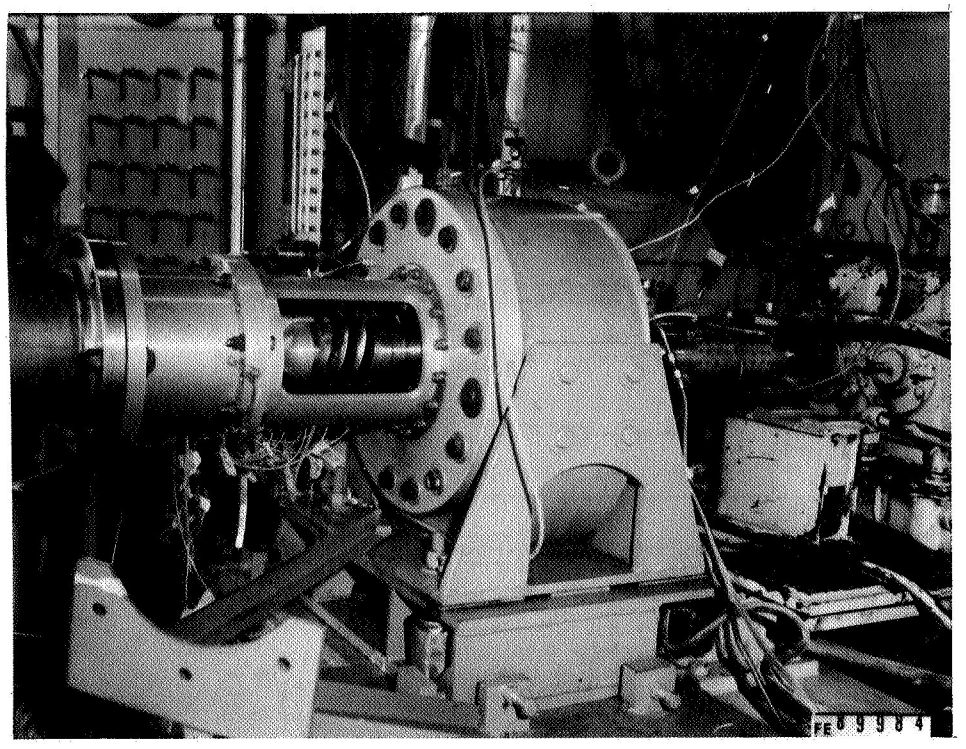

Figure 8. Overall View of Test Rig FE 89984

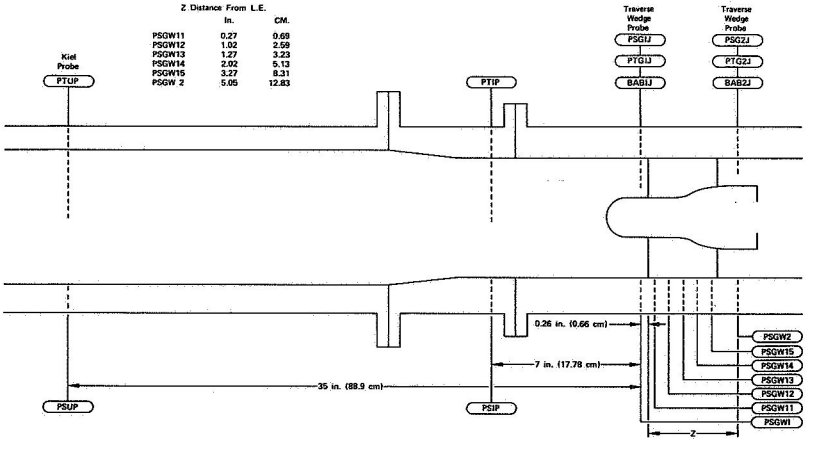

Figure 9. Performance Pressure Instrumentation Locations FD 48166

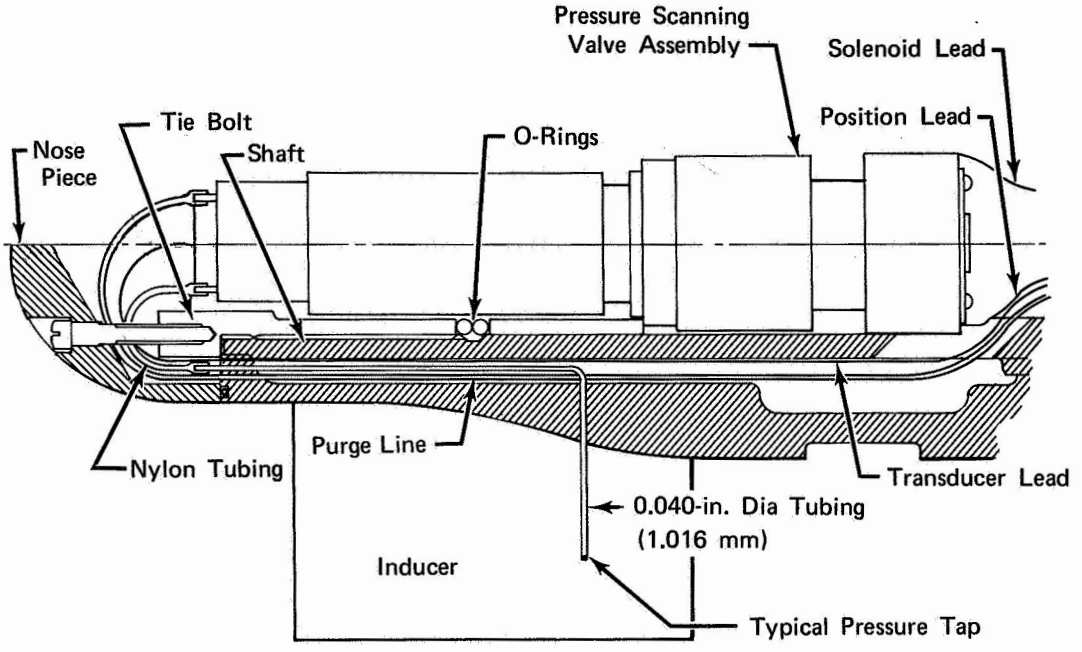

Figure 10. Pressure Scanning Valve in Inducer Hub

FD 25812A

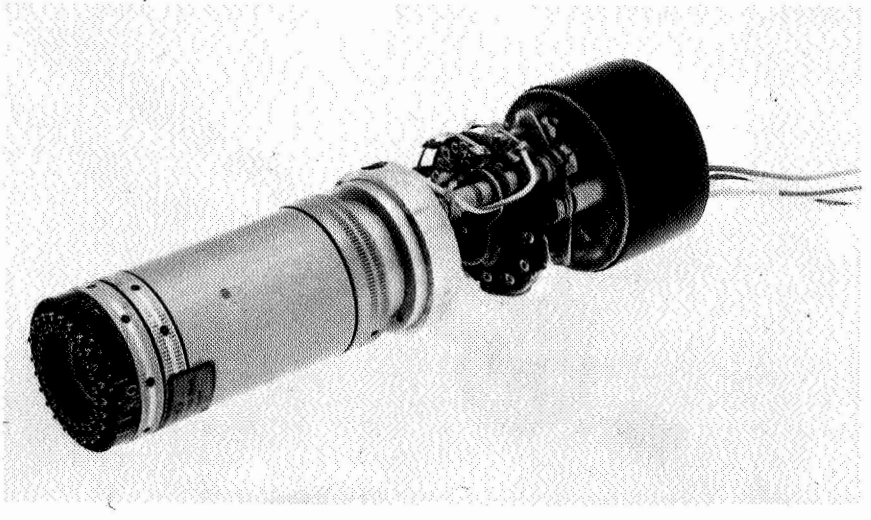

Figure 11. Pressure Scanning Valve - Transducer Assembly

FE 94089

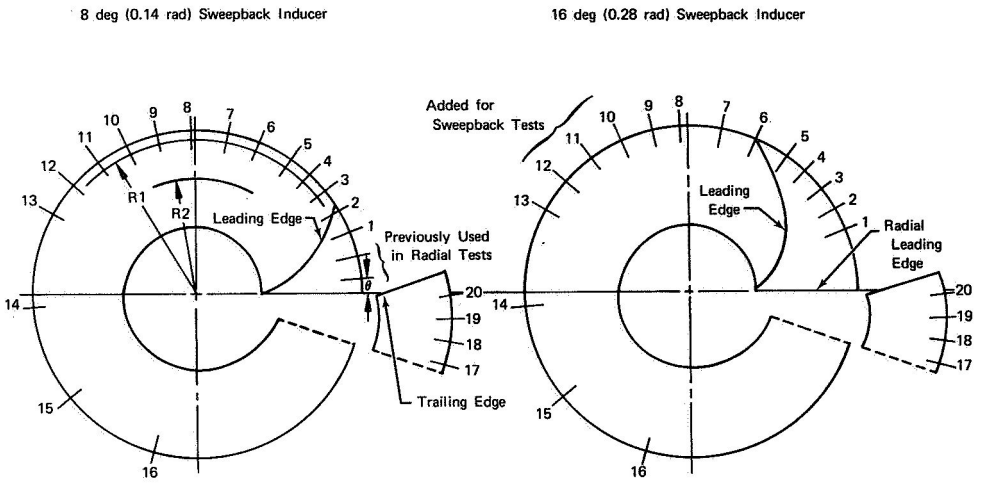

Figure 12. Inducer Blade Pressure Tap Locations FD 61211

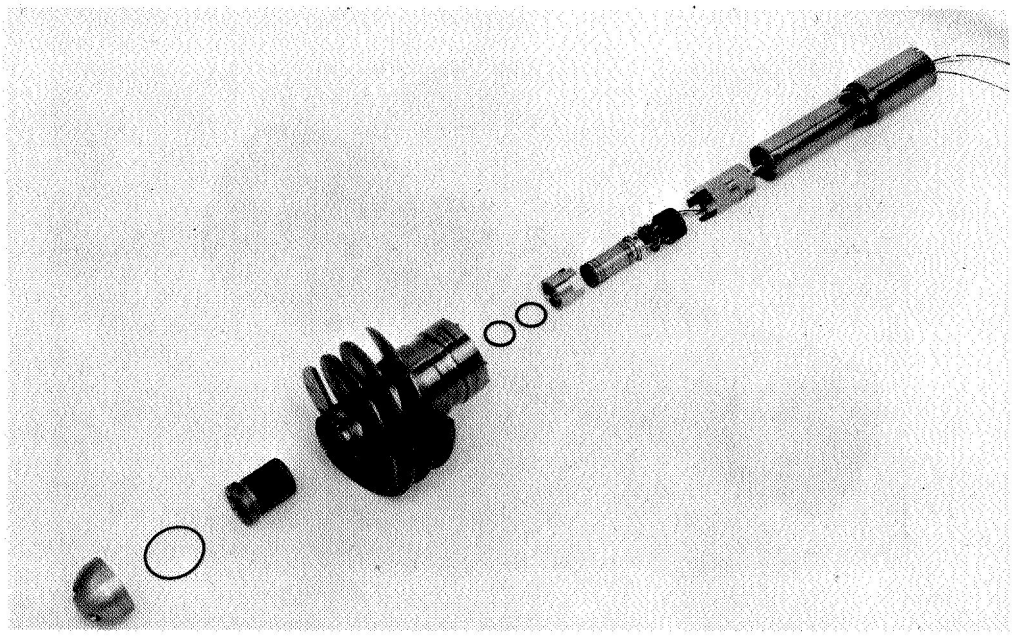

Figure 13. Exploded View of Inducer and Pressure Scanning Valve FE 94088

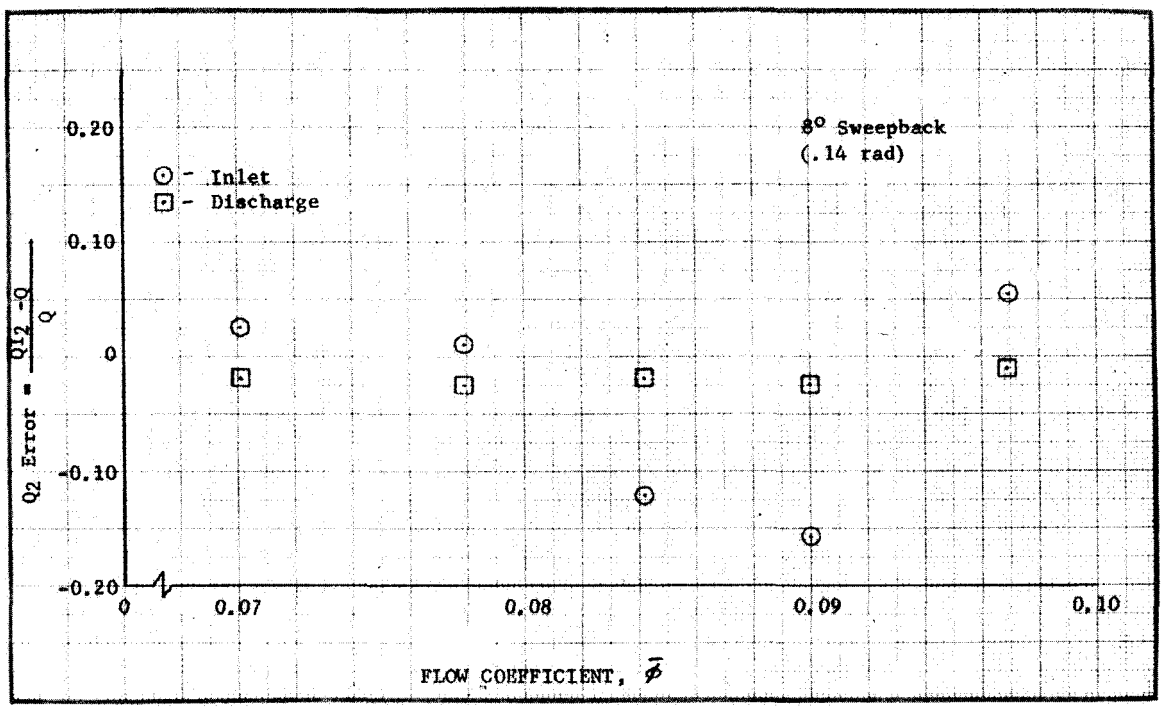

DF 91235

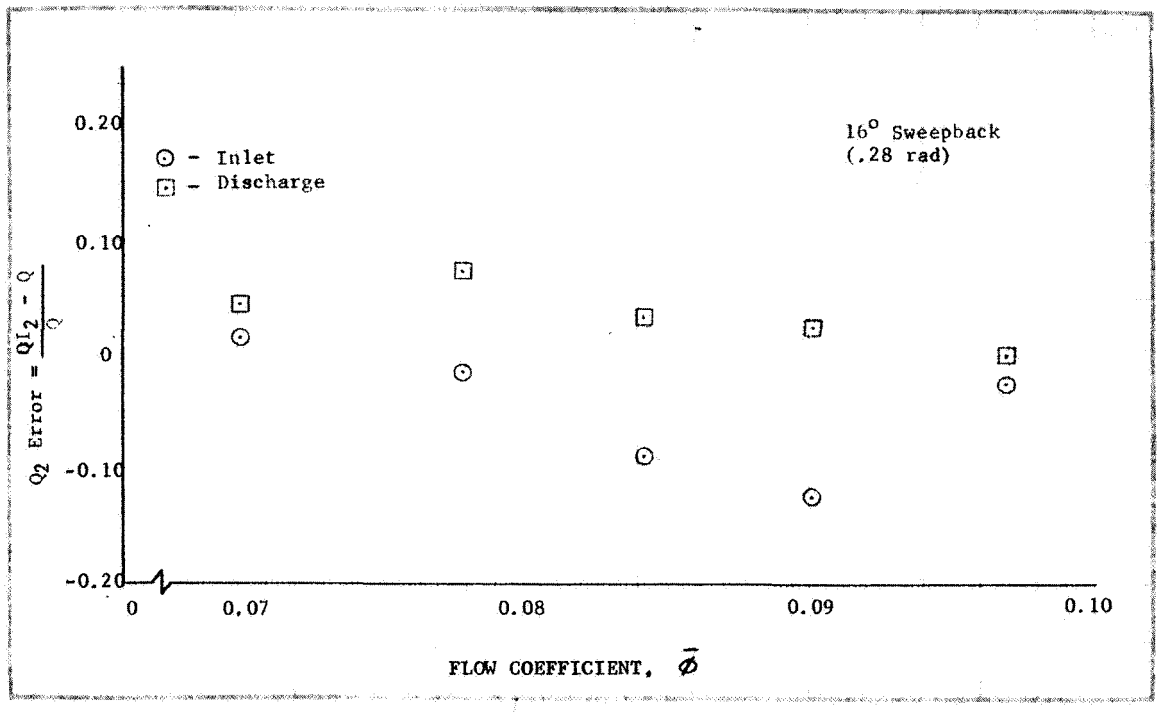

DF 91236

Figure 14. Comparison of Integrated with Flowmeter Measured Flow at Inducer Inlet and Discharge

SECTION III
TEST RESULTS

A. Tip Clearance Tests

Task VII required modification of the Inducer Hydrodynamic Program to account for the effects of blade tip clearance on inducer performance. Test data from Task VI of the original program (1) was to be correlated with predictions from the modified program. A review of the tip clearance data is given in this section.

As explained in (1), the original blade tip clearance selected for the radial leading edge inducer was .061 in. (0.155 cm). The reverse flow measured at the inducer tip with this clearance could not be handled by the two-dimensional meridional streamline analysis used in the hydrodynamic computer program. A study resulted in reducing reverse flow by reducing tip clearance from .061 in. (0.155 cm) to .021 in. (0.054 cm). This provided a reduction in prerotation and led to the design and use of a new housing with a clearance of .011 in. (.028 cm). Thus data were gathered in three different blade tip clearances during the radial inducer test program. Another test program, reported in (3), resulted in additioal data at the .011 in. tip clearance.

Figure 15 compares the radial distributions of the inlet flow angle of the radial inducer at the three tip clearances. Angles are measured from the axial direction so that the amount of prerotation present is a direct function of the magnitude of the flow angle. Pure axial flow has an angle of zero degrees, while angles greater than 90 degrees (1.57 rad) indicate backflow. It can be seen that reducing the tip clearance appreciably helps the prerotation problem. Not only does the flow more closely approach axial flow for a large percentage of the inducer inlet radius, but the prerotation that does remain at the tip is reduced to less than 90 deg (1.57 rad). The reverse flow was essentially eliminated at flow coefficients greater than the .070 for the reduced clearances of .021 in. (.054 cm) and .011 in. (.028 cm). Prerotation was entirely eliminated at a flow coefficient of .096.

The effects of tip clearance on noncavitating performance can be seen in Figures 16 and 17 where efficiency and head coefficient are plotted as functions of flow coefficient and clearance/blade height ratio respectively. As noted in (1), the maximum efficiency and head rise occur, not for the minimum tip clearance, but for the .021 in. clearance indicating the existence of an "optimum" clearance. It was stated in (1) that the drops in efficiency and head coeffient at a clearance of .011 in. might have been caused by the instrumentation on the blades which cast some doubt on the "optimum" clearance conclusion. Additional tests were conducted in the program of (3)using an inducer with no blade instrumentation and the results correlated closely with the previous data, which confirms that an optimum clearance does exist.

Complete cavitating performance data were not available for the three tip clearances at a common flow coefficient and a conclusion regarding the effect of clearance on cavitating performance could not be made.

B. Leading Edge Sweepback Tests

The results of the performance and blade pressure loading tests conducted during Task VIII for the two sweep leading edge inducer configurations are given in the following paragraphs.

1. Performance Tests

A summary of performance test points which were run for the 8 and 16 deg (.14 and .28 rad) leading edge sweep inducers is given in Table 6. All performance data were taken at a tip speed of 150 ft/sec (45.6 m/s) and at a tip clearance of .011 in. (0.028 cm). Noncavitating and cavitating test results are discussed separately in the following paragraphs.

a. Non-Cavitating

Non-cavitating operation is defined here as operation at an inlet pressure where a degree of cavitation can exist but is not detrimental to performance. All non-cavitating tests were run at an NPSH of approximately 106 ft (32.3 m) which is approximately six times the value at which head fall off occurred.

Mass averaged non-cavitating performance for the two swept inducer tests, along with the radial test data from (1), is shown in figure 18. The data show that the addition of an 8 deg (.14 rad) sweep to the leading edge raised efficiency by approximately 6 points. When the sweep angle was increased to 16 deg (.28 rad) efficiency decreased to within 3 points above the radial inducer values. Sweep angle seemed to have negligible effect on head coefficient, the small difference in figure 18 could be attributed to data scatter.

Head coefficient and efficiency are shown plotted vs sweep angle in figure 19. This figure shows clearly the existence of an optimum sweep angle (from the non cavitating performance stand point) which is between 0 and 16 deg (0 to .28 rad) for this inducer.

The radial distributions of the inlet flow parameters (flow angle, axial velocity and total head) for both the 8° and 16° (.14 and .28 rad) sweepback inducers are given in figure 20. Data for both sweepbacks are similar and show that prerotation, as evidenced by inlet flow angle, is present in a larger part of the inlet flow field than it was for the radial inducer. Back flow was noted at the tip of both sweepback configurations at flow coefficients of approximately .090 and less. The radial inducer did not have back flow at the .011 in (.028 cm) tip clearance which was used for the swept inducers. It should be noted that as the inducer blade is swept, the fixed probe measurement station becomes farther from the blade. Inlet flow may have a larger amount of prerotation nearer to the blade leading edge.

The radial distributions of the discharge flow parameters (including head coefficient, efficiency, deviation angle and ideal head coefficient) are shown in figure 21. The relative change in these parameters from one configuration to another is very small. This is as expected

since the inlet of the inducer was the only thing being changed and the effect on average performance was slight. The only significant difference in the parameters at the exit between any of the inducer designs shows up in the discharge ideal head coefficient distributions. The ideal head coefficients at the outer streamlines of the 16° (.28 rad) sweptback inducer are somewhat higher than those of the 8° (.14 rad) sweptback inducer.

b. Cavitating

Cavitating performance tests of the two sweptback designs were conducted in conjunction with the blade pressure tests. This provided four or five data points during each test run. All runs were performed twice, the first time with the pressure taps at one radius, and again with the pressure taps at the other radius. An attempt was made to set the same inlet pressure for both radii, and this was accomplished within the limitations of the test loop. A total of eight to ten cavitating test points were accumulated for each sweepback at each flow coefficient.

A comparison of the suction capabilities of the radial and the two sweptback inducers is given in figure 22. The comparison is shown for a flow coefficient of 0.084, but is typical of the other flow coefficients. The addition of sweepback to the blade leading edge resulted in a sizeable increase in suction performance. This is further illustrated in the crossplot of minimum cavitation number achieved versus sweepback angle of figure 22. Increases in sweepback lead to corresponding increases in suction performance, up to the limit of sweepback angle tested under this contract.

2. Blade Pressure Loading Tests

A summary of the operating points at which the inducer blade surface pressures were recorded is given in Table 7. Difficulties with the "Scanivalve" purge air supply limited the amount of blade surface pressure data that could be acquired. As discussed in Section IIC, the purge air pressure at the "Scanivalve" must be higher than the blade surface pressures to ensure that all of the water is blown out of each pressure tap tube before a reading is taken. The purge air is supplied to the shaft, and subsequently to the valve, through a cavity formed by two lip seals. Due to rapid wear of the seals and the resultant high leakage, purge pressure dropped below some of the blade surface pressures, particularly in the high NPSH tests and in the aft portion of the inducer during the low NPSH tests. As a result all of the water was not purged from these pressure tap tubes and, therefore, the scanivalve readings were not indicative of the surface pressure. Attempts to reduce seal wear, such as introducing cooling water and the use of teflon in place of rubber, were unsuccessful.

The majority of the measured blade pressure data are useful for correlation with predictions because of the apparent accuracy of the leading edge suction surface measurements which were low pressures and did not require a high purge pressure. These data are extremely sensitive to leading edge sweep and, as such, provide most of the required empirical information regarding the effects of sweep on inducer blade loading and performance.

Table 8 summarizes the operating points at which useable pressure data were taken during the water loop testing and for which predicted and experimental data comparisons were made. These operating points have been assigned numbers. The blade and hub pressure data are tabulated in Tables 9 through 18. Figures 23, 24 and 25 indicate the relationship of these points to the cavitating and noncavitating performance of the two sweptback inducers.

Table 6. Summary of Performance Tests

Test No.	Speed rpm	Speed rad/sec	Flow gpm	Flow cm^3/s	Inlet Total Pressure psig	Inlet Total Pressure N/cm^2	Temperature ^oF	Temperature ^oK
8^o Sweepback								
6.01	4900	513.1	1464	92,380	31.5	21.7	81	300.2
6.02	4900	513.1	1362	85,940	31.5	21.7	84	301.9
6.03	4900	513.1	1272	80,270	31.5	21.7	86.5	303.3
6.04	4900	513.1	1177	74,270	31.5	21.7	90	305.2
6.05	4900	513.1	1060	66,890	31.5	21.7	90	305.2
6.08	4900	513.1	1362	85,940	31.5	21.7	81	300.2
	4900	513.1	1362	85,940	12.2	8.4	81	300.2
	4900	513.1	1362	85,940	2.7	1.9	81	300.2
	4900	513.1	1362	85,940	-5.3	-3.7	81	300.2
6.09	4900	513.1	1273	80,330	11.6	8.0	85	302.4
	4900	513.1	1273	80,330	1.9	1.3	86	303.0
	4900	513.1	1273	80,330	-6.3	-4.3	86	303.0
6.12	4900	513.1	1416	89,350	31.5	21.7	87	303.6
	4900	513.1	1416	89,350	12.1	8.3	90	305.2
	4900	513.1	1416	89,350	1.5	1.0	92	306.3
	4900	513.1	1416	89,350	-7.0	-4.8	93	306.9
6.13	4900	513.1	1362	85,940	31.5	21.7	81	300.2
	4900	513.1	1362	85,940	12.1	8.3	84	301.9
	4900	513.1	1362	85,940	2.3	1.3	86	303.0
	4900	513.1	1362	85,940	-6.8	-4.5	87	303.6
6.14	4900	513.1	1272	80,270	31.5	21.7	93	306.9
	4900	513.1	1272	80,270	12.1	8.3	94	307.4
	4900	513.1	1272	80,270	2.1	1.4	94	307.4
	4900	513.1	1272	80,270	-6.5	-4.5	95	308.0

Table 6. Summary of Performance Tests (Continued)

Test No.	Speed rpm	Speed rad/sec	Flow gpm	Flow cm^3/s	Inlet Total Pressure psig	Inlet Total Pressure N/cm^2	Temperature ^oF	Temperature ^oK
16° (.28 rad) Sweepback								
7.03	4900	513.1	1362	85,940	31.5	21.7	93	306.9
	4900	513.1	1362	85,940	11.9	8.2	93	306.9
	4900	513.1	1362	85,940	2.1	1.4	93	306.9
	4900	513.1	1362	85,940	-4.8	-3.3	93	306.9
	4900	513.1	1362	85,940	-7.3	-5.0	93	306.9
7.04	4900	513.1	1272	80,270	31.5	21.7	92	305.3
	4900	513.1	1272	80,270	11.0	7.6	92	306.3
	4900	513.1	1272	80,270	1.4	1.0	92	306.3
	4900	513.1	1272	80,270	-7.7	-5.3	93	306.9
	4900	513.1	1272	80,270	-8.2	-5.6	93	306.9
7.05	4900	513.1	1272	80,270	31.5	21.7	93	306.9
	4900	513.1	1272	80,270	3.6	2.5	94	307.4
	4900	513.1	1272	80,270	-4.9	-3.4	94	307.4
	4900	513.1	1272	80,270	-8.2	-5.6	94	307.4
	4900	513.1	1233	77,800	-10.3	-7.1	95	308.0
7.06	4900	513.1	1465	92,450	31.5	21.7	88	304.1
7.07	4900	513.1	1362	85,490	31.5	21.7	93	306.9
7.08	4900	513.1	1272	80,270	31.5	21.7	95	308.0
7.09	4900	513.1	1177	74,270	31.5	21.7	97	309.1
7.10	4900	513.1	1060	66,890	31.5	21.7	99	310.2
7.13	4900	513.1	1362	85,940	31.3	21.6	86	303.0
	4900	513.1	1362	85,940	11.5	7.9	87	303.6
	4900	513.1	1362	85,940	0.8	0.6	87.5	303.8
	4900	513.1	1362	85,940	-3.1	-2.1	88	304.1
	4900	513.1	1317	83,100	-8.5	-5.9	88	304.1
7.14	4900	513.1	1272	80,270	31.3	21.6	87	303.6
	4900	513.1	1272	80,270	4.5	3.1	88	304.1
	4900	513.1	1272	80,270	1.3	0.9	88	304.1
	4900	513.1	1272	80,270	-3.9	-2.7	87	303.6
	4900	513.1	1211	76,420	-8.7	-6.0	87	303.6

Table 7. Summary of Blade Pressure Tests

Test No.	Speed rpm	Speed rad/s	Flow gpm	Flow cm^3/s	Inlet Total Pressure psig	Inlet Total Pressure N/cm^2	Temperature ^oF	Temperature ^oK
8^o (.14 rad) Sweepback, Pressure Taps at Inner Radius								
6.06-1	4900	513.1	1460	92,130	31.5	21.7	80	299.7
6.06-2	4900	513.1	1361	85,880	31.5	21.7	81	300.2
6.06-3	4900	513.1	1272	80,270	31.5	21.7	82	300.8
6.06-4	4900	513.1	1060	66,890	31.5	21.7	84	301.9
6.07-1	3920	410.5	1163	73,390	31.5	21.7	82	300.8
6.07-2	3920	410.5	1090	68,789	31.5	21.7	81	300.2
6.07-3	3920	410.5	1015	64,050	31.5	21.7	81	300.2
6.07-4	3920	410.5	849	53,570	31.5	21.7	81	300.2
6.08-1	4900	513.1	1362	85,940	12.2	8.4	81	300.2
6.08-2	4900	513.1	1362	85,940	2.7	1.9	81	300.2
6.08-3	4900	513.1	1362	85,940	-5.3	-3.7	81	300.2
6.09-1	4900	513.1	1273	80,330	11.6	8.0	85	302.4
6.09-2	4900	513.1	1273	80,330	1.9	1.3	86	303.0
6.09-3	4900	513.1	1273	80,330	-6.3	-4.3	86	303.0
8^o (.14 rad) Sweepback, Pressure Taps at Outer Radius								
6.10-1	3920	410.5	1160	73,200	31.5	21.7	90	305.2
6.10-2	3920	410.5	1090	68,780	31.5	21.7	90	305.2
6.10-3	3920	410.5	1015	64,050	31.5	21.7	90	305.2
6.10-4	3920	410.5	849	53,570	31.5	21.7	90	305.2
6.11-1	4900	513.1	1446	91,250	31.5	21.7	87	303.6
6.11-2	4900	513.1	1351	85,880	31.5	21.7	88	304.1
6.11-3	4900	513.1	1271	80,200	31.5	21.7	90	305.2
6.11-4	4900	413.1	1050	66,890	31.5	21.7	92	306.3

Table 7. Summary of Blade Pressure Tests (Continued)

Test No.	Speed rpm	Speed rad/s	Flow gpm	Flow cm^3/s	Inlet Total Pressure psig	Inlet Total Pressure N/cm^2	Temperature ^oF	Temperature ^oK
8^o (.14 rad) Sweepback, Pressure Taps at Outer Radius								
6.12-1	4900	513.1	1416	89,350	31.5	21.7	87	303.6
6.12-2	4900	513.1	1416	89,350	12.1	8.3	90	305.2
6.12-3	4900	513.1	1416	89,350	1.5	1.0	92	306.3
6.12-4	4900	513.1	1416	89,350	-7.0	-4.8	93	306.9
6.13-1	4900	513.1	1362	85,940	31.5	21.7	81	300.2
6.13-2	4900	513.1	1362	85,940	12.1	8.3	84	301.9
6.13-3	4900	513.1	1362	85,940	1.9	1.3	86	303.0
6.13-4	4900	513.1	1362	85,940	-6.6	-4.5	87	303.6
6.14-1	4900	513.1	1272	80,270	31.5	21.7	93	306.9
6.14-2	4900	513.1	1272	80,270	12.1	8.3	94	307.4
6.14-3	4900	513.1	1272	80,270	2.1	1.4	94	307.4
6.14-4	4900	513.1	1272	80,270	-6.5	-4.5	95	308.0
16^o (.28 rad) Sweepback, Pressure Taps at Outer Radius								
7.01-1	4900	513.1	1464	92,380	31.5	21.7	92	306.3
7.01-2	4900	513.1	1362	85,940	31.5	21.7	92	306.3
7.01-3	4900	513.1	1273	80,330	31.5	21.7	92	306.3
7.01-4	4900	513.1	1176	74,200	31.5	21.7	92	306.3
7.01-5	4900	513.1	1063	67,080	31.5	21.7	92	306.3
7.02-1	3920	419.5	1167	73,640	31.5	21.7	93	306.9
7.02-2	3920	410.5	1087	68,600	31.5	21.7	93	306.9
7.02-3	3920	410.5	1016	64,110	31.5	21.7	93	306.9
7.02-4	3920	410.5	848	53,510	31.5	21.7	91	305.8

Table 7. Summary of Blade Pressure Tests (Continued)

Test No.	Speed rpm	Speed rad/s	Flow gpm	Flow cm^3/s	Inlet Total Pressure psig	Inlet Total Pressure N/cm^2	Temperature ^oF	Temperature ^oK
16^o (.28 rad) Sweepback, Pressure Taps at Outer Radius								
7.03-1	4900	513.1	1362	85,940	31.5	21.7	93	306.9
7.03-2	4900	513.1	1362	85,940	11.9	8.2	93	306.9
7.03-3	4900	513.1	1362	85,940	2.1	1.4	93	306.9
7.03-4	4900	513.1	1362	85,940	-4.8	-3.3	93	306.9
7.03-5	4900	513.1	1362	85,940	-7.3	-5.0	93	306.9
7.04-1	4900	513.1	1272	80,270	31.5	21.7	92	306.3
7.04-2	4900	513.1	1272	80,270	11.0	7.6	92	306.3
7.04-3	4900	513.1	1272	80,270	1.4	1.0	92	306.3
7.04-4	4900	513.1	1272	80,270	-7.7	-5.3	93	306.9
7.04-5	4900	513.1	1272	80,270	-8.2	-5.6	93	306.9
7.05-1	4900	513.1	1272	80,270	31.5	21.7	93	306.9
7.05-2	4900	513.1	1272	80,270	3.6	2.5	94	307.4
7.05-3	4900	513.1	1272	80,270	-4.9	-3.4	94	307.4
7.05-4	4900	513.1	1272	80,270	-8.2	-5.6	94	307.4
7.05-5	4900	513.1	1233	77,800	-10.3	-7.1	95	308.0
16^o (.28 rad) Sweepback, Pressure Taps at Inner Radius								
7.11-1	4900	513.1	1462	92,260	31.5	21.7	86	303.0
7.11-2	4900	513.1	1360	85,820	31.5	21.7	93	306.9
7.11-3	4900	513.1	1273	80,330	31.5	21.7	97	309.1
7.11-4	4900	513.1	1174	74,080	31.5	21.7	108	315.2
7.12-1	3920	410.5	1160	73,200	31.5	21.7	119	321.3
7.12-2	3920	410.5	1093	68,970	31.5	21.7	122	323.0
7.12-3	3920	410.5	1021	64,430	31.5	21.7	108	315.2
7.12-4	3920	410.5	845	53,320	31.5	21.7	96	308.6

Table 7. Summary of Blade Pressure Tests (Continued)

Test No.	Speed		Flow		Inlet Total Pressure		Temperature	
	rpm	rad/s	gpm	cm^3/s	psig	N/cm^2	^oF	^oK
7.13-1	4900	513.1	1362	85,940	31.3	21.6	86	303.0
7.13-2	4900	513.1	1362	85,940	11.5	7.9	87	303.6
7.13-3	4900	513.1	1362	85,940	0.8	0.6	87.5	303.8
7.13-4	4900	513.1	1362	85,940	-3.1	-2.1	88	304.1
7.13-5	4900	513.1	1317	83,100	-8.5	05.9	88	304.1
7,14-1	4900	513.1	1272	80,270	31.3	21.6	87	303.6
7.14-2	4900	513.1	1272	80,270	4.5	3.1	88	304.1
7.14-3	4900	513.1	1272	80,270	1.3	0.9	88	304.1
7.14-4	4900	513.1	1272	80,270	-3.9	-2.7	87	303.6
7.14-5	4900	513.1	1211	76,420	-8.7	-6.0	87	303.6

Table 8. Operating Points Used in Computer Program Development

Point No.	Speed (%)	$\bar{\Phi}$	$\bar{\Psi}$	NPSH (ft)	NPSH (m)	Run No.	Radius
8^o (.14 rad) Sweepback							
1	100	0.090	.165	39.1	11.9	6.08-3	2
2	100	0.090	.165	20.6	6.28	6.08-4	2
3	100	0.084	.177	18.1	5.52	6.09-3	2
4	80	0.096	.140	105.6	32.2	6.10-1	1
5	80	0.090	.164	105.6	32.2	6.10-2	1
6	80	0.084	.182	105.6	32.2	6.10-3	1
7	80	0.070	.216	105.6	32.2	6.10-4	1
8	100	0.090	.163	105.5	32.2	6.11-2	1
9	100	0.070	.213	105.4	32.1	6.11-4	1
10	100	0.094	.143	60.4	18.4	6.12-2	1
11	100	0.094	.148	35.7	10.9	6.12-3	1
12	100	0.094	.156	16.0	4.88	6.12-4	1
13	100	0.090	.162	60.7	18.5	6.13-2	1
14	100	0.090	.162	37.9	11.6	6.13-3	1
15	100	0.090	.164	16.8	5.12	6.13-4	1
16	100	0.084	.179	60.2	18.3	6.14-2	1
17	100	0.084	.178	37.0	11.3	6.14-3	1
18	100	0.084	.176	17.0	5.18	6.14-4	1
16^o (.28 rad) Sweepback							
19	100	0.084	.180	105.5	32.2	7.01-3	1
20	100	0.078	.193	105.5	32.2	7.01-4	1
21	100	0.070	.210	105.5	32.2	7.01-5	1
22	100	0.090	.162	60.0	18.3	7.03-2	1
23	100	0.090	.161	37.2	11.3	7.03-3	1
24	100	0.084	.178	60.0	18.3	7.04-2	1
25	100	0.084	.177	35.7	10.9	7.04-3	1
26	100	0.084	.167	14.5	4.42	7.04-4	1
27	100	0.084	.172	13.2	4.08	7.04-5	1
28	100	0.084	.178	40.6	12.4	7.05-2	1
29	100	0.084	.176	20.9	6.37	7.05-3	1
30	100	0.090	.165	25.2	7.68	7.13-4	2
31	100	0.087	.128	12.7	3.87	7.13-5	2
32	100	0.084	.176	23.4	7.13	7.14-4	2
33	100	0.080	.115	12.2	3.72	7.14-5	2

Table 9. Noncavitating Pressure Distribution; 8 deg (.14 rad) Sweepback, Tip Streamline
U_T = 120 ft/sec (36.4 m/s), NPSH = 106 ft (32.3m)

Pressure Tap Location	$\bar{\phi}$ = .096 Test 6.10-1				$\bar{\phi}$ = .090 Test 6.10-2			
	Suction Surface		Pressure Surface		Suction Surface		Pressure Surface	
	lb/in^2	N/cm^2	lb/in^2	N/cm^2	lb/in^2	N/cm^2	lb/in^2	N/cm^2
1*								
2*								
3**			-	-			-	-
4	25.7	17.7	-	-	26.1	18.0	-	-
5	-	-	51.7	35.6	-	-	52.1	35.9
6	34.7	23.9	51.7	35.6	35.1	24.2	54.1	37.3
7	38.7	26.7	52.7	36.3	38.3	26.4	54.5	37.6
8	38.2	26.3	61.2	42.2	38.4	26.5	> 56.3	> 38.8
9	45.7	31.5	51.2	35.3	45.4	31.3		
10***	45.7	31.5			45.4	31.3		
11***	53.2	37.0			52.2	36.0		
12***	51.7	35.6			51.7	35.6		
13	59.7	41.2	58.7	40.5	> 57.4	> 39.6		
14	60.7	41.8	63.7	43.9				
15	49.7	34.3	61.7	42.5				
16	-	-	57.7	39.8				
17	60.7	41.8	53.7	37.0				
18	59.2	40.8	-	-				
19	57.7	39.8	56.7	39.1				
20	55.7	38.4	-	-				
PH1	45.7	31.5			43.4	29.9		
PH2	51.7	35.4			52.6	36.3		
PH3	56.7	39.1			> 56.1	> 38.7		
PH4	59.7	41.2						
PH5	-	-						

"-" denotes missed reading due to blockage in pressure port
* Pressure tap location removed by sweepback
** Suction surface pressure tap location removed by sweepback
*** Pressure taps installed on suction surface only

Table 9. Noncavitating Pressure Distribution (Continued)

Pressure Tap Location	$\bar{\phi}$ = .084 Test 6.10-3				$\bar{\phi}$ = .070 Test 6.10-4			
	Suction Surface		Pressure Surface		Suction Surface		Pressure Surface	
	lb/in^2	N/cm^2	lb/in^2	N/cm^2	lb/in^2	N/cm^2	lb/in^2	N/cm^2
1*								
2*								
3**			-	-			-	-
4	25.8	17.8	-	-	16.5	11.4	-	-
5	-	-	55.7	38.4	-	-	53.1	36.6
6	36.0	24.8	> 57.1	> 39.4	40.3	27.8	> 55.8	> 38.5
7	40.2	27.7			41.8	28.8		
8	38.9	26.8			40.5	27.9		
9	46.9	32.3			46.8	32.3		
10	46.2	31.9			47.8	33.0		
11	53.1	36.6			> 54.8	> 37.8		
12	54.4	37.5						
13	> 59.3	> 40.9						
PH1	45.2	31.2			45.3	31.2		
PH2	53.1	36.6			53.5	36.9		
PH3	55.1	38.0			53.6	37.0		
PH4	57.3	39.5			> 57.2	> 39.4		
PH5	-	-						

Table 10. Noncavitating Pressure Distribution; 8 deg (.14 rad) Sweepback, Tip Streamline
U_T = 150 ft/sec (45.6 m/s), NPSH = 106 ft (32.3m)

Pressure Tap Location	$\bar{\phi}$ = .090 Test 6.11-2				$\bar{\phi}$ = .070 Test 6.11-4			
	Suction Surface		Pressure Surface		Suction Surface		Pressure Surface	
	lb/in^2	N/cm^2	lb/in^2	N/cm^2	lb/in^2	N/cm^2	lb/in^2	N/cm^2
1*								
2*								
3**			-	-			-	-
4	1.7	1.2	>24.0	>16.5	3.2	2.2	28.2	19.4
5	-	-			-	-	27.7	19.1
6	13.7	9.4			15.7	10.8	>29.7	>20.5
7	>21.5	>14.8			21.7	15.0		
8					14.7	10.1		
9					24.7	17.0		
10					>28.2	>19.4		
PH1	>22.2	>15.3			21.9	15.1		
PH2					26.9	18.5		
PH3					>28.8	>19.9		

"-" denotes missed reading due to blockage in pressure port
* Pressure tap location removed by sweepback
** Suction surface pressure tap location removed by sweepback

Table 11. Cavitating Pressure Distribution; 8 deg (.14 rad) Sweepback, Tip Streamline
U_T = 150 ft/sec (45.6 m/s), $\bar{\emptyset}$ = .094

Pressure Tap Location	NPSH = 60.4 ft (18.4m) Test 6.12-2				NPSH = 35.7 ft (10.9m) Test 6.12-3			
	Suction Surface		Pressure Surface		Suction Surface		Pressure Surface	
	lb/in^2	N/cm^2	lb/in^2	N/cm^2	lb/in^2	N/cm^2	lb/in^2	N/cm^2
1*								
2*								
3**			-	-			-	-
4	6.9	4.8	> 23.1	> 15.9	7.9	5.4	> 24.1	> 16.6
5	-	-			-	-		
6	9.3	6.4			8.9	6.1		
7	15.6	10.8			7.5	5.2		
8	-	-			-	-		
9	-	-			-	-		
10***	> 24.3	> 16.8			7.9	5.4		
11***					13.9	9.6		
12***					> 24.3	> 16.8		
PH1	22.9	15.8			14.4	9.9		
PH2	23.3	16.1			23.7	16.3		
PH3	> 25.8	> 17.8			> 25.6	> 17.7		

"-" denotes missed reading due to blockage in pressure port
* Pressure tap location removed by sweepback
** Suction surface pressure tap location removed by sweepback
*** Pressure taps installed on suction surface only

Table 11. Cavitating Pressure Distribution (Continued)

Pressure Tap Location	NPSH = 16.0 ft (4.9m) Test 6.12-4			
	Suction Surface		Pressure Surface	
	lb/in^2	N/cm^2	lb/in^2	N/cm^2
1*				
2*				
3**			-	-
4	7.2	5.0	8.7	6.0
5	-	-	9.4	6.5
6	8.7	6.0	6.8	4.7
7	7.0	4.8	-	-
8	-	-	-	-
9	-	-	13.4	9.2
10***	7.2	5.0		
11***	10.2	7.0		
12***	6.9	4.8		
13	1.0	4.8	-	-
14	9.0	6.2	> 23.5	> 16.2
15	-	-		
16	-	-		
17	> 24.4	> 16.8		
PH1	10.0	6.9		
PH2	6.6	4.6		
PH3	9.6	6.6		
PH4	> 24.3	> 16.8		

Table 12. Cavitating Pressure Distribution; 8 deg (.14 rad) Sweepback, Tip Streamline
U_T = 150 ft/sec (45.6 m/s), $\emptyset$ = .090

Pressure Tap Location	NPSH = 6.07 ft (18.5m) Test 6.13-2				NPSH = 37.9 ft (11.6m) Test 6.13-3			
	Suction Surface		Pressure Surface		Suction Surface		Pressure Surface	
	lb/in^2	N/cm^2	lb/in^2	N/cm^2	lb/in^2	N/cm^2	lb/in^2	N/cm^2
1*								
2*								
3**			-	-			-	-
4	6.9	4.8	> 23.7	> 16.3	3.9	2.7	> 27.5	> 19.0
5	-	-			-	-		
6	9.0	6.2			8.2	5.7		
7	-	-			4.2	2.9		
8	14.5	10.0			9.7	6.7		
9	> 24.6	> 17.0			-	-		
10***					3.9	2.7		
11***					12.7	8.8		
12***					> 29.7	> 20.5		
PH1	22.0	15.2			13.2	9.1		
PH2	22.0	15.2			27.2	18.8		
PH3	> 24.3	> 16.8			> 28.2	> 19.4		

"-" denotes missed reading due to blockage in pressure port
* Pressure tap location removed by sweepback
** Suction surface pressure tap location removed by sweepback
*** Pressure taps installed on suction surface only

Table 12. Cavitating Pressure Distribution (Continued)

Pressure Tap Location	NPSH = 16.8 ft (5.12m) Test 6.13-4			
	Suction Surface		Pressure Surface	
	lb/in^2	N/cm^2	lb/in^2	N/cm^2
1*				
2*				
3**			-	-
4	4.2	2.9	4.7	3.2
5	-	-	4.2	2.9
6	6.2	4.3	-	-
7	4.2	2.9	20.2	13.9
8	9.2	6.3	8.2	5.7
9	-	-	-	-
10***	4.2	2.9		
11***	8.2	5.7		
12***	4.2	2.9		
13	4.2	2.9	-	-
14	4.7	3.2	>27.7	>19.1
15	-	-		
16	-	-		
17	>28.7	>19.8		
PH1	6.7	4.6		
PH2	5.2	3.6		
PH3	10.4	7.2		
PH4	>28.2	>19.4		

Table 13. Cavitating Pressure Distribution; 8 deg (.14 rad) Sweepback, Tip Streamline
U_T = 150 ft/sec (45.6 m/s), $\emptyset$ = .084

Pressure Tap Location	NPSH = 60.2 ft (18.3m) Test 6.14-2				NPSH = 37.0 ft (11.3m) Test 6.14-3			
	Suction Surface		Pressure Surface		Suction Surface		Pressure Surface	
	lb/in^2	N/cm^2	lb/in^2	N/cm^2	lb/in^2	N/cm^2	lb/in^2	N/cm^2
1*								
2*								
3**			-	-			-	-
4	3.2	2.2	>28.2	>19.4	3.7	2.6	>27.7	>19.1
5	-	-			-	-		
6	1.7	1.2			5.7	3.9		
7	-	-			4.2	2.9		
8	14.2	9.8			9.2	6.3		
9	-	-			-	-		
10	>28.7	>19.8			5.7	3.9		
11					12.2	8.4		
12					>29.2	>20.1		
PH1	23.2	16.0			12.7	8.8		
PH2	27.7	19.1			27.7	19.1		
PH3	>30.2	>20.8			>29.2	>20.1		

"-" denotes missed reading due to blockage in pressure port
* Pressure tap location removed by sweepback
** Suction surface pressure tap location removed by sweepback

Table 13. Cavitating Pressure Distribution (Continued)

Pressure Tap Location	NPSH = 17.0 ft (5.2m) Test 6.14-4			
	Suction Surface		Pressure Surface	
	lb/in^2	N/cm^2	lb/in^2	N/cm^2
1*				
2*				
3**			-	-
4	4.2	2.9	5.2	3.6
5	-	-	-	-
6	5.7	3.9	4.2	2.9
7	4.7	3.2	> 28.7	> 19.8
8	9.7	6.7		
9	-	-		
10	4.7	3.2		
11	7.2	5.0		
12	4.2	2.9		
13	4.7	3.2		
14	4.7	3.2		
15	4.7	3.2		
16	-	-		
17	> 29.7	> 20.5		
PH1	9.7	6.7		
PH2	4.2	2.9		
PH3	17.7	12.2		
PH4	> 29.2	> 20.1		

Table 14. Cavitating Pressure Distribution; 8 deg (.14 rad) Sweepback, Midspan Streamline
U_T = 150 ft/sec (45.6 m/s)

Pressure Tap Location	NPSH = 39.1 ft (11.9m) $\bar{\emptyset}$ = .090 Test 6.08-3				NPSH = 20.6 ft (6.3m) $\bar{\emptyset}$ = .090 Test 6.08-4			
	Suction Surface		Pressure Surface		Suction Surface		Pressure Surface	
	lb/in^2	N/cm^2	lb/in^2	N/cm^2	lb/in^2	N/cm^2	lb/in^2	N/cm^2
1	5.1	3.5	-	-	1.8	1.2	-	-
2	5.3	3.7	> 13.8	> 9.5	3.1	2.1	2.2	1.5
3	5.1	3.5			1.7	1.2	1.7	1.2
4	13.5	9.3			1.5	1.0	1.7	1.2
5	12.7	8.8			1.6	1.1	1.6	1.1
6	11.9	8.2			1.7	1.2	5.2	3.6
7	-	-			1.6	1.1	1.6	1.1
8	> 10.9	> 7.5			1.0	0.7	5.5	3.8
9					-		1.5	1.0
10***					1.5	1.0		
11***					1.6	1.1		
12***					5.1	3.5		
13					1.8	1.2	5.9	4.1
14					> 7.6	> 5.2	-	-
15							> 9.6	> 6.6
PH1	> 11.7	> 8.1			1.9	1.3		
PH2					3.8	2.6		
PH3					6.1	4.2		
PH4					> 9.4	> 6.5		

"-" denotes missed reading due to blockage in pressure port
*** Pressure taps installed on suction surface only

Table 14. Cavitating Pressure Distribution (Continued)

Pressure Tap Location	NPSH = 18.1 ft (5.5m) $\bar{\emptyset}$ = .084 Test 6.09-3			
	Suction Surface		Pressure Surface	
	lb/in^2	N/cm^2	lb/in^2	N/cm^2
1	1.9	1.3	-	-
2	2.5	1.7	2.3	1.6
3	1.5	1.0	1.5	1.0
4	1.0	0.7	2.7	1.9
5	4.8	3.3	1.0	0.7
6	1.5	1.0	3.0	2.6
7	3.3	2.3	1.3	0.1
8	1.0	0.7	3.6	2.5
9	1.9	1.3	1.3	0.9
10***	1.4	1.0		
11***	1.8	1.2		
12***	2.5	1.7		
13	2.6	1.8	3.0	2.1
14	3.4	2.3	3.5	2.4
15	3.4	2.3	4.5	3.1
16	-	-	2.7	1.9
17	-	-	-	-
18	> 8.9	> 6.1	-	-
19			-	-
20			> 8.5	> 5.9
PH1	1.7	1.2		
PH2	2.6	1.8		
PH3	3.0	2.1		
PH4	5.6	3.9		
PH5	> 8.9	> 6.1		

Table 15. Noncavitating Pressure Distribution; 16 deg (.28 rad) Sweepback, Tip Streamline
U_T = 150 ft/sec (45.6 m/s), NPSH = 106 ft (32.3m)

Pressure Tap Location	$\bar{\phi}$ = .084 Test 7.01-3				$\bar{\phi}$ = .078 Test 7.01-4			
	Suction Surface		Pressure Surface		Suction Surface		Pressure Surface	
	lb/in^2	N/cm^2	lb/in^2	N/cm^2	lb/in^2	N/cm^2	lb/in^2	N/cm^2
1*								
2*								
3*								
4*								
5*								
6**			> 18.7	>12.9			>18.7	>12.9
7	0.7	0.5			1.2	0.8		
8	-	-			9.2	6.3		
9	6.2	4.3			5.7	3.9		
10	> 18.2	>12.5			>17.7	>12.2		
PH1	17.7	12.2			16.2	11.2		
PH2	> 32.2	>22.2			> 32.7	>22.5		

"-" denotes missed reading due to blockage in pressure port
* Pressure tap location removed by sweepback
** Suction surface pressure tap location removed by sweepback

Table 15. Noncavitating Pressure Distribution (Continued)

Pressure Tap Location	$\bar{\emptyset}$ = .070 Test 7.01-5			
	Suction Surface		Pressure Surface	
	lb/in^2	N/cm^2	lb/in^2	N/cm^2
1*				
2*				
3*				
4*				
5*				
6**			> 18.2	> 12.5
7	0.7	0.5		
8	6.2	4.3		
9	5.2	3.6		
10	> 16.7	> 11.5		
PH1	15.2	10.5		
PH2	> 34.7	> 23.9		

Table 16. Cavitating Pressure Distribution; 16 deg (.28 rad) Sweepback, Tip Streamline
U_T = 150 ft/sec (45.6 m/s), Ø = .090

Pressure Tap Location	NPSH = 60.0 ft (18.3m) Test 7.03-2				NPSH = 37.2 ft (11.3m) Test 7.03-3			
	Suction Surface		Pressure Surface		Suction Surface		Pressure Surface	
	lb/in^2	N/cm^2	lb/in^2	N/cm^2	lb/in^2	N/cm^2	lb/in^2	N/cm^2
1*								
2*								
3*								
4*								
5*								
6**			13.2	9.1			3.7	2.6
7	0.9	0.6	9.2	6.3	0.7	0.5	6.2	4.3
8	0.7	0.5	3.9	2.7	0.9	0.6	3.2	2.2
9	0.7	0.5	3.2	2.2	0.7	0.5	2.2	1.5
10***	1.9	1.3			0.7	0.5		
11***	4.9	3.4			0.7	0.5		
12***	4.7	3.2			3.2	2.2		
13	-	-	>17.2	>11.9	-	-	7.7	5.3
14	>17.7	>12.2			9.2	6.3	5.9	4.1
15					3.2	2.2	-	-
16					>16.3	>11.2	-	-
17							>15.7	>10.8
PH1	1.7	1.2			1.7	1.2		
PH2	11.2	7.7			5.2	3.6		
PH3	>18.9	>13.0			8.7	6.0		
PH4					12.2	8.4		
PH5					12.7	8.8		

"-" denotes missed reading due to blockage in pressure port
* Pressure tap location removed by sweepback
** Suction surface pressure tap location removed by sweepback
*** Pressure taps installed on suction surface only

Table 17. Cavitating Pressure Distribution; 16 deg (.28 rad) Sweepback, Tip Streamline
U_T = 150 ft/sec (45.6 m/s), $\bar{\phi}$ = .084

Pressure Tap Location	NPSH = 60.0 ft (18.3m) Test 7.04-2				NPSH = 35.7 ft (10.9m) Test 7.04-3			
	Suction Surface		Pressure Surface		Suction Surface		Pressure Surface	
	lb/in^2	N/cm^2	lb/in^2	N/cm^2	lb/in^2	N/cm^2	lb/in^2	N/cm^2
1*								
2*								
3*								
4*								
5*								
6*•			> 16.7	> 11.5			3.7	2.6
7	0.7	0.5			3.7	2.6	7.7	5.3
8	1.2	0.8			0.7	0.5	6.7	4.6
9	1.2	0.8			3.2	2.2	3.7	2.6
10***	3.7	2.6			3.9	2.7		
11***	> 16.2	> 11.2			4.2	2.9		
12***					4.2	2.9		
13					-	-	9.7	6.7
14					11.2	7.7	8.2	5.7
15					8.2	5.7	-	-
16					> 16.2	> 11.2	-	-
17							> 18.2	> 12.5
PH1	15.2	10.5			2.2	1.5		
PH2	> 16.2	> 11.2			2.7	1.9		
PH3					8.7	6.0		
PH4					14.2	9.8		
PH5					> 17.7	> 12.2		

"-" denotes missed reading due to blockage in pressure port
* Pressure tap location removed by sweepback
** Suction surface pressure tap location removed by sweepback
*** Pressure taps installed on suction surface only

Table 17. Cavitating Pressure Distribution (Continued)

Pressure Tap Location	NPSH = 14.5 ft (4.4m) Test 7.04-4				NPSH = 13.2 ft (4.1m) Test 7.04-5			
	Suction Surface		Pressure Surface		Suction Surface		Pressure Surface	
	lb/in^2	N/cm^2	lb/in^2	N/cm^2	lb/in^2	N/cm^2	lb/in^2	N/cm^2
1*								
2*								
3*								
4*								
5*								
6**			0.7	0.5	1.2	0.8		
7	0.7	0.5	0.7	0.5	1.2	0.8	1.2	0.8
8	0.7	0.5	0.7	0.5	1.2	0.8	1.2	0.8
9	0.7	0.5	0.7	0.5	1.2	0.8	1.2	0.8
10***	0.7	0.5			1.2	0.8		
11***	0.7	0.5			1.2	0.8		
12***	0.7	0.5			1.2	0.8		
13	-	-	0.7	0.5	-	-	> 16.2	> 11.2
14	0.7	0.5	2.2	1.5	1.2	0.8		
15	0.7	0.5	-	-	1.2	0.8		
16	2.7	1.9	-	-	> 15.2	> 10.5		
17	4.7	3.2	> 10.2	> 7.0				
18	> 12.2	> 8.4						
PH1	0.7	0.5			1.2	0.8		
PH2	1.2	0.8			2.2	1.5		
PH3	0.7	0.5			14.7	10.1		
PH4	4.7	3.2			> 16.7	> 11.5		
PH5	> 7.7	> 5.3						

Table 17. Cavitating Pressure Distribution (Continued)

Pressure Tap Location	NPSH = 40.6 ft (12.4m) Test 7.05-2				NPSH = 20.9 ft (6.4m) Test 7.05-3			
	Suction Surface		Pressure Surface		Suction Surface		Pressure Surface	
	lb/in^2	N/cm^2	lb/in^2	N/cm^2	lb/in^2	N/cm^2	lb/in^2	N/cm^2
1*								
2*								
3*								
4*								
5*								
6**			> 21.2	> 14.6			0.7	0.5
7	0	0			0.7	0.5	-	-
8	0	0			0.7	0.5	0.7	0.5
9	0	0			0.7	0.5	> 20.7	> 14.3
10	0	0			0.7	0.5		
11	1.2	0.8			0.7	0.5		
12	2.2	1.5			0.7	0.5		
13	-	-			-	-		
14	> 21.2	> 14.6			> 22.7	> 15.7		
PH1	7.7	5.3			1.7	1.2		
PH2	20.7	14.3			0.7	0.5		
PH3	19.7	13.6			20.7	14.3		
PH4	> 21.7	> 15.0			> 22.7	> 15.7		

Table 18. Cavitating Pressure Distribution; 16 deg (.28 rad) Sweepback, Midspan Streamline
U_T = 150 ft/sec (45.6 m/s)

Pressure Tap Location	NPSH = 25.2 ft (7.68m) $\bar{\phi}$ = .090 Test 7.13-4				NPSH = 12.7 ft (3.87m) $\bar{\phi}$ = .087 Test 7.13-5			
	Suction Surface		Pressure Surface		Suction Surface		Pressure Surface	
	lb/in^2	N/cm^2	lb/in^2	N/cm^2	lb/in^2	N/cm^2	lb/in^2	N/cm^2
1*								
2*								
3*								
4**			1.2	0.8			1.2	0.8
5	-	-	-	-	-	-	1.2	0.8
6	-	-	> 22.2	> 15.3	-	-	1.2	0.8
7	-	-			1.2	0.8	1.2	0.8
8	1.7	1.2			0.7	0.5	1.2	0.8
9	2.7	1.9			0.7	0.5	1.2	0.8
10***	-	-			1.2	0.8		
11***	7.2	5.0			0.7	0.5		
12***	5.2	3.6			1.2	0.8		
13	11.2	7.7			0.7	0.5	1.2	0.8
14	> 25.7	> 17.7			1.2	0.8	-	-
15					-	-	-	-
16					> 24.7	> 17.0	-	-
17							> 26.2	> 18.1
PH1	5.7	3.9			1.2	0.8		
PH2	15.7	10.8			1.2	0.8		
PH3	23.7	16.3			2.7	1.9		
PH4	24.7	17.0			5.7	3.9		
PH5	> 25.7	> 17.7			> 24.2	> 16.7		

"-" denotes missed reading due to blockage in pressure port
* Pressure tap location removed by sweepback
** Suction surface pressure tap location removed by sweepback
*** Pressure taps installed on suction surface only

Table 18. Cavitating Pressure Distribution (Continued)

Pressure Tap Location	NPSH = 23.4 ft (7.13m) $\bar{\phi}$ = .084 Test 7.14-4				NPSH = 12.2 ft (3.72m) $\bar{\phi}$ = .080 Test 7.14-5			
	Suction Surface		Pressure Surface		Suction Surface		Pressure Surface	
	lb/in^2	N/cm^2	lb/in^2	N/cm^2	lb/in^2	N/cm^2	lb/in^2	N/cm^2
1*								
2*								
3*								
4**			1.2	0.8			1.2	0.8
5	-	-	1.7	1.2	-	-	0.7	0.5
6	-	-	1.7	1.2	-	-	1.2	0.8
7	1.2	0.8	3.2	2.2	1.2	0.8	0.7	0.5
8	1.2	0.8	1.7	1.2	0.7	0.5	1.2	0.8
9	-	-	24.2	16.7	1.2	0.8	1.2	0.8
10***	1.7	1.2			1.2	0.8		
11***	1.7	1.2			1.2	0.8		
12***	17.7	12.2			1.2	0.8		
13	1.7	1.2	>26.7	>18.4	1.2	0.8	1.2	0.8
14	>26.7	>18.4			1.2	0.8	-	-
15					-	-	-	-
16					1.7	1.2	-	-
17					-	-	>25.7	>17.7
18					3.7	2.6		
19					-	-		
20					2.2	1.5		
PH1	2.2	1.5			1.2	0.8		
PH2	3.7	2.6			1.2	0.8		
PH3	24.2	16.7			2.7	1.9		
PH4	26.2	18.1			4.7	3.2		
PH5	>26.7	>18.4			>23.7	>16.3		

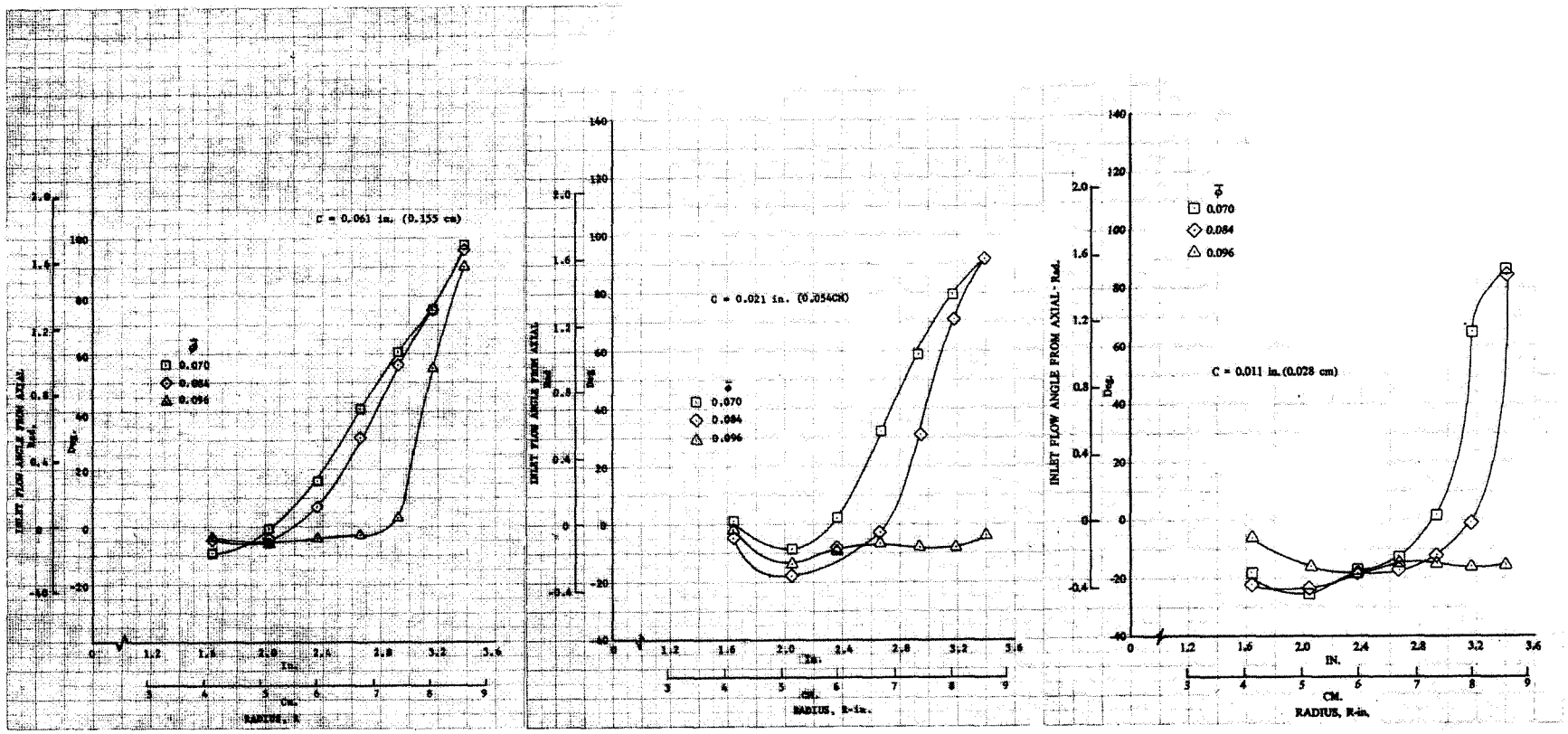

DF 91286 DF 85005 DF 85002

Figure 15. Radial Distribution of Inlet Flow Angle With Varying Blade Tip Clearance; U_T = 150 ft/sec (45.6 m/sec), NPSH = 106 ft (32.3 m)

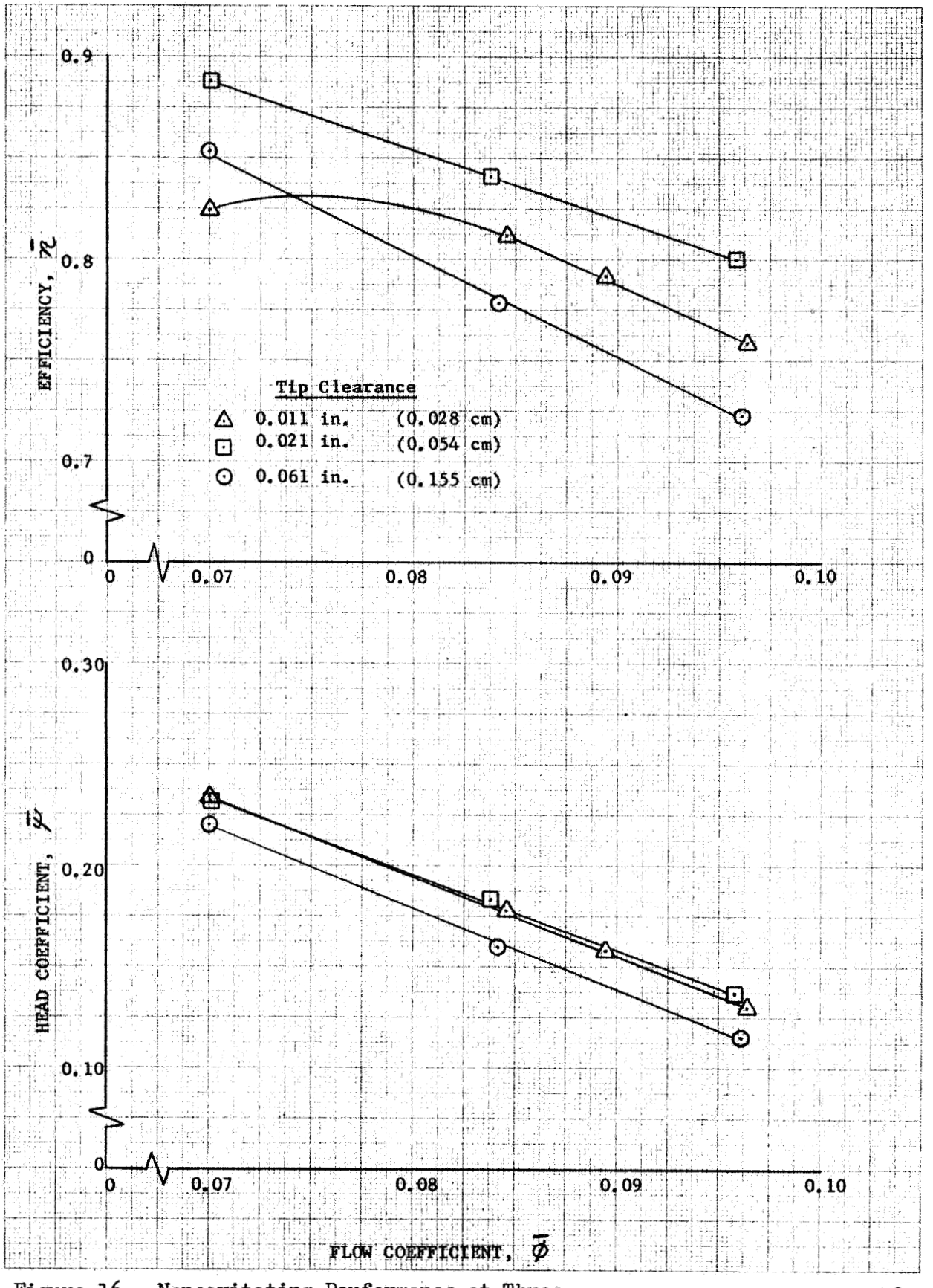

Figure 16. Noncavitating Performance at Three Blade Tip Clearances; U_T = 150 ft/sec (45.6 m/sec), NPSH = 106 ft (32.3m)

DF 91287

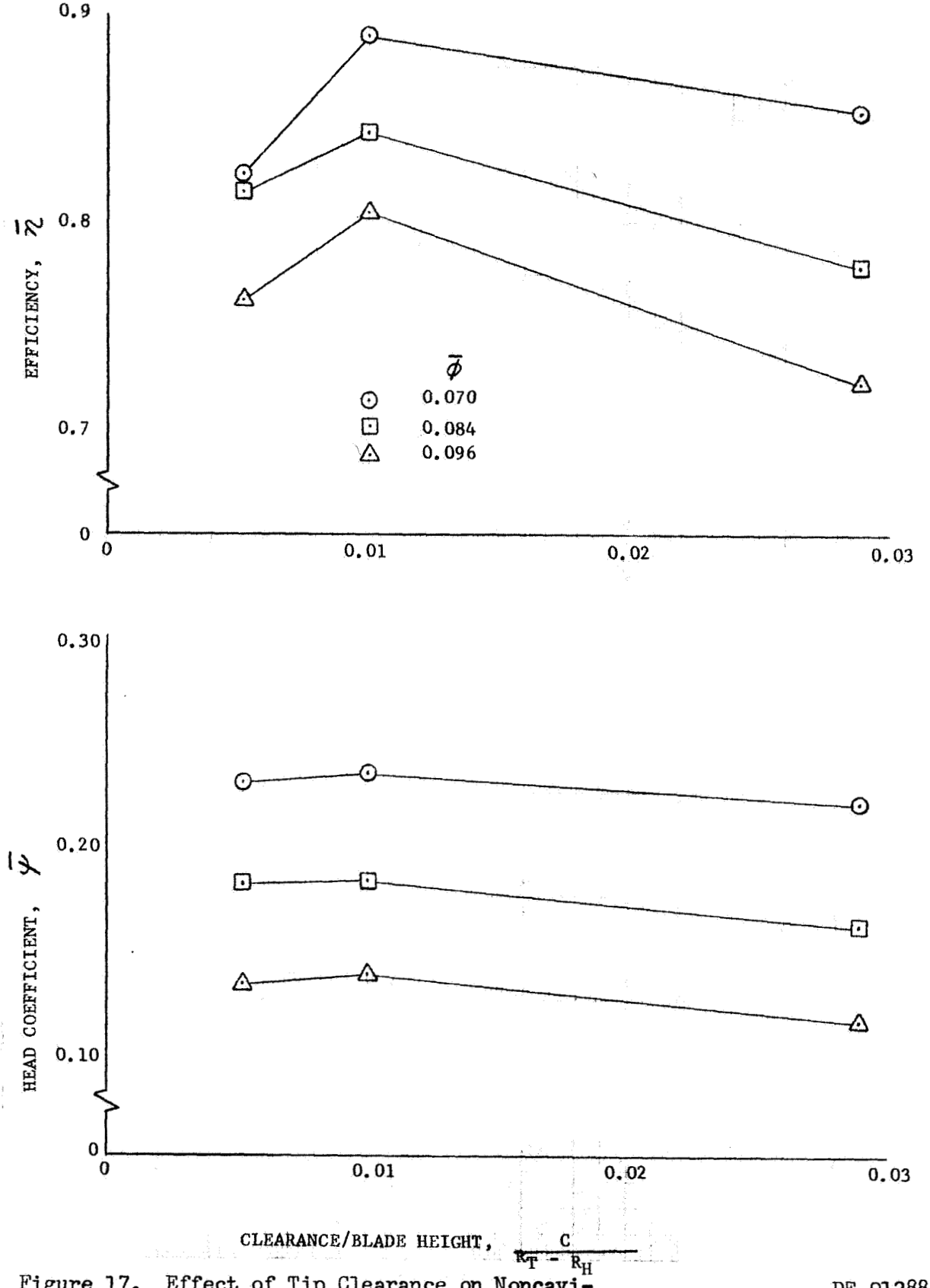

Figure 17. Effect of Tip Clearance on Noncavitating Performance; U_T = 150 ft/sec (45.6 m/sec), NPSH = 106 ft (32.3m)

DF 91288

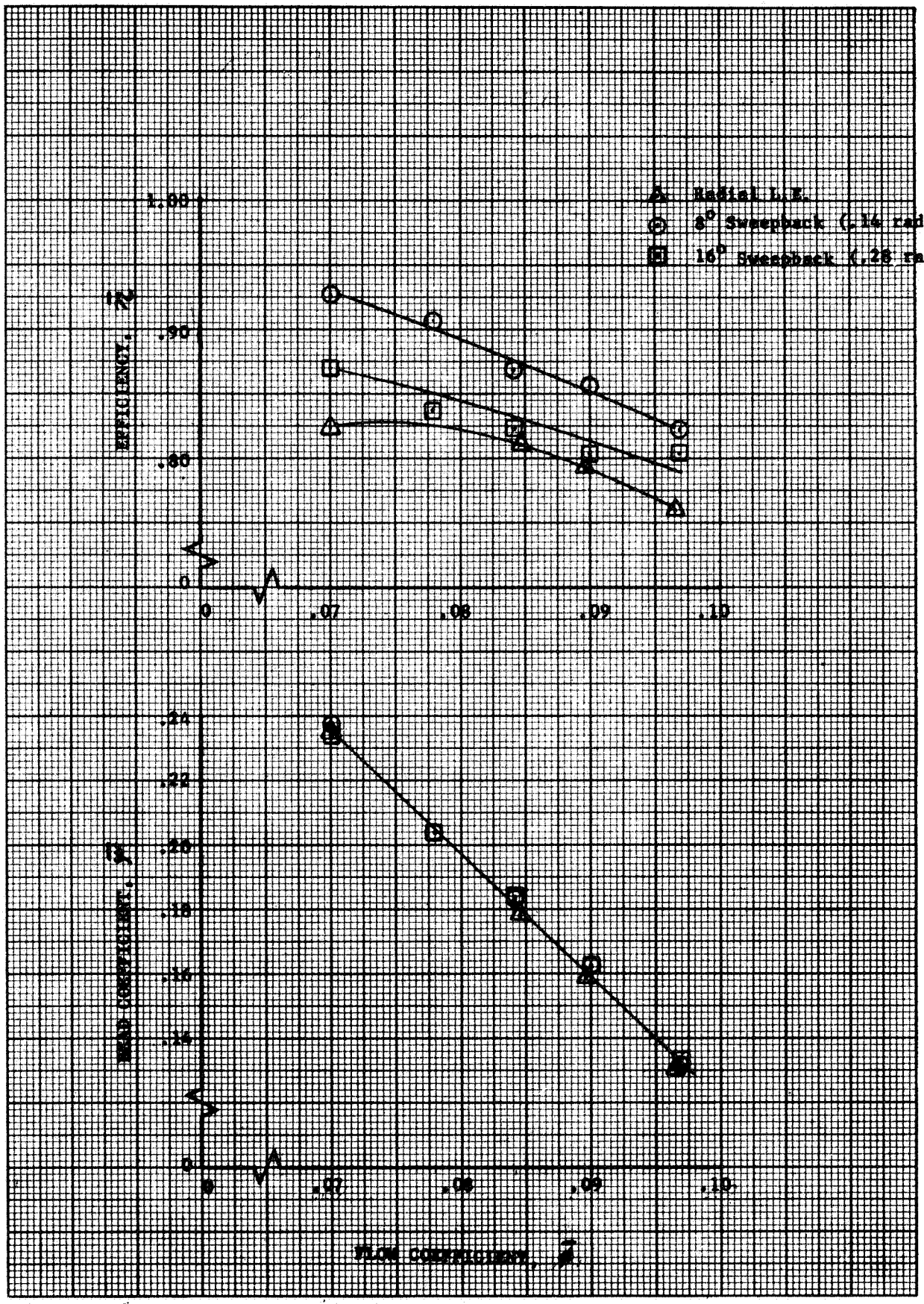

Figure 18. Noncavitating Performance for Three Leading Edge Sweepbacks; U_T = 150 ft/sec (45.6 m/sec), NPSH = 106 ft (32.3m)

DF 91289

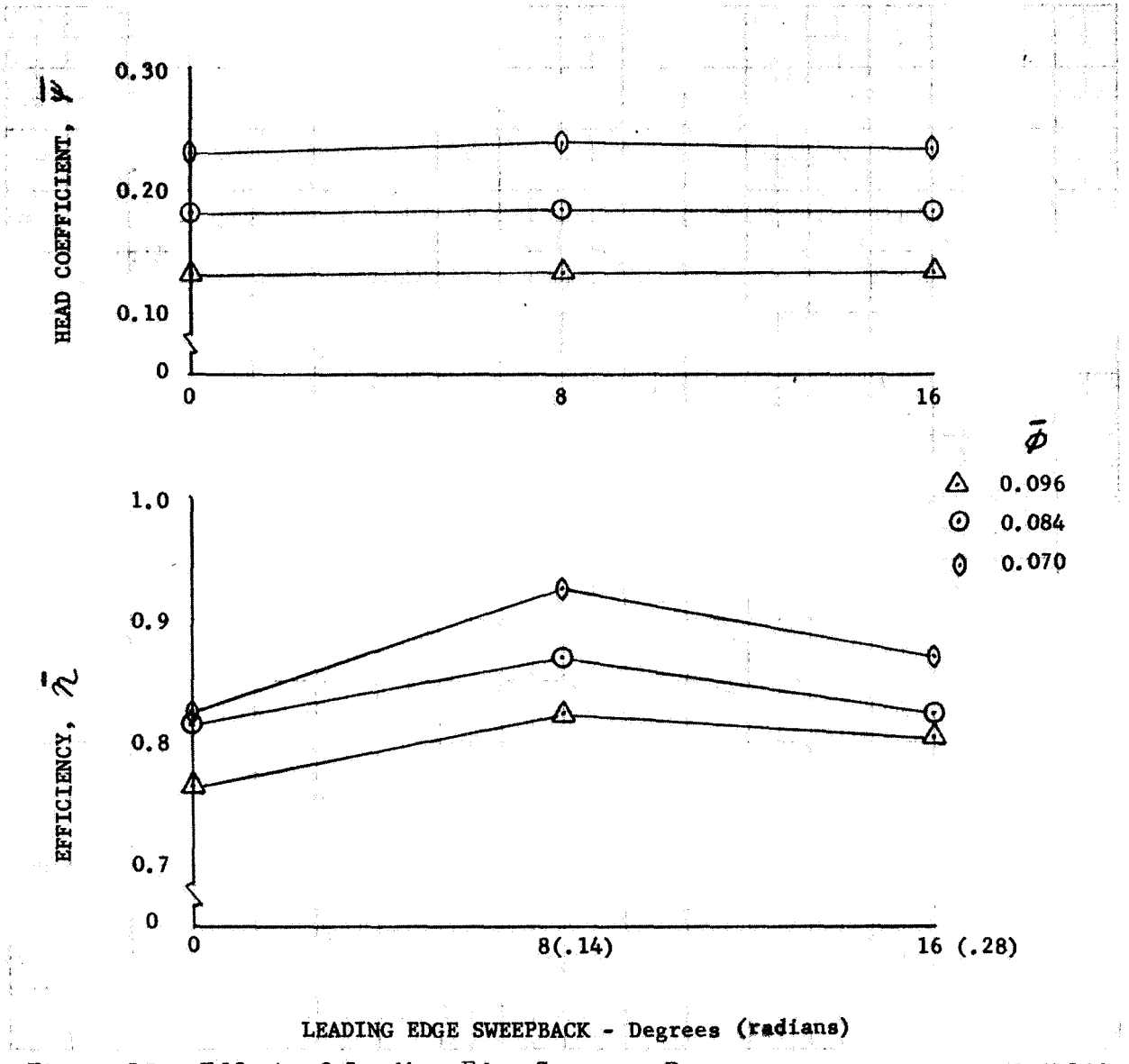

Figure 19. Effect of Leading Edge Sweep on Performance; U_T = 150 ft/sec (45.6 m/sec)

DF 91290

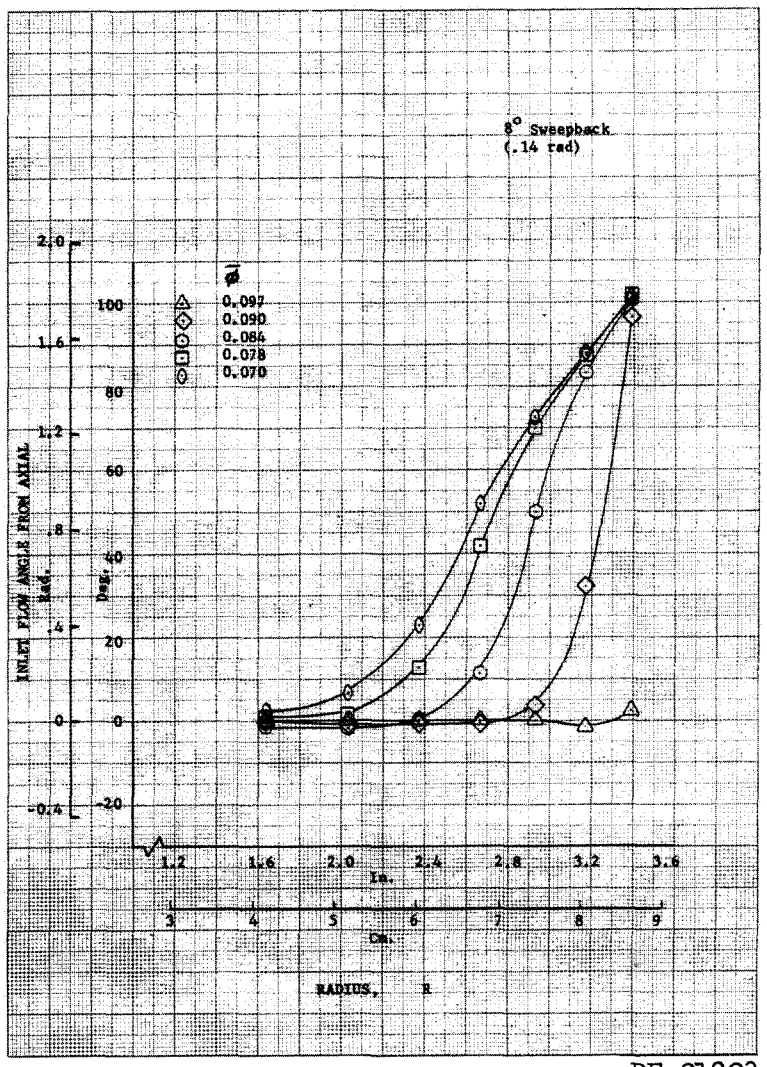

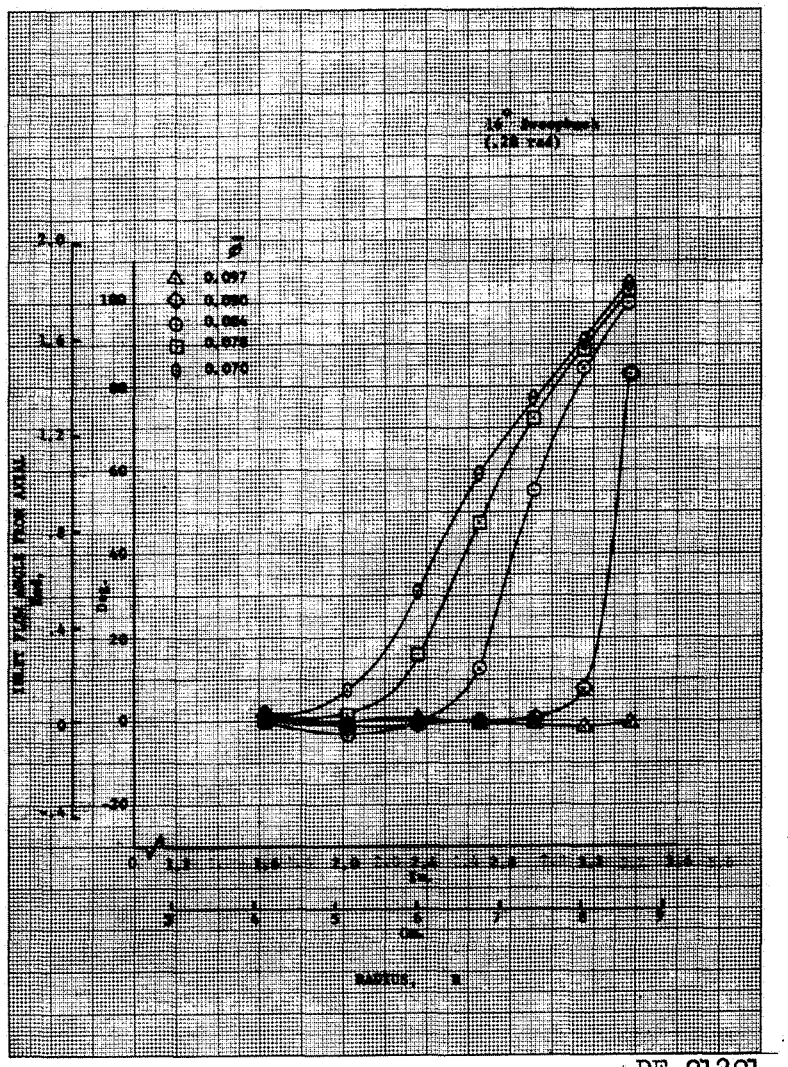

Figure 20. Radial Distribution of Inlet Flow Parameters; U_T = 150 ft/sec (45.6 m/sec), NPSH = 106 ft (32.3 m)

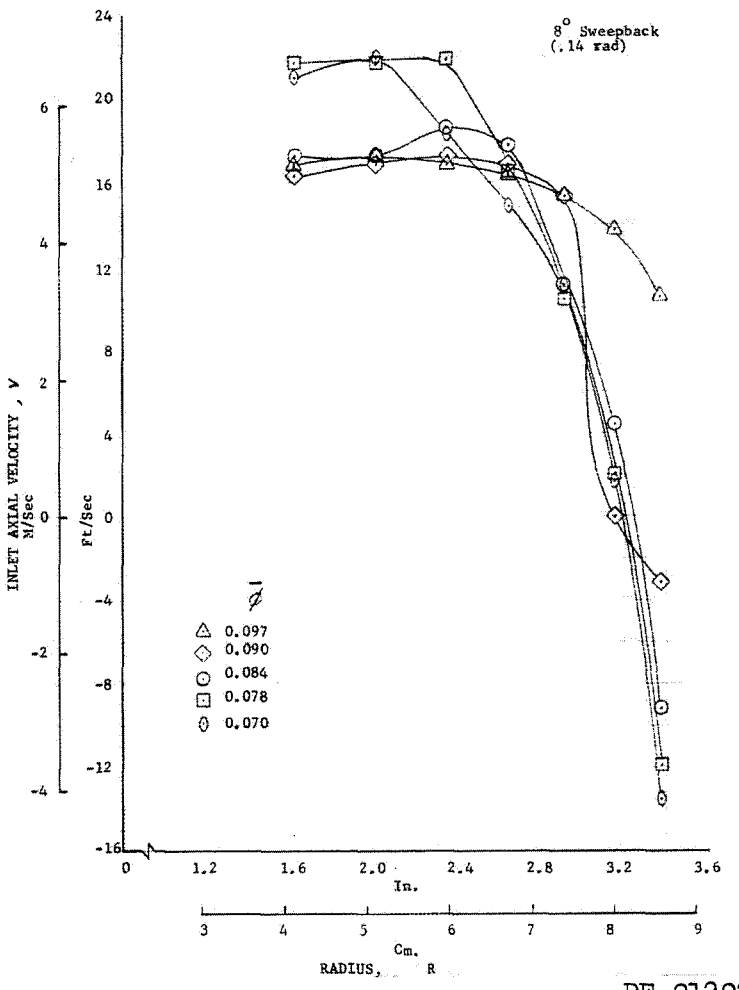

DF 91292

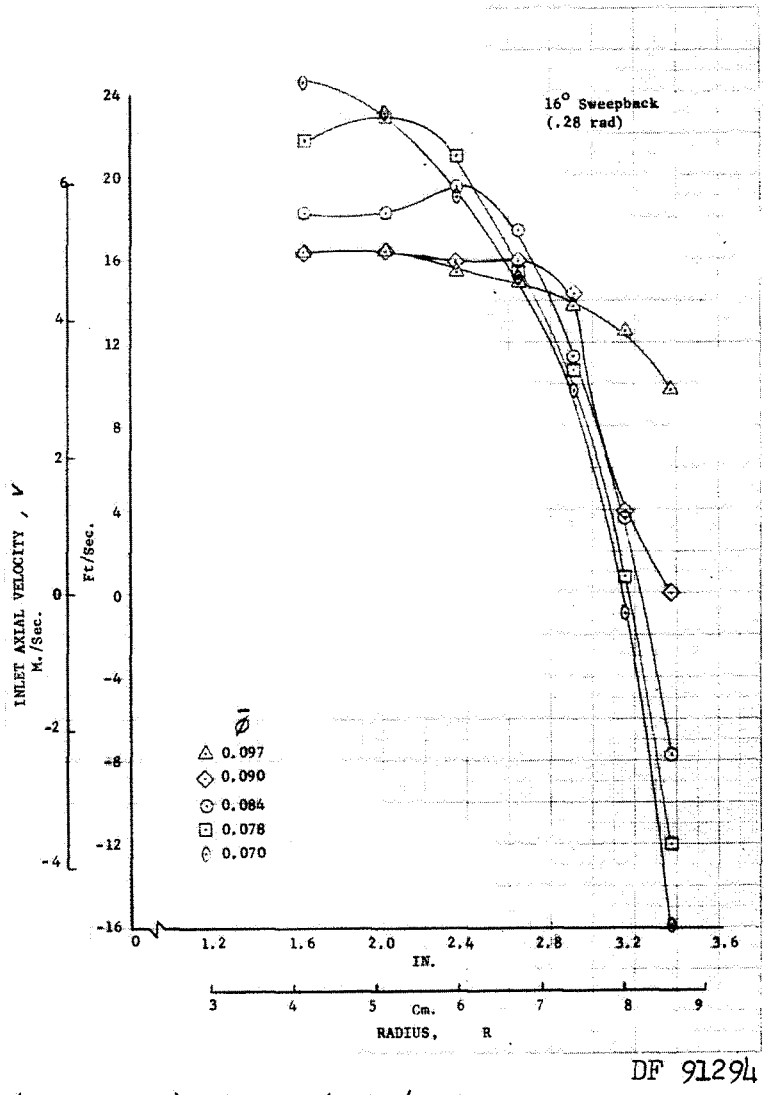

DF 91294

Figure 20. Radial Distribution of Inlet Flow Parameters (Continued); U_T = 150 ft/sec (45.6 m/sec), NPSH = 106 ft (32.3 m)

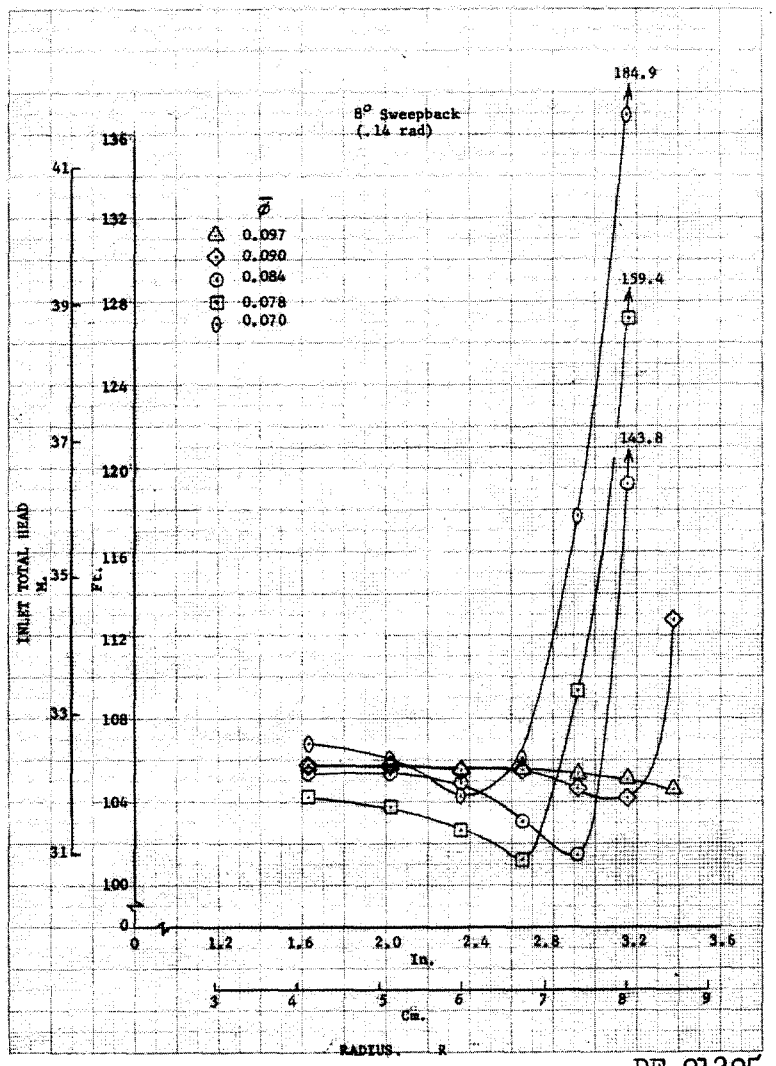

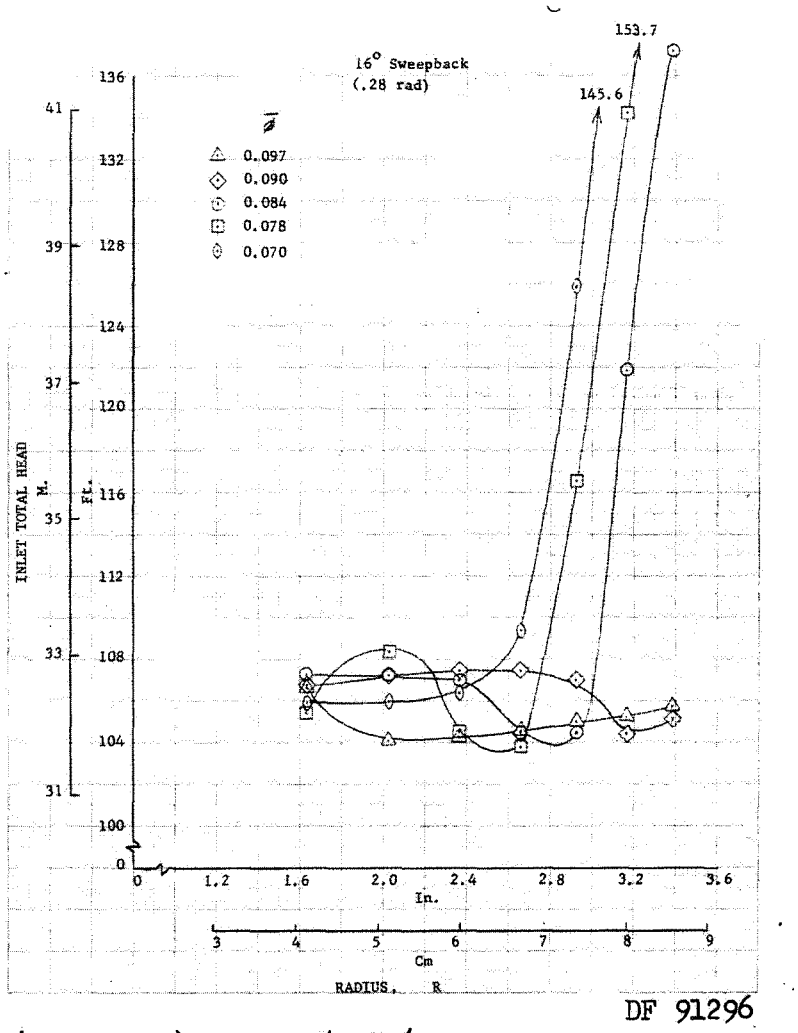

Figure 20. Radial Distribution of Inlet Flow Parameters (Continued); U_T = 150 ft/sec (45.6 m/sec), NPSH = 106 ft (32.3 m)

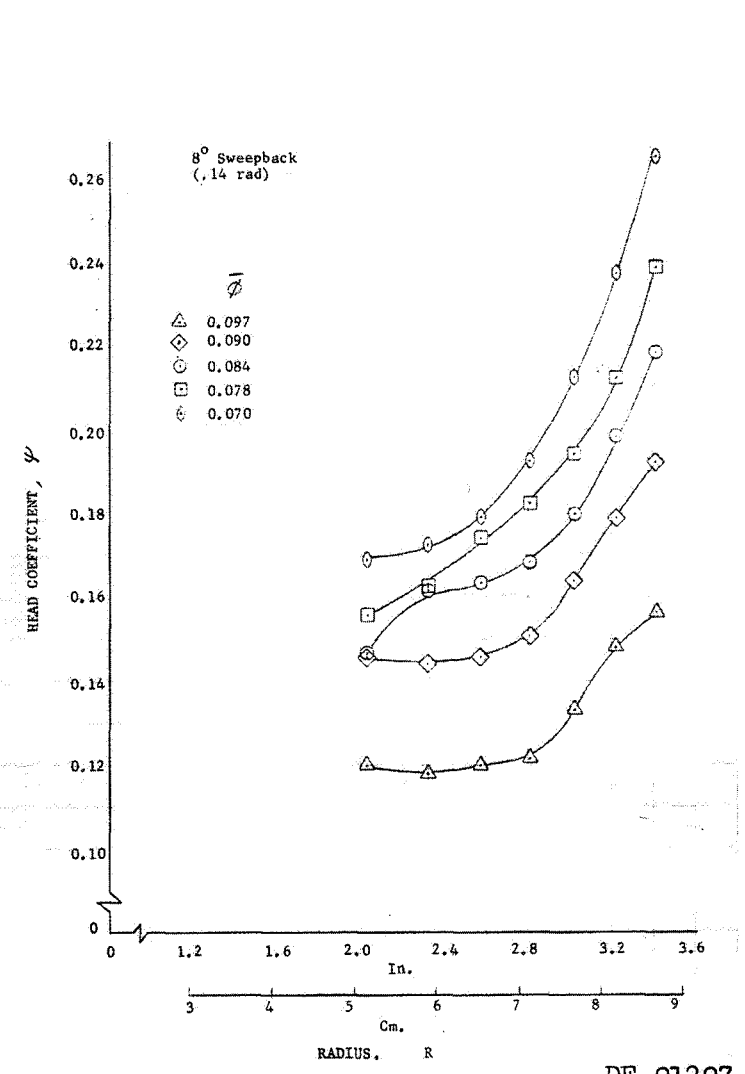

DF 91297

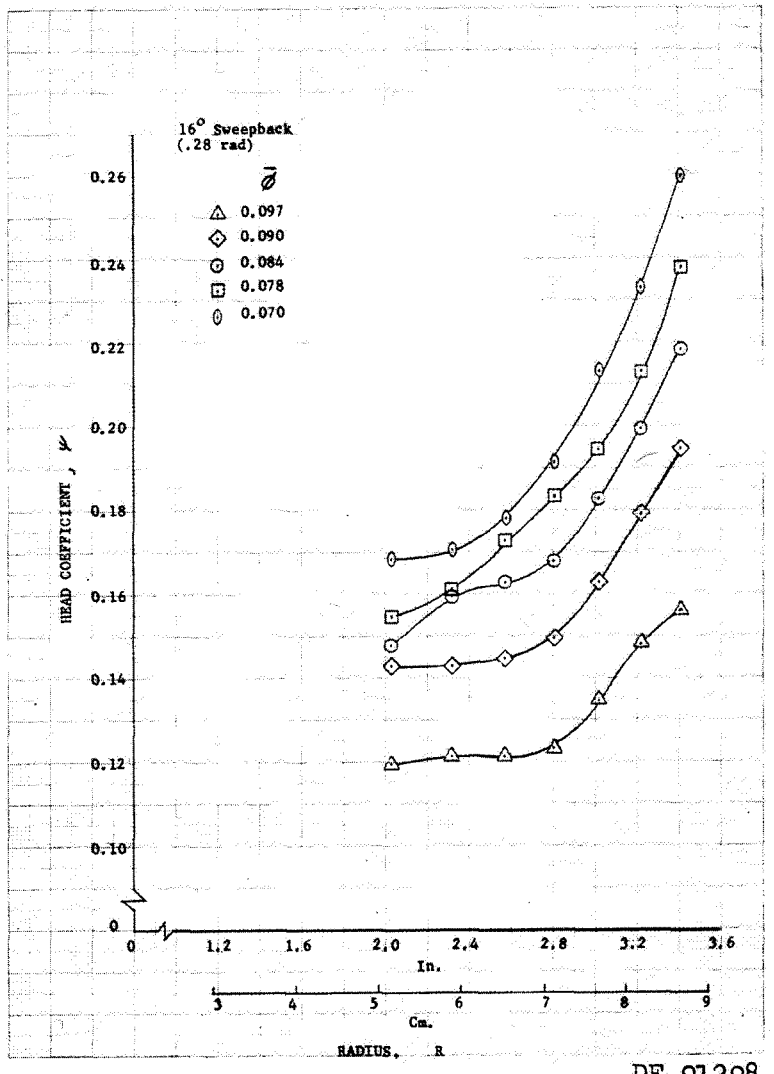

DF 91298

Figure 21. Radial Distribution of Discharge Flow Parameters; U_T = 150 ft/sec (45.6 m/sec), NPSH = 106 ft (32.3 m)

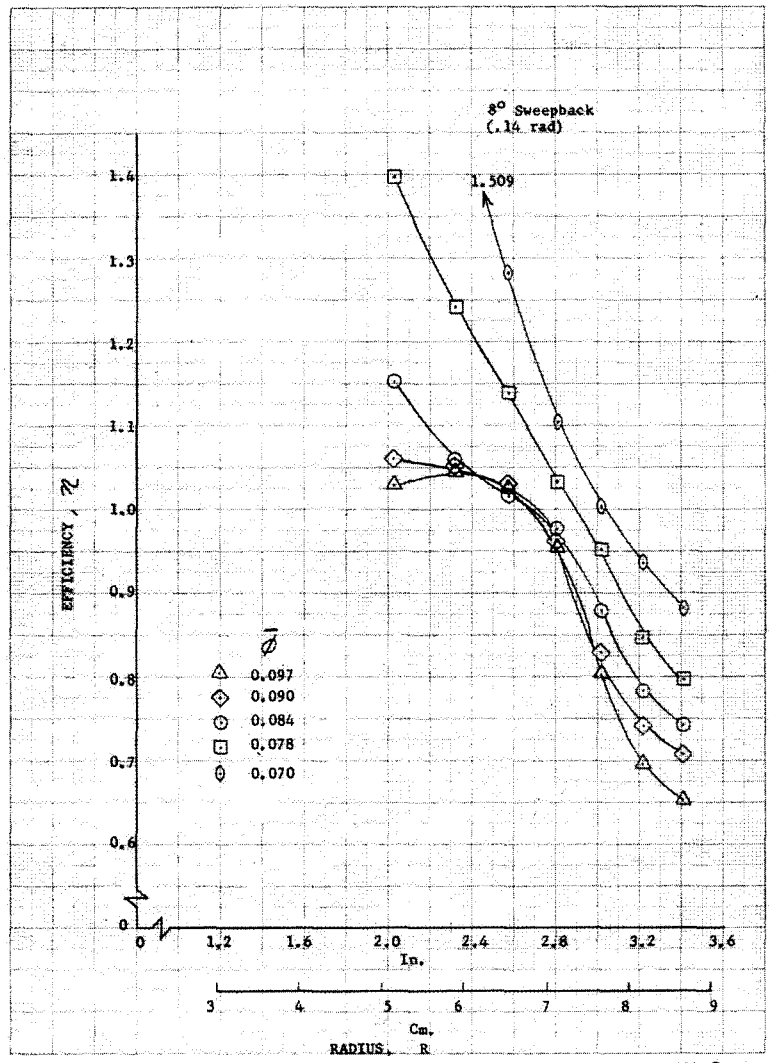

DF 91299

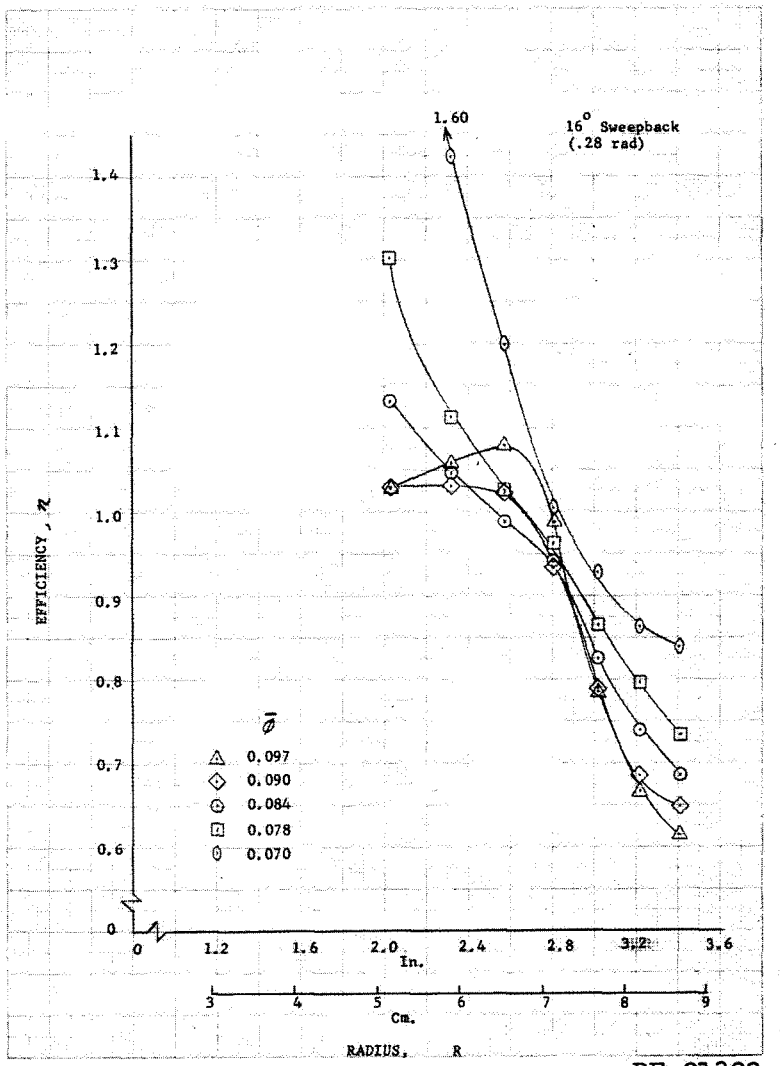

DF 91300

Figure 21. Radial Distribution of Discharge Flow Parameters (Continued); U_T = 150 ft/sec (45.6 m/sec), NPSH = 106 ft (32.3 m)

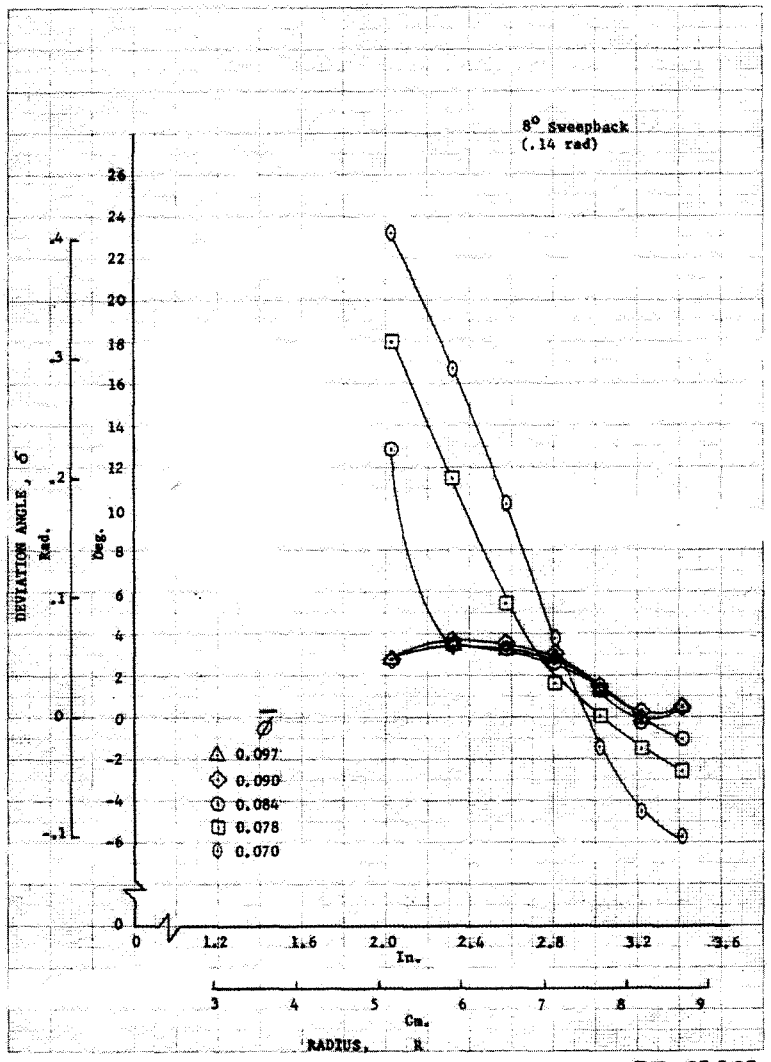

DF 91301

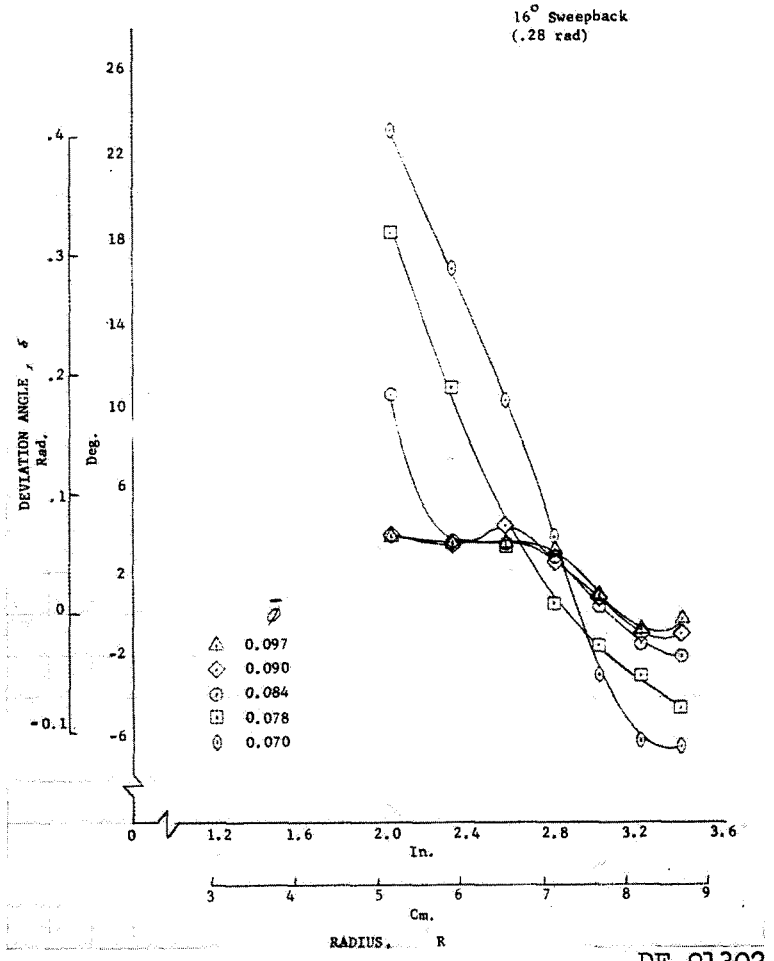

DF 91302

Figure 21. Radial Distribution of Discharge Flow Parameters (Continued); U_T = 150 ft/sec (45.6 m/sec), NPSH = 106 ft (32.3 m)

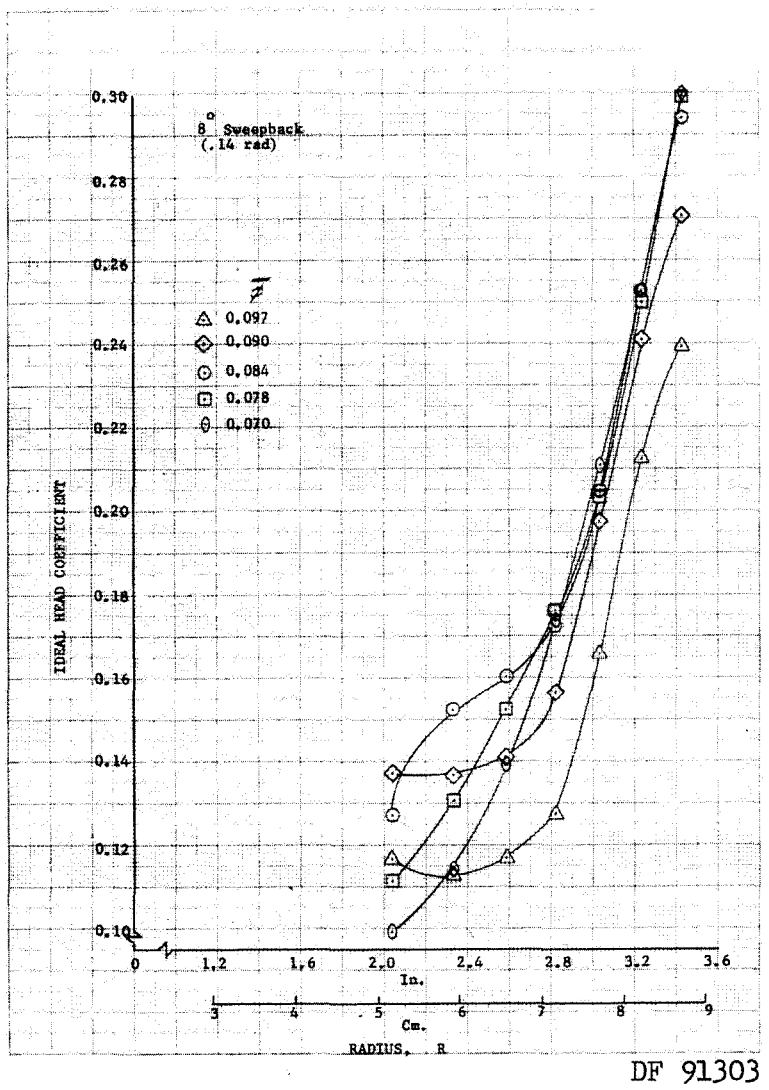

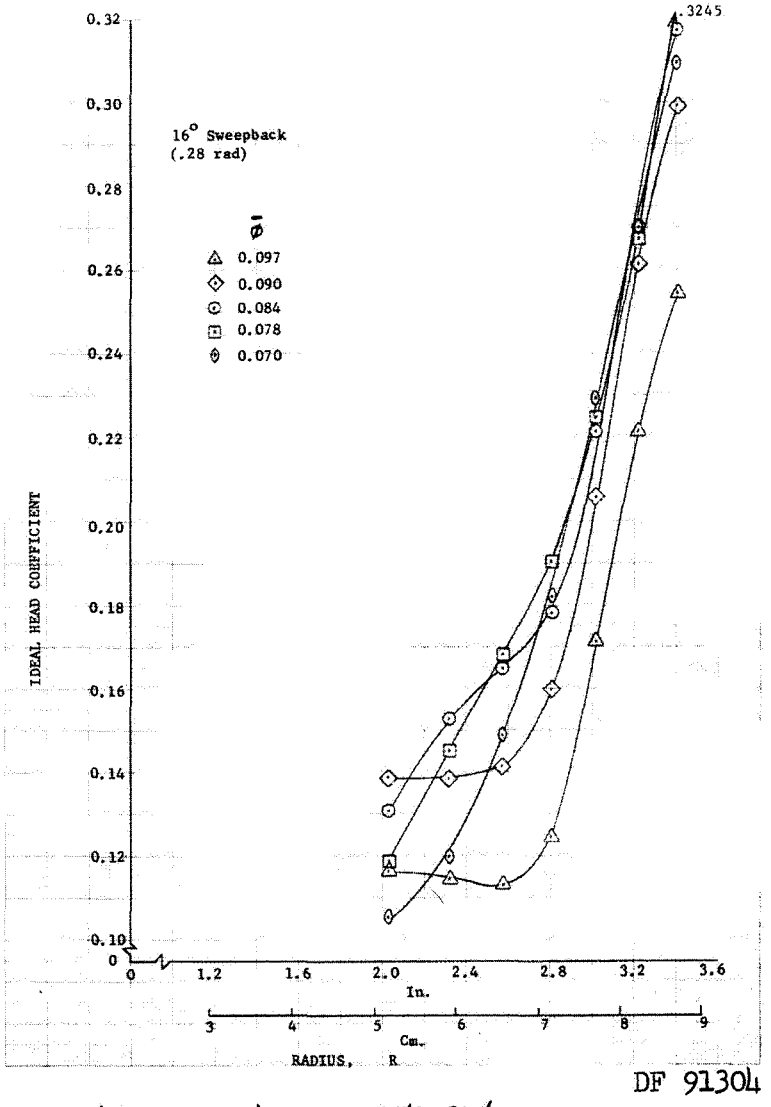

Figure 21. Radial Distribution of Discharge Flow Parameters (Continued); U_T = 150 ft/sec (45.6 m/sec), NPSH = 106 ft (32.3 m)

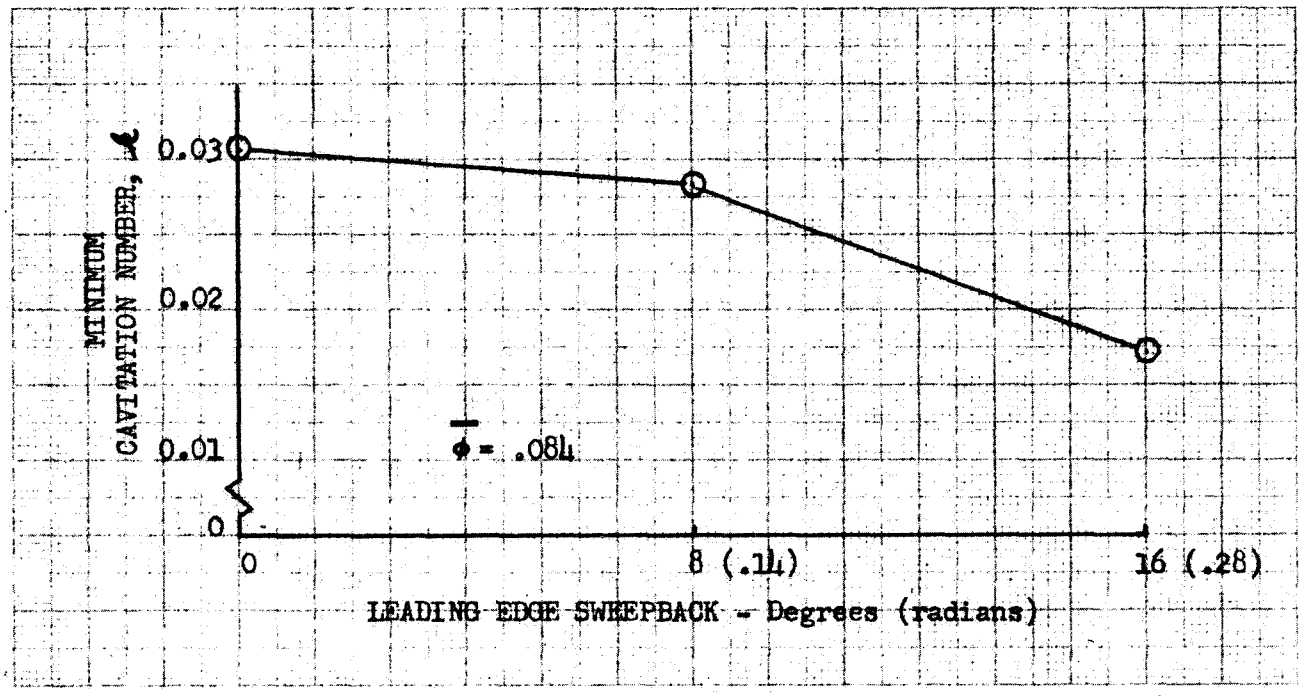

DF 94072

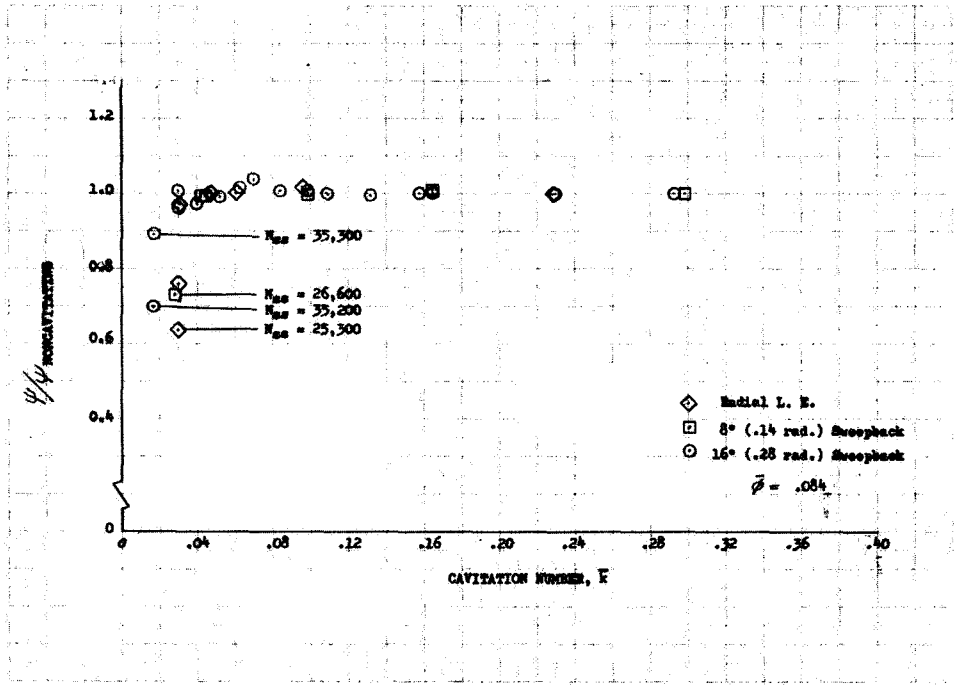

DF 91305

Figure 22. Effect of Sweepback on Inducer Suction Capability; U_T = 150 ft/sec (45.6 m/sec), C = .011 in (0.028 cm)

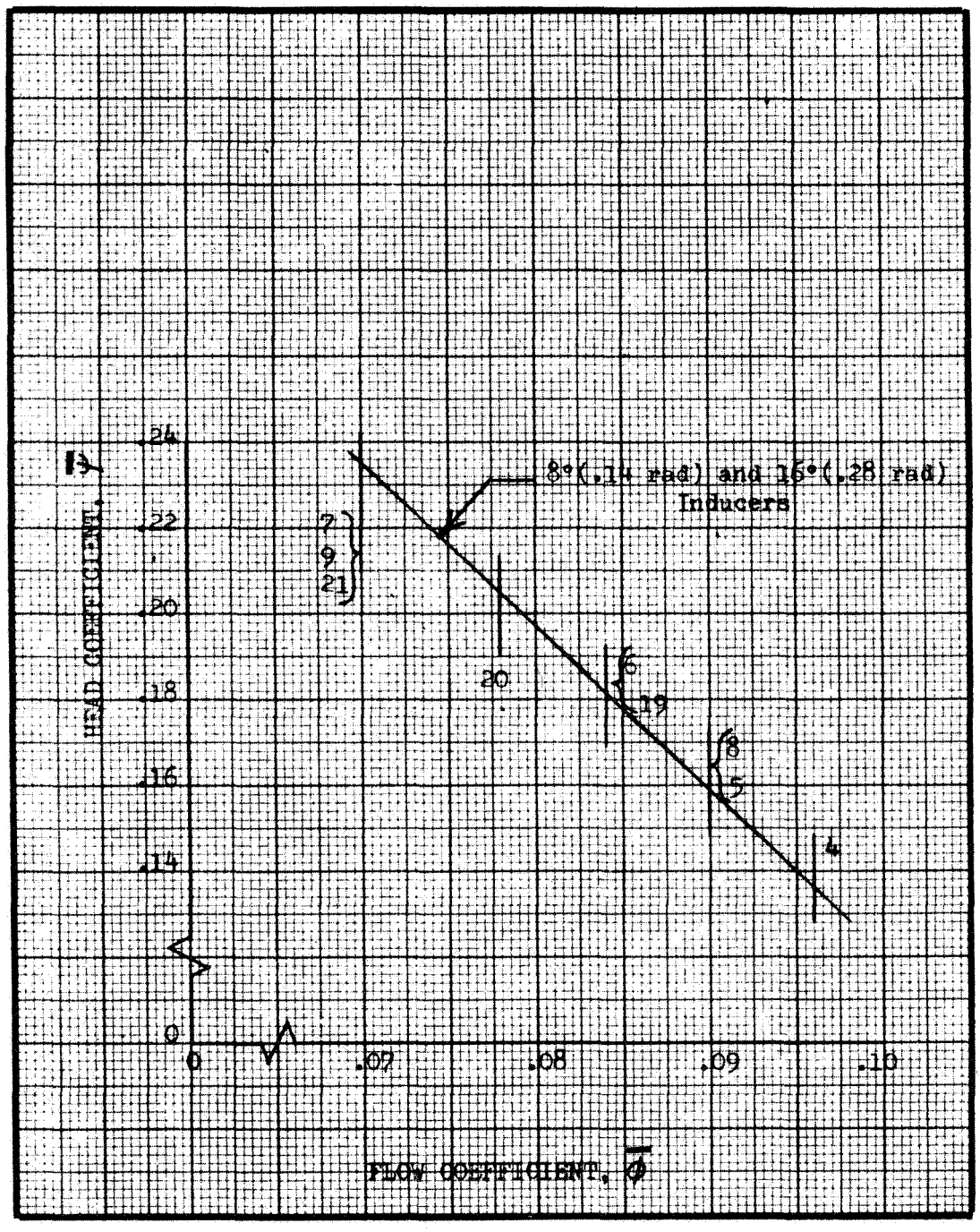

Figure 23. Summary of Noncavitating Performance Data Used in Computer Program Development

DF 91306

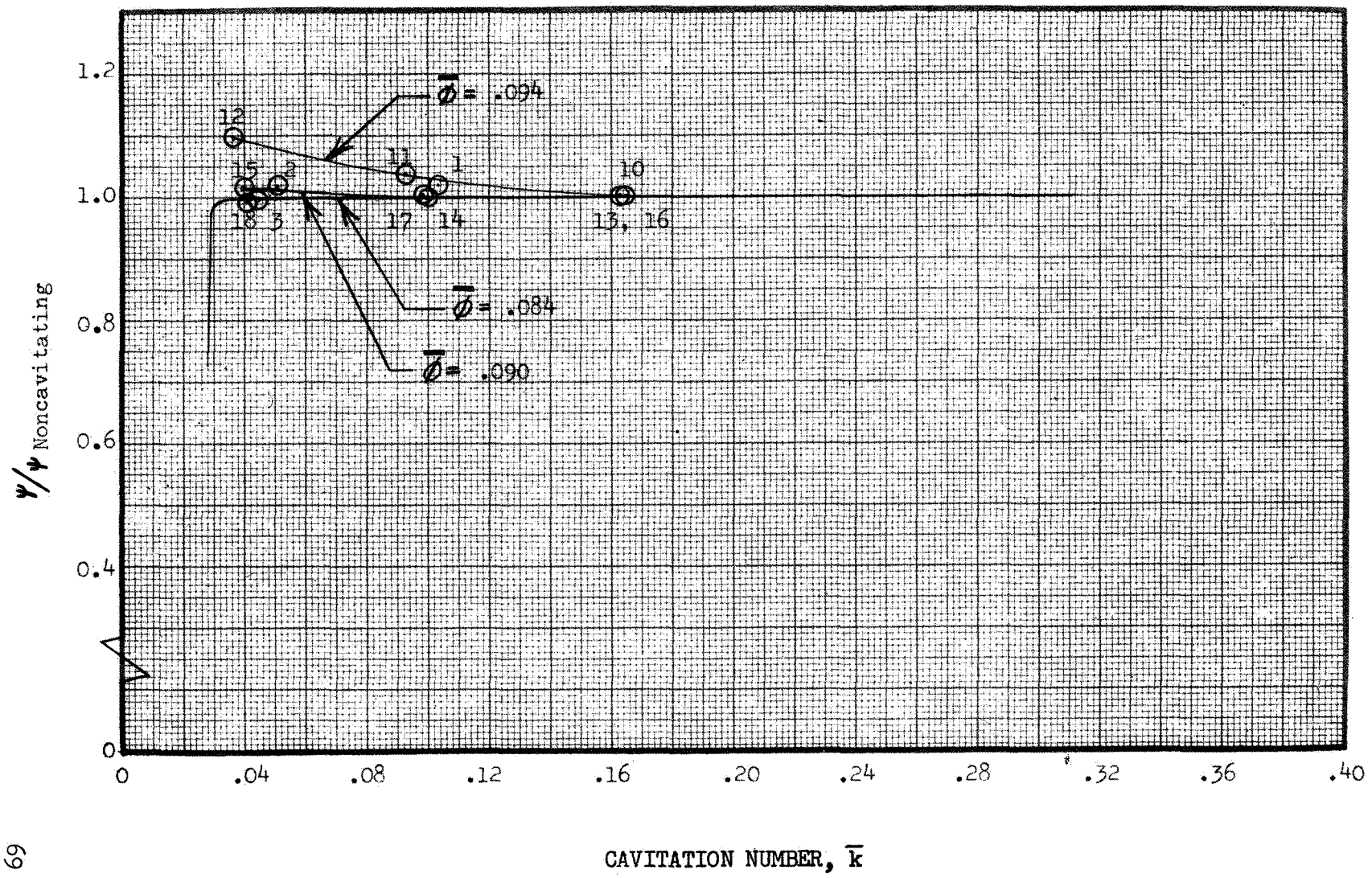

Figure 24. Summary of Cavitating Performance Data for 8 deg (.14 rad) Sweepback Inducer Used in Computer Program Development

DF 91307

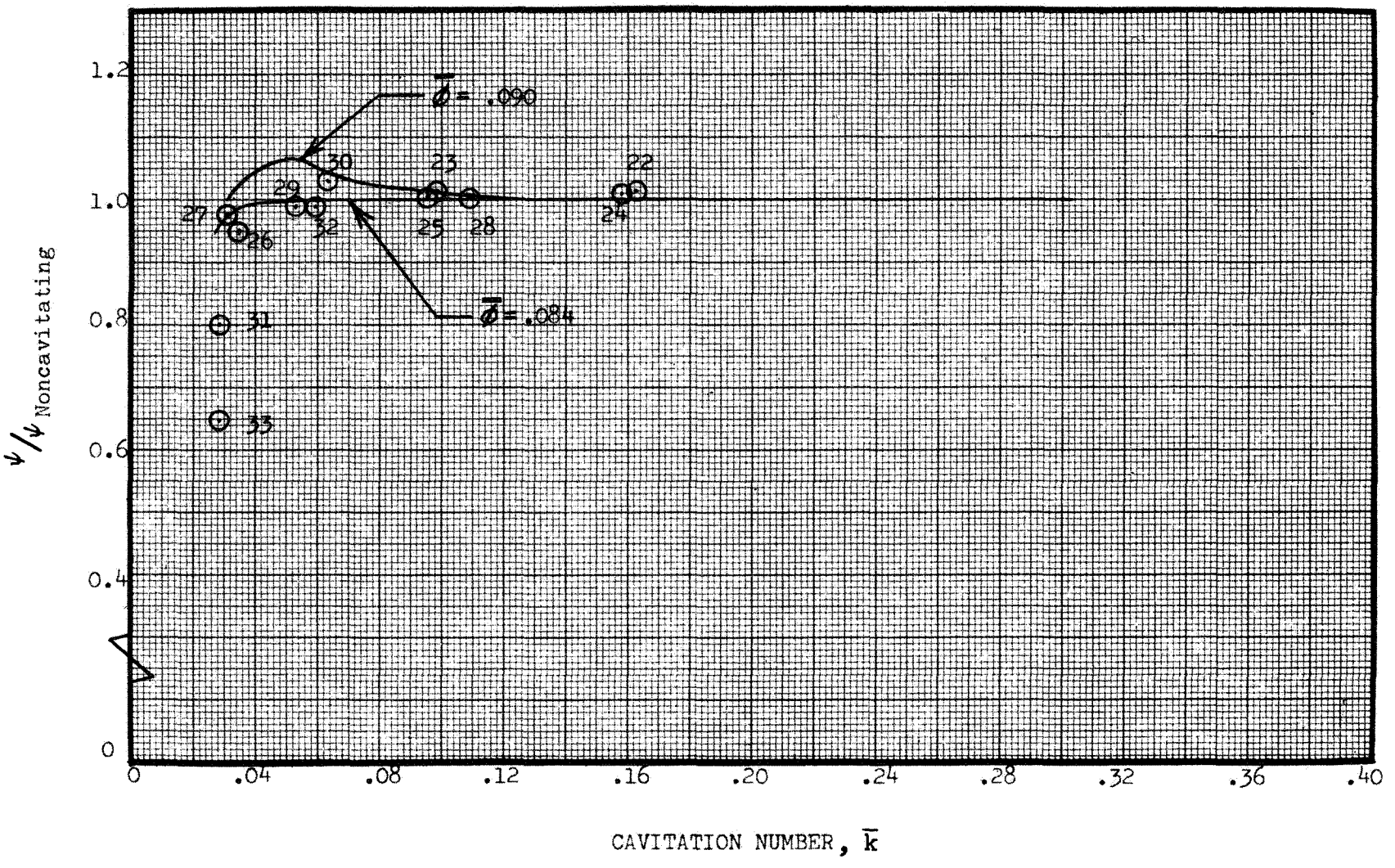

Figure 25. Summary of Cavitating Performance Data for 16 deg (.28 rad) Sweepback Inducer Used in Computer Program Development DF 91308

SECTION IV
ANALYSIS

A. Summary of Hydrodynamic Analyses

The basic flow analysis uses a mean streamline, two-dimensional meridional flow model. It is assumed that the average flow conditions in the blade-to-blade space can be represented on a meridional surface so that only a two-dimensional, streamline balancing analysis to satisfy radial momentum is required to establish mean velocities, pressures and flow angles for several radial locations at specified axial stations. A vapor cavity is assumed to exist at all times over some finite distance along the blade suction surface at the inducer inlet. This cavity, together with the adjacent blade, forms a channel for each stream tube which is bounded by two meridional streamlines. It is assumed that all the vapor is contained in the cavity and that the liquid flows in the bounded channel. This concept is based on the tendency of the liquid to be separated from the vapor due to centrifugal forces arising from curvature of the flow in the blade-to-blade space. Because the vapor merely displaces the liquid in the present flow model, it is considered that the actual blade can be replaced by a pseudo blade consisting of the real blade plus the cavity. The blade angle is replaced by the mean angle of the pseudo-blade; i.e., the average of the real blade angle and the angle of the surface of discontinuity between the vapor and the liquid measured from the same reference plane. This then produces a local flow "deviation" caused by cavitation, which will add to other deviation effects. These additional effects include leading edge incidence and trailing edge unloading due to circulation around the blades.

Viscous effects are also incorporated in the flow model. A boundary layer analysis determines the amount of flow blockage and momentum defect due to diffusion and to viscous shear forces at the blade surfaces and on the hub and shroud walls. The boundary layer blockage causes the meridional velocity to increase and reduces the work capability of the inducer. The momentum defect causes the mass-average total pressure to be reduced. Thus, the viscosity of the fluid affects both the head input and head output. The presence of a boundary layer and its effect on the cavity formation are also accounted for in the cavity model.

B. Tip Clearance Analysis

A tip clearance flow analysis was prepared and incorporated in the inducer hydrodynamic computer program to provide the program with the capability of predicting the effects of tip clearance on inducer performance. The analysis is described in this section and its formulation is included in the computer program of (2).

1. General Description of Analysis

A tip vortex flow model was selected to represent tip clearance effects based on the work of Rains (4) and Lakshminarayana (5). Observations of tip vortex flow patterns within inducers and other axial flow

turbomachinery have been reported by these and other investigators. The vortex forms as a result of the discontinuity between the inducer through flow and the tip clearance leakage flow and is assumed to consist of: (1) a central core where the fluid rotates as a solid body, and (2) a free vortex surrounding the central core. The vortex induces a secondary velocity component which is normal to the passage through flow and which causes a change in the flow angle. At the exit, this flow angle change results in additional flow deviation which reduces inducer ideal head. The formation of the vortex requires energy, a portion of which will not be recovered and therefore will represent an actual head loss.

Rains developed a theory for predicting the radius and circulation of the vortex core based on constant blade loading along the chord. Since an inducer blade does not experience constant loading, Rains basic differential equations were incorporated into the inducer internal flow analysis and solved for each station by the finite difference method. The spacing of the stations was sufficiently small that constant loading between stations could be assumed. Deviation angles which were calculated through the direct application of Rains equations were found to be unrealistically large and a correction factor was applied to the circulation to bring ideal head predictions into agreement with the test data. The correction was based on work done by Lakshminarayana (5) who related the circulation correction to a decrease in lift with tip clearance that had been measured by him and Horlock (6).

Tip clearance losses were calculated by the method of Lakshminarayana (5) who derived a semiempirical expression for the decrement in efficiency as a function of tip clearance to blade height ratio, blade angle, aspect ratio, flow coefficient, and ideal head coefficient. The ideal head used in this calculation was the value that was obtained using the empirically corrected circulation.

2. Vortex Model Formulation

The vortex flow model considered is shown in figure 26 where flow through the tip clearance from pressure to suction side of the blade causes a vortex to form on the suction side near the blade tip. The vortex rotates in a direction counter to the inducer and its radius increases with distance from the leading edge.

Rains (4) analyzed the flow by assuming incompressible, lossless flow from upstream (W_∞) to both the suction side (W_S) and the pressure side (W_P) of the blade, and through the tip clearance as shown in figure 27. W refers to a velocity vector which is relative to the blade. Tip leakage flow, which has a velocity W_P along the blade before passing through the clearance, is assumed to maintain this component of velocity after passing through the clearance, relative velocity pressures are assumed equal in both sides of the blade, and there is assumed to be no radial static pressure gradient in the tip clearance space. On the suction side, tip leakage flow has velocity W_S because it comes to the same dynamic pressure as suction side flow.

Interaction of tip leakage flow with suction side through flow is shown in figure 28. An observer at the blade leading edge looking in the "ℓ" direction would see tip leakage flowing to the left with velocity component W_S Sin (λ/2) and suction side through flow underneath flowing to the right with velocity component W_S Sin (λ/2), creating a plane of velocity discontinuity. Both flows would move away from the observer with velocity $W_\ell = W_S$ Cos (λ/2).

Rains replaced the discontinuity plane with a potential vortex sheet of strength $\gamma = 2W_S$ Sin (λ/2) and extending from the blade suction side to infinity in the "m" direction. The sheet moves in the "ℓ" direction with velocity W_ℓ being continuously formed at the blade leading edge. To account for the condition of no velocity into the inducer outer wall, a mirror image of the vortex and flow field is constructed as shown in figure 29.

Each vortex filament in a sheet induces a velocity in every other filament. Rains determined that a pair of semi-infinite vortex sheets would induce each other to roll up (figure 29) and that: (1) the roll up is approximately circular, (2) the circles remain nearly tangent to the sheets, and (3) there is little stretching of each sheet as it rolls up. With these assumptions the growth and roll up of the vortex sheet can be computed.

The rate of change of vortex radius "a" can be determined from the induced velocity (V_A) at point "A" (figure 29). Due to the two semi-infinite sheets, this velocity is:

$$V_A = 2\,\frac{da}{dt} = \frac{\gamma}{2\pi} \ln\left(1 + \frac{c}{a}\right) \quad \text{(downward)}$$

The rate of change of sheet length "b" rolled up can be determined from the induced velocity (V_o) of point "o" (figure 29). Due to the suction side through flow velocity component and the mirror image roll up, this velocity is:

$$V_o = \frac{db}{dt} = W_S \text{ Sin } (\lambda/2) - \frac{\Gamma}{4\pi\,(a+c)} \quad \text{(toward blade)}$$

where "Γ" is the circulation of that portion of the sheet which is rolled up, and "b" is the length of sheet rolled up.

Consider a length of vortex sheet "$d\ell$" formed at the blade leading edge and released to move in the "ℓ" direction. Such a sheet is shown in figure 30. An observer traveling with the sheet (and its mirror image) would observe the roll up as a function of time. Knowing his transport velocity ($V_\ell = d\ell/dt$) allows description of the roll up as a function of position along the "ℓ" axis.

$$\frac{da}{d\ell} = \frac{da/dt}{d\ell/dt}, \qquad \frac{db}{d\ell} = \frac{db/dt}{d\ell/dt}$$

$$\text{or} \quad \frac{da}{d\ell} = \frac{\gamma}{4\pi V_\ell} \ln\left(1 + \frac{c}{a}\right)$$

$$\text{and} \quad \frac{db}{d\ell} = \frac{1}{V_\ell}\left[W_s \sin(\lambda/2) - \frac{\Gamma}{4\pi(a+c)} \right]$$

Rains then assumes that fluid inside the roll up (of radius "a") rotates as a solid body, and that circulation of the solid body velocity field is equal to the circulation (Γ) of the rolled up vortex sheet. This allows the angular velocity to be computed as:

$$\omega_{TC} = \frac{\Gamma}{2\pi a^2}$$

A summation of the equations that are used to calculate tip clearance vortex radius and circulation is as follows:

$$\lambda = \cos^{-1}(W_p/W_s)$$

$$\gamma = 2 W_s \sin(\lambda/2)$$

$$V_\ell = W_s \cos(\lambda/2)$$

$$a = a' + \Delta\ell\left(\frac{\bar{\gamma}}{4\pi \bar{V}_\ell} \ln\left(1 + \frac{c}{a}\right)\right)$$

$$\Gamma = \frac{\Gamma' + \bar{\gamma} \tan(\bar{\lambda}/2)\,\Delta\ell\,(1-k)}{1 + \frac{\bar{\gamma}\,\Delta\ell\,(1-k)}{4\pi \bar{V}_\ell\,(a+c)}}$$

$$\omega_{TC} = \frac{\Gamma}{2\pi a^2}$$

The calculations are performed within the inducer internal flow analysis for each axial calculation station. Prime superscripts refer to previous station values and bars refer to a cumulative station average.

After determining the vortex properties, the velocities induced by the vortex are determined by a method similar to that recommended by Lakshminarayana (5). The vortex is assumed to be located in the center of the blade passage with the upper edge of the vortex core tangent to the blade tip as shown in figure 31. The passage is divided into two regions: inside and outside of the vortex core. At any radial location outside of the vortex core, the induced velocity is calculated by

$$W_{NC} = \frac{\Gamma}{2\tau}\left[\frac{\sinh M}{\cosh M - 1} - \frac{\sinh N}{\cosh N - 1}\right]$$

where $M = \frac{2\pi}{\tau} (R_T - R - a)$

$N = \frac{2\pi}{\tau} (R_T - R + a + 2C)$

τ = Passage width

This component of induced velocity is normal to the through flow relative velocity, W. The flow deviation, $\Delta\beta$, due to the induced velocity is

$$\Delta\beta = \text{Tan}^{-1} \left(\frac{W_{NC}}{W}\right)$$

Because the inducer internal flow analysis is based on one dimensional flow in the cross channel direction, a means for averaging the vortex effects on the flow field is used. Each stream tube is divided into portions which lie within the vortex core and those which are part of the induced flow field. The normal flow velocity is integrated over each region and area averaged for the streamtube according to:

$$\overline{W}_{NC} = \frac{\int_{AF} (W_{NC})_F \, dA_F + \int_{AI} (W_{NC})_I \, dA_I}{A_F + A_I}$$

where: A represents the cross channel area and the subscripts (F) and (I) represent the forced vortex and its induced flow field respectively.

The average effect of the vortex on the relative flow angle is then determined for each stream tube by:

$$\overline{\Delta\beta} = \text{Tan}^{-1} \frac{\overline{W_{NC}}}{W}$$

The average vortex effect calculations are repeated for each stream tube at each axial station. The change in the velocity component normal to the through flow direction is a function of the vortex strength and as such is based on the history of the formation of the vortex. That is, the flow conditions at any station which result from formation of the vortex are related to conditions from the leading edge to the point in question.

Preliminary evaluations of the basic vortex model resulted in predicted inducer deviation angles which were unrealistically large. Lakshiminarayana (5) also evaluated Rains' vortex model and concluded that predicted circulation was too large. He developed and applied a correction factor to the calculated circulation based on work he and Horlock had previously done (6) in which they measured the variation in lift of an isolated blade with tip clearance. Lakshminaryana's lift correction is shown as a function of clearance to blade tip spacing

(C/τ) in figure 32. His correction is the broken line and covers the range $0.01 < C/\tau < 0.10$. C/τ values for the inducer tests were 0.0015, 0.0028, and 0.0083; all lower than the range for which Lakshminarayana defined a lift correction. New corrections were calculated for these C/τ values in the same form as proposed in (5) with the value of the lift correction being determined from the experimentally measured inducer ideal head rise. These corrections and the lift correction curve fit in the clearance range $C/\tau < 0.01$ are shown as data points and a solid line in figure 32. The lift corrections which were defined from the inducer data are quite consistent with Lakshiminarayana's corrections.

3. Loss Model Formulation

The loss model used in the program was obtained from the work of Lakshminarayana (5). The model includes the parameters; clearance to blade height ratio ($C/\Delta\bar{R}$), average blade tip metal angle ($\bar{\beta}_T^*$), Aspect Ratio (AR), inlet tip flow coefficient (ϕ) and ideal head coefficient (ψ_{iTC}). Lakshiminarayana's expression for the efficiency differential due to tip clearance is:

$$\Delta\eta = \frac{0.7\ (C/\Delta\bar{R})}{\sin\bar{\beta}^*_{TIP}}\ \psi_{iTC}\left[\ 1 + 10\sqrt{\frac{\bar{\phi}}{\psi_{iTC}}\ \frac{(C/\Delta\bar{R}\cdot AR}{\sin\bar{\beta}^*_{TIP}}}\ \right]$$

Tip clearance loss is applied to inducer total mass averaged performance at the inducer exit. The performance at this point includes the effect of tip clearance on ideal head rise by virtue of the vortex formation but the effect of tip clearance on actual head (or loss) is not included.

The mass averaged head loss is modified to include the effects of tip clearance through the use of Lakshminarayana's efficiency relationship:

$$\psi_{\ell TC} = \left[\ 1 - \eta' + 0.7\ \frac{(C/\Delta\bar{R})}{\sin\bar{\beta}^*_{TIP}}\ \psi_{iTC}\left(1 + 10\sqrt{\frac{\phi}{\psi_{iTC}}\ \frac{(c/\Delta\bar{R})\cdot AR}{\sin\bar{\beta}^*_{TIP}}}\right)\right]\psi_{iTC}$$

where:

η' = Efficiency without tip clearance effects.

After calculation of the total loss coefficient, including the effect of tip clearance, actual head rise and overall efficiency are calculated as follows:

$$\psi_{a\ TC} = \psi_{iTC} - \psi_{TC}$$

$$\eta_{TC} = \frac{\psi_{aTC}}{\psi_{iTC}}$$

where the subscript (TC) represents parameters that include the effects of tip clearance.

C. Leading Edge Sweepback Analysis

Leading edge sweepback was provided for in the original hydrodynamic analysis of (1). The computer program accepts a description of the leading edge shape in the meridional plane as a third order polynominal in R with constant coefficients. The value of the coefficients is input. A radial leading edge is defined by setting the coefficients equal to zero. The flow analysis of the swept and unswept leading edge cases is the same and the effects of sweepback are accounted for by assuming that the angular momentun of an element of fluid in a streamtube does not change until the element enters the inducer. Corrections for blade thickness and boundary layer blockage are made whenever a streamtube enters the blade passage.

Flow analysis of inducers with leading edge sweepback was complicated by difficulties in some cases in obtaining computer program convergence. An iteration is included in the program to insure that the radial pressure gradient that results from the calculated streamtube properties satisfies the gradient obtained from radial momentum. The iteration converges relatively quickly for noncavitating cases, but the existence of a vapor cavity on the blade surface often prevents convergence within 100 iterations (the internal program limit). Inspection of the pressure gradient values in these instances reveals that no progress toward convergence is being made. In spite of the lack of convergence on pressure gradient the predicted pressure profiles generally appear to be smooth and reasonable except in certain cases where highly swept inducers are being analyzed. In these cases, results were obviously erroneous with negative streamtube static pressures being predicted.

Several modifications to the computer program were made in an attempt to improve the iteration:

1) A limit on cavity size changes between iterations was added.

2) The amount of streamline adjustment between iterations was increased.

3) Streamline curvature and radial acceleration effects were removed from the radial momentum equation.

These modifications did not significantly improve the convergence, and the original calculations were retained.

A finer axial grid spacing (Z = 0, .002, etc. instead of 0, .005, etc) was then input into the program, and one of the obviously erroneous cases was rerun. Predicted pressures were considerably improved, and the radial pressure profile was smooth and reasonable. Vapor cavity length was also in good agreement with the test data. Convergence on pressure gradient was closer than previously but the error is still of considerable magnitude. A comparison of the predicted pressure profile from the streamtube calculations, the pressure due to radial momentum, and the measured pressures is shown in figure 33 for an axial station .14 ft. (.042 m) inside the leading edge. The measured pressures are between the predicted streamtube pressures and the radial momentum

pressures. If the pressure gradient convergence iteration had operated properly, the predicted and measured radial pressure profiles would be expected to be in good agreement. The finer grid spacing was found to generally improve the pressure gradient convergence for all axial stations similar to the results of figure 33.

The general agreement of predicted with measured blade loading and performance data (as will be discussed in Section V), in spite of the lack of pressure gradient convergence, indicates that these predictions were not particularly sensitive to radial pressure gradient and therefore a close tolerance convergence was not absolutely required for the purpose of this program. Undoubtedly, the computer program would be more generally applicable and its predictions would be more accurate if the pressure gradient iteration converged. Future effort might be fruitfully expended to improve the convergence.

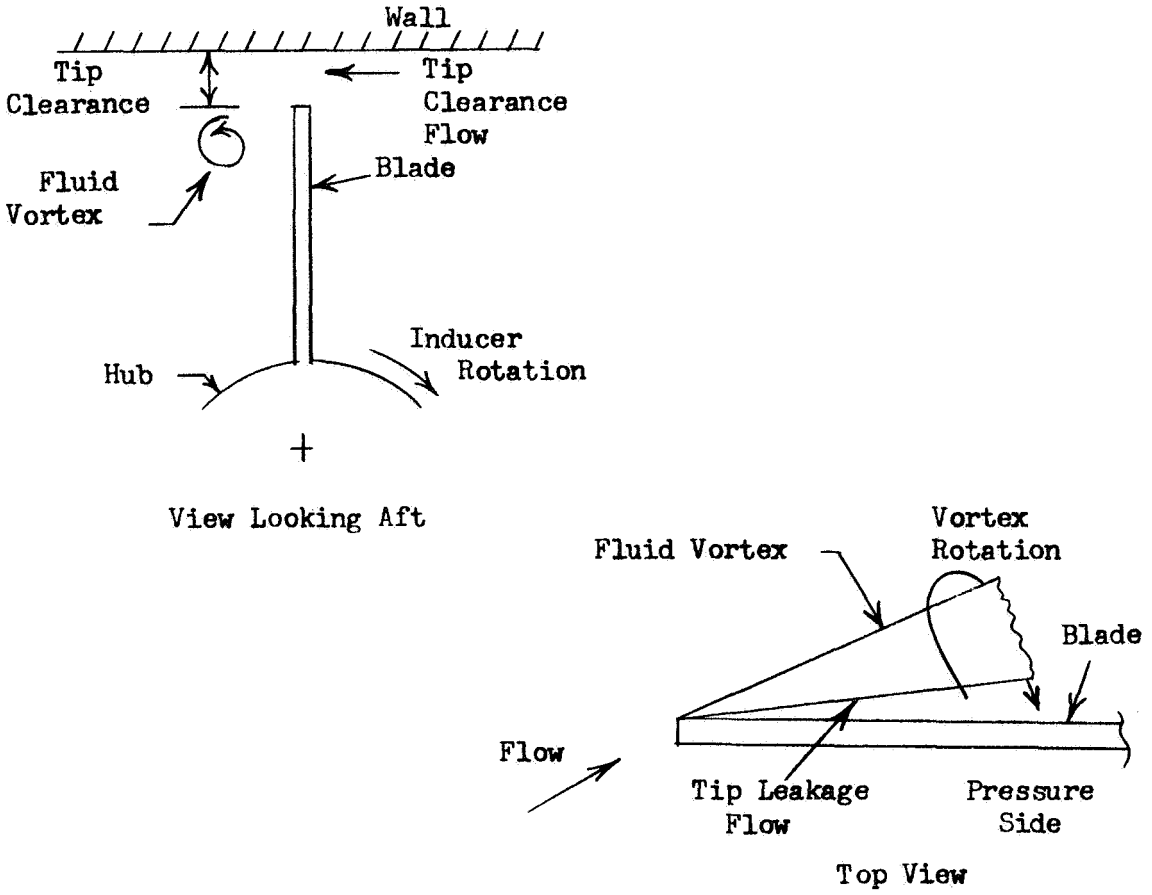

Figure 26. Tip Vortex Flow Model FD 63322

$$\lambda = \cos^{-1}\left(\frac{W_p}{W_s}\right)$$

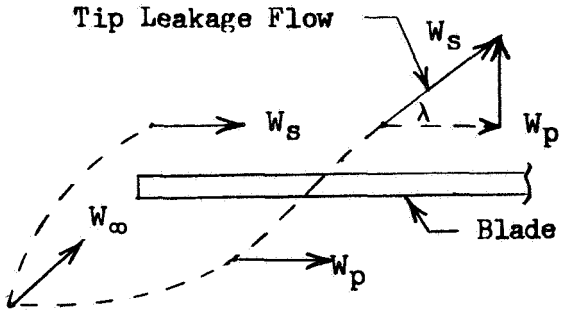

Figure 27. Flow Velocities in the Tip Clearance Region FD 63323

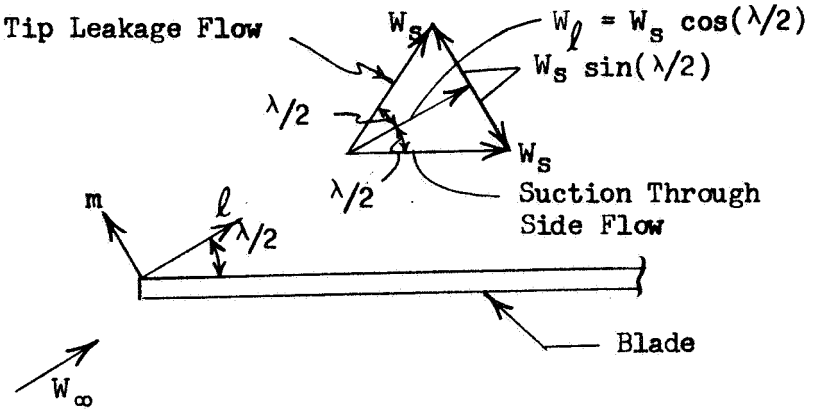

Figure 28. Interaction of Tip Clearance With Through Flow FD 63324

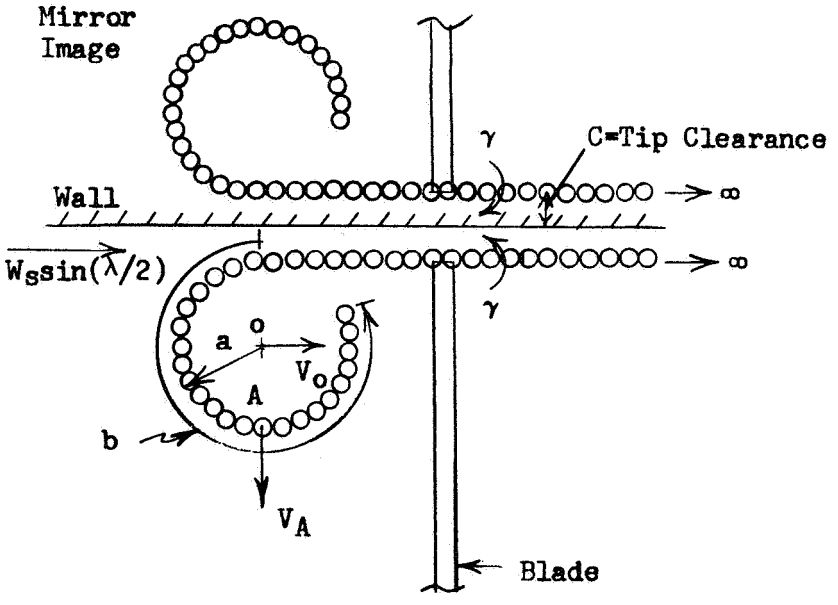

Figure 29. View Looking Aft in "ℓ" Direction FD 63325

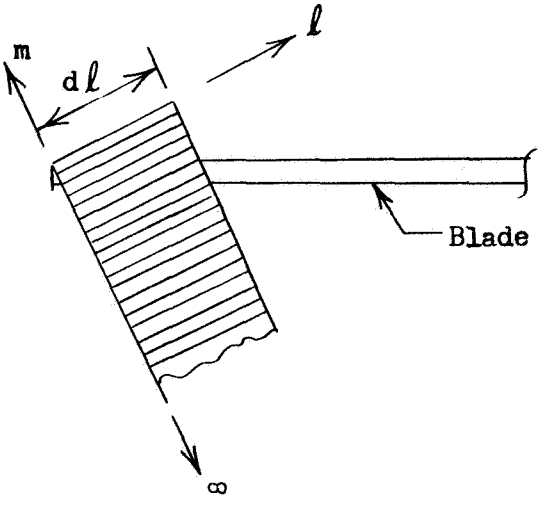

Figure 30. Top View FD 63326

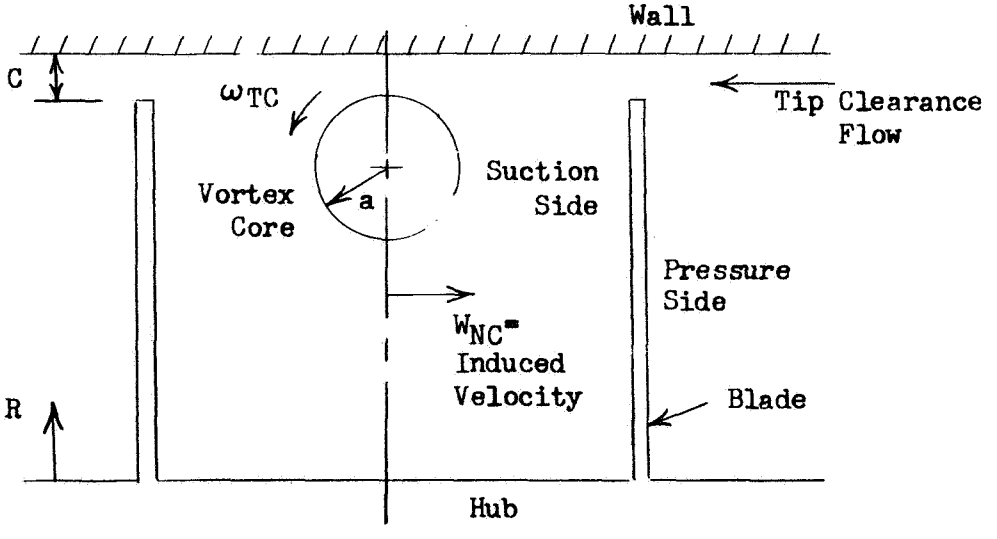

Figure 31. Vortex Located in Blade Passage FD 63327

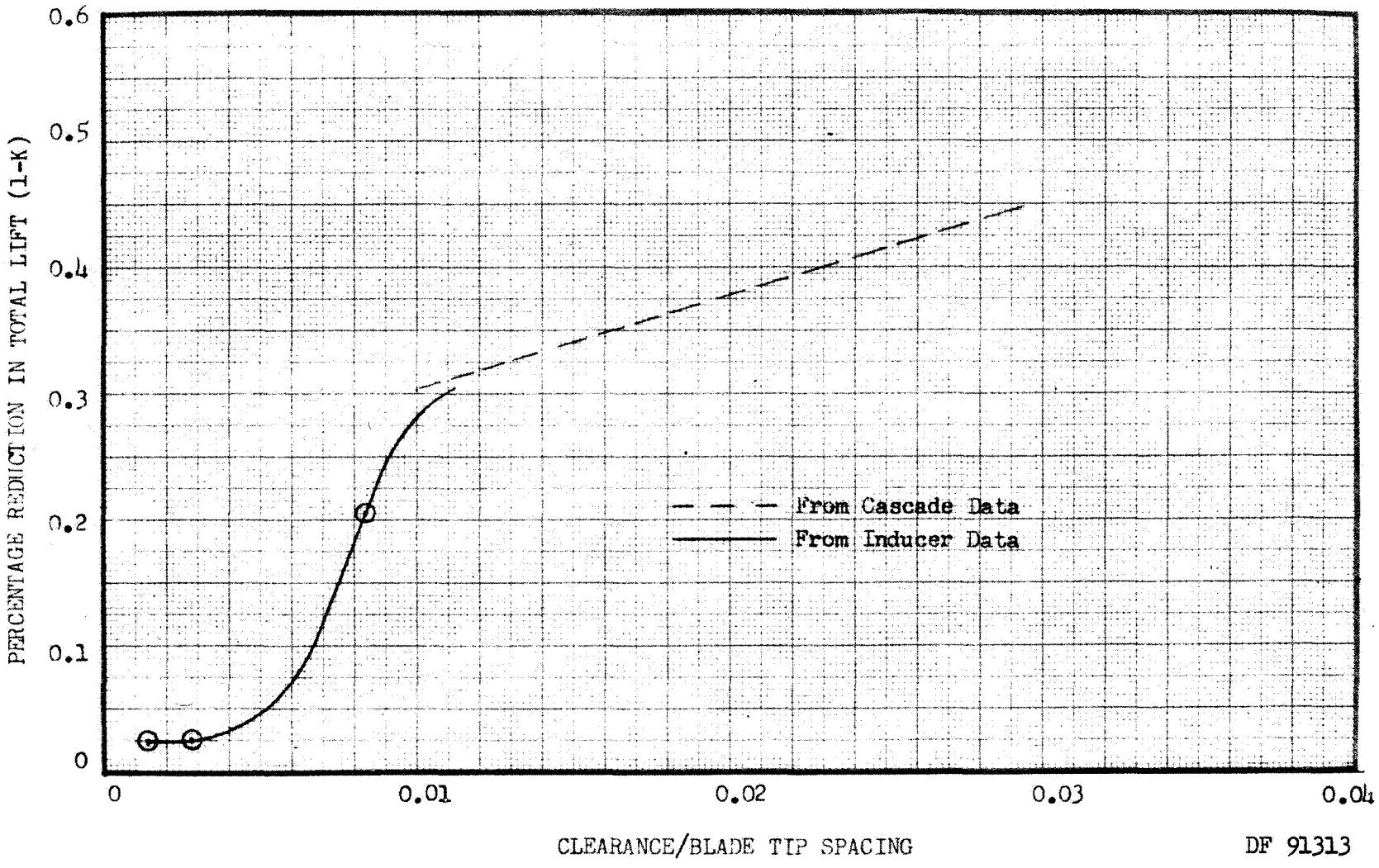

Figure 32. Variation in Blade Lift with Tip Clearance

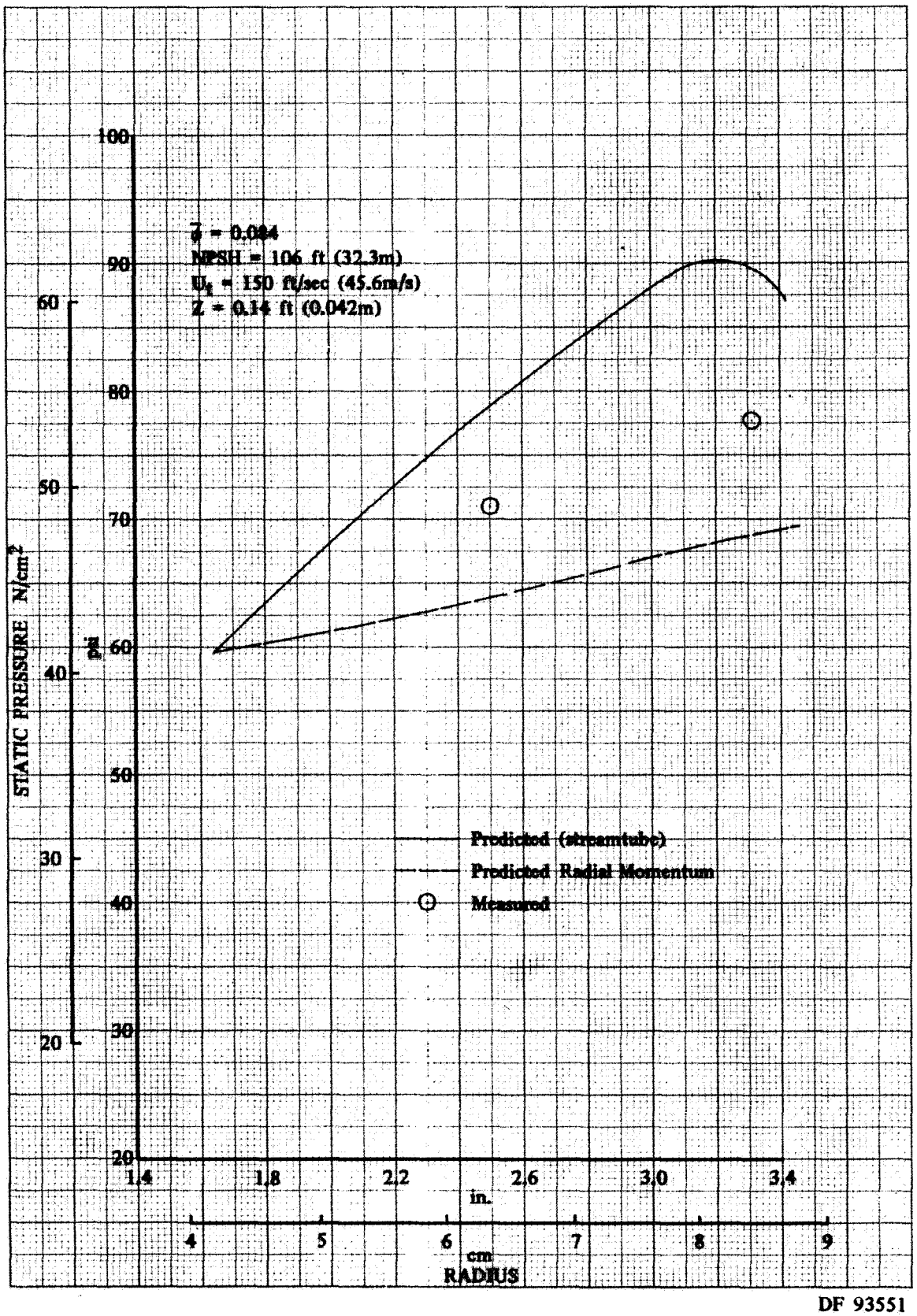

Figure 33. Comparison of Predicted with Measured Radial Static Pressures, Radial Leading Edge Inducer.

SECTION V
DATA CORRELATION

A. Tip Clearance

The predicted effect of blade tip clearance on inducer head coefficient and efficiency is compared with experimental data in figure 34. Predicted and experimental ideal head coefficient and head loss coefficient are compared in figure 35. Actual head and efficiency predictions are in general agreement with the experimental data. Discrepancies in the level of efficiency and actual head rise are evident as well as some descrepancy in the trend of these parameters with clearance to blade height ratio.

The experimental data indicates an optimum clearance other than zero for which the inducer will achieve maximum performance. This phenomena was discussed by Lakshminarayana in (5). His conclusion was that the vorticity set up by the tip leakage flow through formation of the tip vortex opposes the passage vorticity which arises from secondary flows resulting from flow turning and passage rotation. When each of these effects cancel, that is the net secondary passage vorticity becomes zero, maximum performance will result. The hydrodynamic program does not include secondary vorticity and as such should not be expected to predict the optimum clearance observed from the experimental data.

Predicted and measured ideal head rise are in near exact agreement in both magnitude and trend with varying tip clearance. The difference between predicted and measured overall efficiency and actual head rise therefore results from an inability to accurately predict head loss. The loss predicted at 0.096 flow coefficient is in better agreement with the measured data than that predicted at 0.084 flow coefficient. Since the ideal head is predicted correctly for both one would expect better overall performance agreement at the higher inlet flow coefficient. This is shown to be true on figure 34.

Predicted and measured loss and ideal head vs. flow coefficient data are compared in figure 36. Although a significant variation in loss with flow coefficient was predicted, the measured data shows no variation. This was true for all clearances at which the inducer was tested. The discrepancy between the predicted and measured loss is probably caused by the greater sensitivity of predicted cavity size (and associated dump loss) to changes in inlet flow coefficient than that observed from the experimental data. "Non cavitating" blade loading predictions indicated cavities which were longer than the measured data and the error magnitude increased as flow coefficient decreased. This correlation is discussed in section B1c. Figure 37 shows the total predicted loss broken into its component losses: boundary layer, cavity dump and tip clearance. The cavity dump loss decreases vary rapidly with increasing flow coefficient and adjustments in it could bring predicted lossed into agreement with measured data.

This greater sensitivity of the predicted cavity size to variations in inlet flow coefficient could result from a cavity model inacurracy or from inadequate description of the radial distribution of inlet flow

conditions. As was illustrated in (1), figures 75 and 76, and in figure 15 the most radially uniform inlet flow conditions occurred at 0.096 inlet flow coefficient. As flow coefficient was decreased, prerotation increased and tip axial velocity decreased to the point of tip backflow. Two problems result from this inlet flow distortion relative to the prediction of inducer performance. These are: (1) The inlet flow profile must be defined and there is currently no way of predicting the profile for a new design and (2) The hydrodynamic computer program does not converge consistently on a solution for highly distorted inlet flow profiles. Neither of these problems appear solvable within the scope of the current contract.

B. Leading Edge Sweep

1. Blade Pressure Loading

Predicted and measured blade pressure loading plots, for the tests where purge seal leakage was not excessive, are shown in figures 38 through 43 for the 8 deg (.14 rad) and in figure 44 through 47 for the 16 deg (.28 rad) leading edge tests. The predicted plots show a stagnation point near the leading edge at which the static pressure is equal to the relative total pressure. Only those measured pressure points which were well below the measurement limit, as established by available purge pressure, are shown. This limit is marked in the plots. Most data were limited to the suction surface, and the first data point to reach the measurement limit is marked with an arrow to indicate that the actual pressure is equal to or higher than the plotted value. Noncavitating data are shown in figures 38 and 39 for the 8 degree inducer tip streamline at 80% and 100% operating speed. Cavitating tip streamline data are shown for different flow coefficients in figures 40, 41 and 42 and midspan streamline data are shown in figure 43. Noncavitating data for the 16 degree inducer tip streamline are shown in figure 44. Cavitating data for the tip streamline at two flow coefficients are shown in figures 45 and 46 and data are shown for the midspan streamline at several flow coefficients in figure 47. Selected figures can be compared to obtain an indication of the effects of rotor speed, flow coefficient, radius, and NPSH on the pressure distributions.

a. Rotor Speed Effects

A trend of increased cavity length at higher rotor speed was reported for the radial leading edge inducer in (1). This would be expected since fluid relative velocity is increased at constant pressure for increased rotor speed. Both the measured and predicted radial inducer data showed this trend for "noncavitating" operation at flow coefficients of 0.096, 0.090, and 0.084. The effects of rotor speed for the 8 deg (.14 rad) inducer is seen by comparison of plots for flow coefficients of .090 and .070 in figures 38 and 39. It should be noted that pressure data in the area of a vapor cavity is not properly normalized by the static head coefficient because fluid vapor pressure remains constant while other pressures change with the square of speed. Although the measured data is limited, it can be interpreted to agree with the results of the radial leading edge inducer, a slight increase in cavity length with increased rotor speed. Predicted data for $\bar{\phi}$ = .090 in the figures also show

the expected increase in cavity length with speed but predictions for the $\bar{\phi}$ = .070 point do not. The reason for the discrepancy in the $\bar{\phi}$ = .070 predictions may be due to the previously mentioned computer program convergence problem.

b. Radius Effects

The effect of radial location can be seen by comparing the $\bar{\phi}$ = .090 NPSH = 37.9 plot of figure 41 with the ϕ = .090, NPSH = 39.1 plot of figure 43. Except for the region near the leading edge where a cavity exists, the predictions show a slightly higher head coefficient for both the suction and pressure surfaces for the outer radius. Because of centrifugal effects the static pressure would be expected to be higher in the tip region. This would result in higher head coefficients. The test data and predictions indicate that a longer vapor cavity forms on the blade at the outer radius. This result can be explained by considering the effective incidence and flow angle at the midspan and outer radii. The incidence decreases at the outer radius and tends to result in a smaller cavity. The flow angle is decreasing also which tends to cause a longer cavity. The net result of these two effects is to give longer cavities at the outer radius.

c. Flow Coefficient Effect

For approximately the same levels of NPSH and the same values of rotor speed and radial location, the effect of flow coefficient for the 8 deg (.14 rad) inducer at constant NPSH can be determined from the following series of figures:

NPSH	106 ft (32.3 m)	Figures 38 and 39
NPSH	60 ft (18.3 m)	Figures 40, 41 and 42
NPSH	36 ft (11.0 m)	Figures 40, 41 and 42
NPSH	17 ft (5.2 m)	Figures 40, 41 and 42

The predicted data show the expected increase in cavity length as flow coefficient decreases (due to the increase in cavity length with increasing incidence and increasing incidence with decreasing flow coefficient). The predicted and measured data for the radial leading edge inducer from (1) show this same trend. The measured data on these figures, however, show much less change in cavity length with inlet flow coefficient than the predicted. The differences between predicted and measured data may be partly due to prerotation effects which were not accounted for in the predictions.

For the 16 deg (.28 rad) sweptback inducer the following series of comparisons will illustrate the effects of flow coefficient:

NPSH	106 ft (32.3 m)	Figure 44
NPSH	60 ft (18.3 m)	Figures 45 and 46
NPSH	36 ft (11.0 m)	Figures 45 and 46
NPSH	12 ft (3.7 m)	Figure 47

The conclusion from these comparisons is similar to that for the radial and 8 deg sweepback cases. That is, a decrease in flow coefficient results in an increase in predicted cavity length, especially at low levels of NPSH, and a smaller than predicted increase in measured cavity length.

d. NPSH Effects

The effect of NPSH (or inlet total pressure) for the 8 deg (.14 rad) inducer can be seen by making a series of comparisons similar to the ones for flow coefficient. At the outer radius and a rotor tip speed of 150 ft/sec (45.6 m/s) figures 40, 41 and 42 show the effect of decreasing NPSH at constant flow coefficients of .094, .090, and .084.

These comparisons show that both the measured and predicted data indicate increasing cavity length with decreasing NPSH. This result was reported for a radial leading edge inducer in (1) and is the expected trend since the lower inlet pressure results in a lower mean pressure within the inducer. All pressures tend to be reduced in direct proportion to the inlet pressures with the fluid vapor pressure as a lower limit. The result of decreasing NPSH is therefore a longer cavity and a relatively constant blade pressure loading over the region covered by the cavity. The blade loading is redistributed so that the leading edge load is reduced but relatively high loadings extend further into the inducer.

Of all the data taken, only one flow point had pressure measurements that were good outside of the cavity region. This data, which is for a flow coefficient of .096 and an NPSH of 105.6 ft (32.3 m), is shown on figure 38. Although the predicted difference in blade surface pressures agree with the experimental data, the predicted absolute pressure levels for both suction and pressure surfaces are greater than measured.

Since the remainder of the data taken for the other flow points was only accurate in the region of the vapor cavity it is not possible to estimate the agreement between measured and predicted loadings. The lack of data also prevents an indication of how the suction side pressures recover after the cavity collapses. It should be noted, however, that the agreement between predicted and measured cavity length is reasonable. The data comparisons show the expected trends when considering the effects of flow coefficient and NPSH, which indicates that the program modifications made to account for sweepback are adequate for an 8 deg sweepback.

The influence of decreasing NPSH on blade loading at 16 deg (.78 rad) sweepback can be seen in figure 45 for a flow coefficient of .090 and in figure 46 for a flow coefficient of .084. These comparisons show the expected trend of increasing cavity length with decreasing NPSH that was noted in the radial leading edge and 8 deg sweepback cases. The predictions show good agreement with the data. The reduction of leading edge loading and extension of the region of high loading further into the inducer passage with decreasing NPSH is noted again as it was for the radial leading edge and 8 deg sweepback cases.

e. Sweepback Effects

By considering the 8 and 16 deg sweepback predicted and measured data separately, it has been concluded that the inducer program generates cavity length predictions that are in reasonable agreement with the test data. The effects of sweepback as observed experimentally and as predicted by the inducer program can be evaluated from the following comparisons of 8 with 16 deg data:

Figure 39 with 44 at an NPSH of 106 ft (32.3 m) and $\overline{\phi}$ = .070
Figure 41 with 45 at an NPSH of 60 ft (18.3 m) and $\overline{\phi}$ = .090
Figure 42 with 46 at an NPSH of 60 ft (18.3 m) and $\overline{\phi}$ = .084
Figure 41 with 45 at an NPSH of 37 ft (11.3 m) and $\overline{\phi}$ = .090

A comparison of the two sets of sweepback data with radial data could not be made since there were no measured data for corresponding operating points (equal NPSH, flow coefficient, rotor speed, and radial location) for the three cases. In general, the predicted difference between the 8 deg and 16 deg sweepback pressures was small with the exception of .070 flow coefficient point which showed a considerable difference.

A plot of predicted and measured axial cavity length as a function of cavitation number for the tip streamline is shown in figure 48. Axial cavity lengths were taken as the distance from the leading edge to the point of cavity collapse from the plots of figures 38 through 47. Since the measured collapse point cannot be precisely defined, the deepest (within the inducer) suction surface pressure tap to measure vapor pressure and the first to measure a pressure above vapor pressure are shown on figure 48. It can be assumed that the cavity collapsed between these pressure taps. The predicted cavity lengths for the radial inducer are not shown because they were generated with a earlier cavity model for the report of (1). The cavity model has since been refined as reported in (3) and the refined version was used to generate predictions for the 8 and 16 deg (.14 and .28 rad) swept inducers. Predicted data were initially generated with a coarse grid breakup (24 axial stations and 7 streamtubes) for the 8 deg (.14 rad) inducer and a fine grid breakup (48 axial stations and 11 streamtubes) for the 16 deg (.28 rad) inducer. In some cases, the fine grid was necessary for the 16 deg. inducer to obtain program convergence as discussed in Section IV-C. Grid spacing was later found to effect cavity length, as will be discussed in subsequent paragraphs, and a high and low NPSH point for the 8 deg. inducer were reanalyzed with a fine grid spacing. The fine spacing would be expected to yield more accurate predictions. The fine spacing did not appreciably change the predicted cavity length at high NPSH but it caused the predicted length to increase at low NPSH. The original coarse grid cavity length predictions for the 8 deg inducer were therefore adjusted in accord with the more accurate two fine grid predicted points. This adjusted curve is shown in figure 48 and can be compared with the fine grid 16 deg inducer curve.

The predicted 8 and 16 deg cavity length curves show little effect of sweepback on cavity length. The predicted lines are relatively close

at high and moderate values of NPSH, then tend to diverge at a cavitation number of approximately .08. Below .08, the 16 deg cavity lengths are shorter than the 8 deg. Measured data are not sufficiently complete to conclusively define the effect of sweep on cavity length but they also indicate that there is little effect at cavitation numbers down to approximately 0.1. Below 0.1, the 16 deg sweep cavity lengths appear to be shorter than the 8 deg and radial inducer data. At these low cavitation numbers, the measured effect of sweep on cavity length is greater than the predicted effect.

All of the predicted results have been generated with the assumption of no inlet prewhirl. However, radial traverses of the inducer inlet indicate that non-constant distributions of flow angle, axial velocity, and total head are present. Since inlet variations can be input to the computer program (backflow conditions expected), an attempt was made to define the influence of prewhirl on the predicted data. A typical distribution (based on traverse data) of inlet parameters was used for predictions of blade loadings for both radial and 16 deg sweepbacks. The agreement between test data and the predictions with prewhirl was not as good as previously. For this reason, all of the predictions were generated for constant inlet conditions.

As previously mentioned, the predictions were found to be somewhat sensitive to the input grid pattern (number of streamlines and number of axial stations). A comparison of predicted and measured data, where the predictions were generated with both a coarse and a fine grid, is shown in figure 49 for the radial, 50 for 8 deg (.14 rad) and 51 for the 16 deg (.28 rad) inducers. Each figure shows the data for both a coarse and a fine grid at a high and a low NPSH operating point. Coarse and fine grid patterns are defined as follows:

	No. of Streamlines	No. of Axial Stations	Axial Station Spacing at Inlet
	NI	NJ	Z
Coarse	7	25	.005 ft (.0015 m)
Fine	11	48	.002 ft (.0006 m)

High and moderate NPSH predictions were not sensitive to grid pattern but the low NPSH predictions with the fine grid are in better agreement with the measured data.

There are several areas in which more work could result in improved data correlation. An accurate definition of the influences of prewhirl and the sweepback-prewhirl interaction would help to remove one of the biggest unknowns in this study. Also, there are two areas of possible improvement of the inducer hydrodynamic computer program. The first of these is in the basic cavity model. The total cavity is made up of two primary parts. The first is the growth to maximum conditions, and the second is the cavity collapse. Each of these parts are not as well refined as possible. In determining the cavity growth the program has the tendency of predicting the distance to maximum height too long,

especially for low flow coefficients. The cavity collapse model is only approximate, based on limited empirical data, and could be improved if more data were available. The details of the work done on the cavity model are given in (3). Both of these affect the cavity length so that the blade loading predictions could be improved by solving these problems. The second program weakness lies in its method of determining the radial pressure gradient. Since this procedure affects all of the static pressures in the flow field, an improvement in this area would be significant. The method of calculating the radial pressures involves an iterative procedure that does not converge for many cases.

In spite of all of these problem areas, it is concluded that the comparison of predicted and measured loadings is reasonably accurate for each of the 8 deg and 16 deg sweptback inducers.

2. Performance

a. Noncavitating

For noncavitating conditions, the two independent head coefficients that describe the performance are ideal head, ψ_i, and head loss, ψ_ℓ. Ideal head is a measure of the amount of head that could be generated by the inducer without losses, and the head loss is a measure of the inducer internal losses resulting from cavitation and viscous effects. Actual head coefficient, ψ_a, and efficiency, η, are related to the ideal head and head loss by

$$\psi_a = \psi_i - \psi_\ell$$

$$\eta = 1 - \psi_\ell / \psi_i$$

Figure 52 compares the predicted variation of ideal head and head loss with flow coefficient to the measured data for the three sweepback configurations, and Figure 53 shows the same comparison for actual head and efficiency. The agreement in ideal head is relatively good, while the predicted head loss trend does not match the test data. Since the actual head and efficiency are defined in terms of ideal head and head loss, the lack of agreement in predicted vs. measured head loss is reflected in the actual head and efficiency comparisons. To better indicate the effects of sweepback on performance, the comparisons of Figures 52 and 53 have been replotted, vs. sweepback angle in Figures 54 and 55, respectively.

When the leading edge of an inducer blade is swept back, the blade length and solidity decrease. Since the exit deviation is a function of the solidity (see (1)) and the ideal head is dependent upon the exit deviation, sweepback changes the ideal head. However, over the range of solidities of the test inducers (2.9 for the radial leading edge to 2.4 for the 16° (.28 rad) sweep) the effect on deviation is small, with the estimated loss in ideal head being 0.2% for an 8° sweepback, and 0.4% for a sweepback of 16°. As shown in Figure 54, the measured variation of ideal head with sweepback was small for all flow coefficients except .070 and the agreement between predicted and measured ideal head is good except at the .070 flow coefficient.

The predictions of head loss in Figure 54 indicate that the head loss increases with sweepback while the data shows a bucket characteristic (decreasing head loss to a minimum value and then increasing) with the net result being a decrease of head loss from the radial configuration.

Part of the lack of agreement between the predictions and data may be due to the inlet prewhirl and prewhirl-sweepback interaction. All of the predictions of performance were generated with the assumption of no inlet prewhirl so that some lack of agreement would result from the fact that the data was measured with inlet prewhirl. A better determination of the effects of prewhirl will allow a more complete assessment of the agreement between measured and predicted performance.

In Figure 55 the level of the actual head predictions agree fairly well with the data, but they do not show the same trend with sweepback as the data shows. The discrepancy between measured and predicted actual head is dependent on flow coefficient and becomes greater as flow coefficient decreases. Since the actual head and efficiency are dependent on both the ideal head and head loss, the variation of head loss with sweepback is reflected in the curves of Figure 55.

When the blade loading investigation was being made, the computer program input grid (number of streamlines and numbers of axial stations) was revised in an attempt to solve problems that developed when the 16^{o} sweepback case was being run. Since it was shown that the fine grid would tend to improve the agreement between predicted and measured loadings, the influence of the fine grid on performance was evaluated. Figure 56 compares the predicted performance for a fine and normal grid with the test data at a flow coefficient of 0.084. The ideal head is increased by the fine grid, and the shape of the head loss curve agrees better with the data. Since the data includes the effect of prewhirl and the predictions do not, this may explain the difference between the measured and the revised prediction of ideal head. The revised head loss prediction is approaching the bucket characteristic of the data, and the agreement with data is much better than with the normal grid. A better definition of the cavity growth and of the remainder of the flow field is the best explanation for the improvement in the head loss prediction with a fine grid.

b. Cavitating

The cavitating performance of an inducer is usually evaluated by determining the point at which head break down occurs as NPSH is lowered at a constant flow coefficient. Figure 57 shows the head fall off curves for the radial and swept leading edge inducers. The experimental data indicates that increasing the leading edge sweepback lowers the NPSH at which the head falls off. This trend is duplicated by the predictions although the sharp fall off of the data is not obtained. Both the data and predictions show that the cavitating performance of an inducer can be improved (suction specific speed increased) by sweeping back the leading edge.

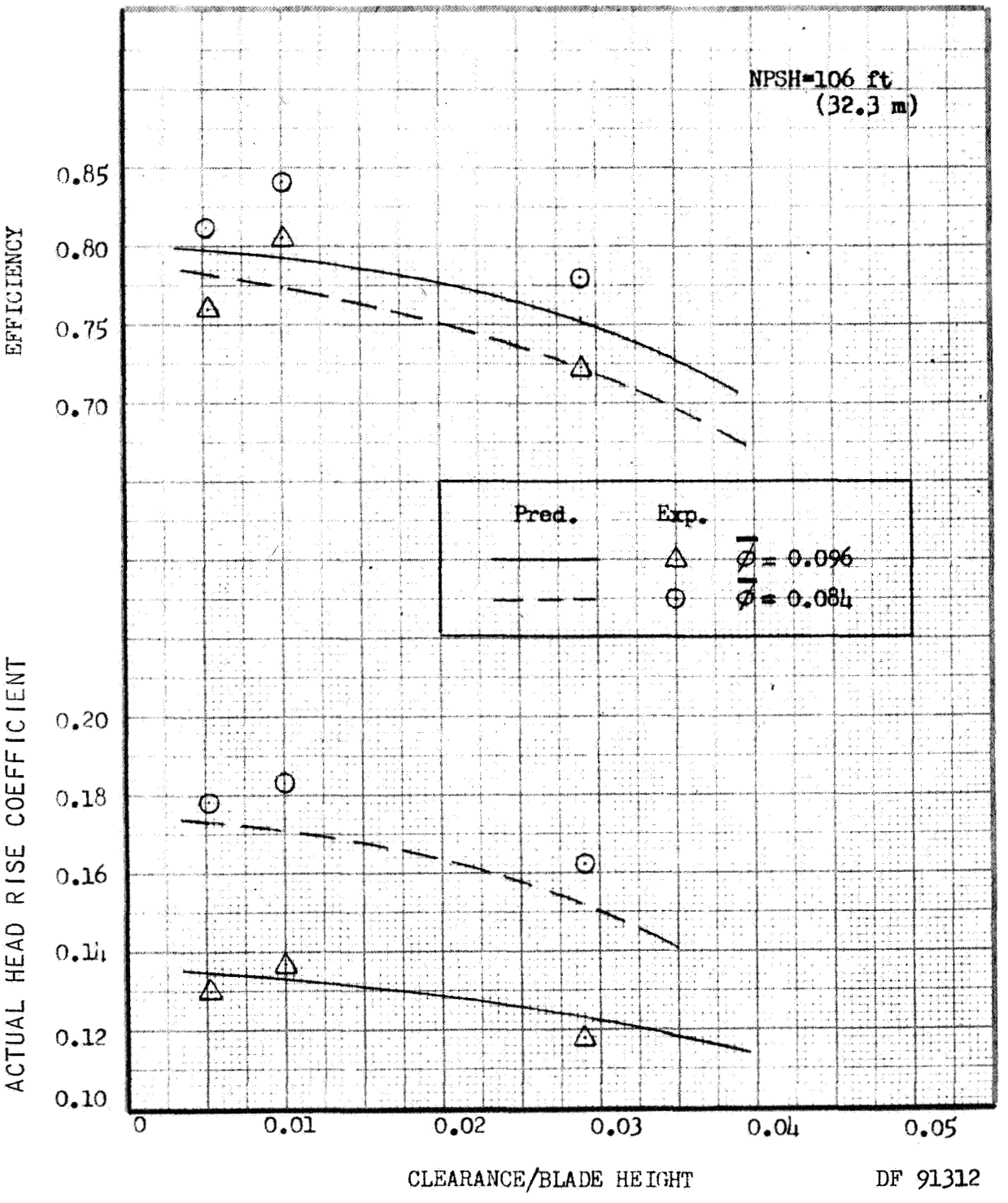

Figure 34. A Comparison of the Predicted and Experimental Effects of Blade Tip Clearance on Inducer Head Coefficient and Efficiency

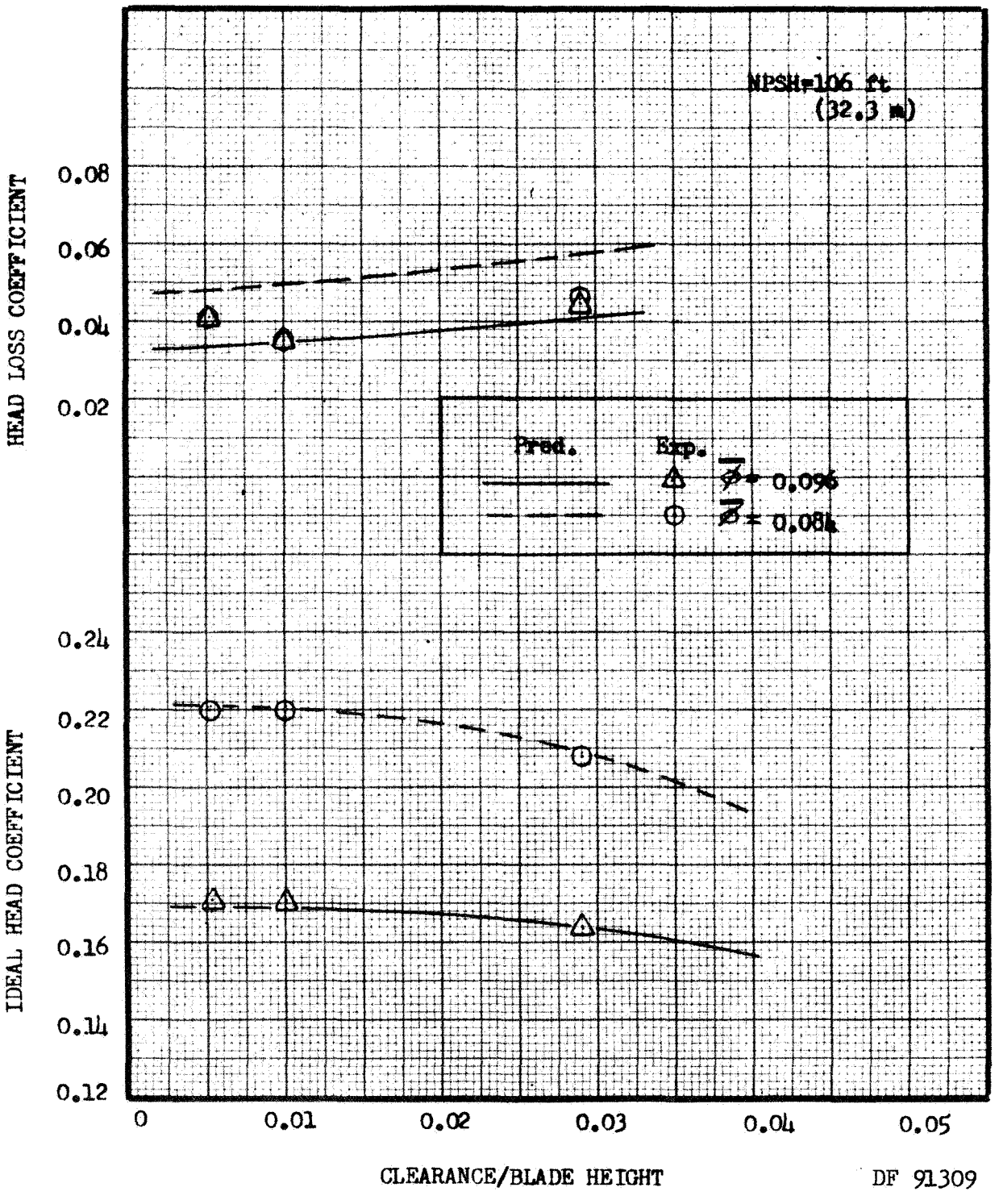

Figure 35. A Comparison of the Predicted and Experimental Effects of Blade Tip Clearance on Inducer Ideal Head Coefficient and Head Loss Coefficient

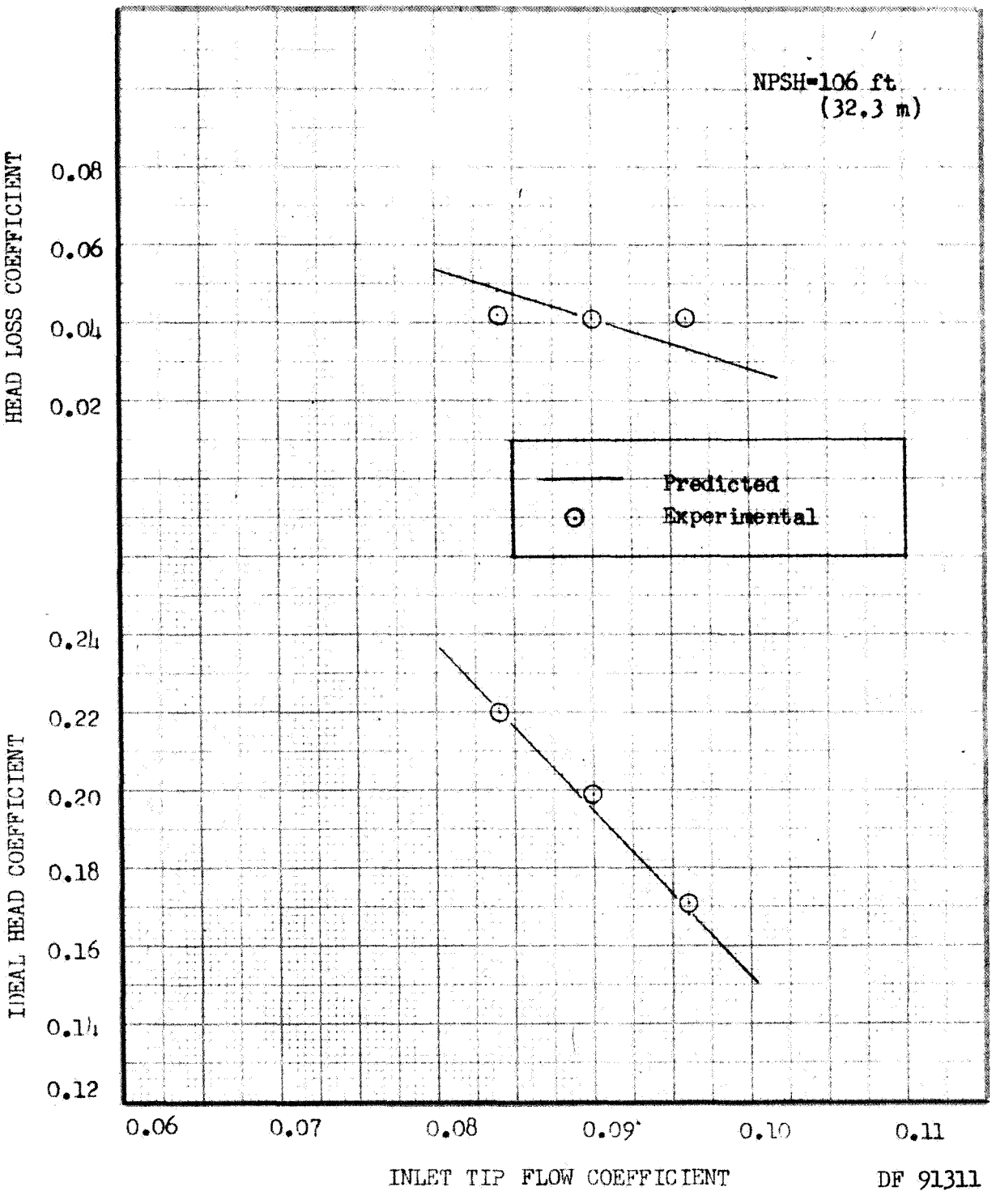

Figure 36. A Comparison of the Predicted and Experimental Effects of Flow Coefficient on Inducer Ideal Head Coefficient and Head Loss Coefficient. C = .011 in (0.028 cm)

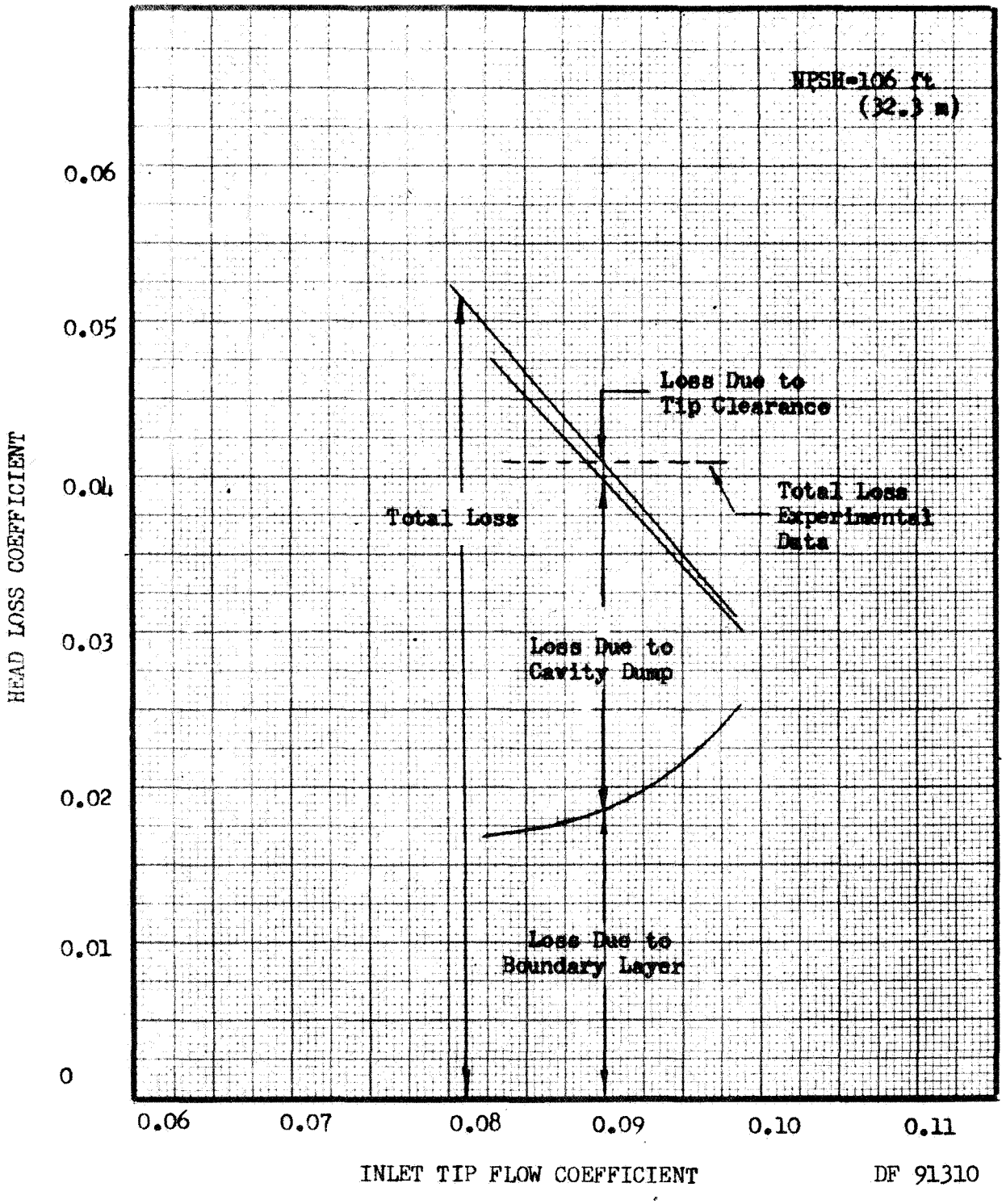

Figure 37. Loss Components of Inducer Total Predicted Loss. C = .011 in (0.028 cm)

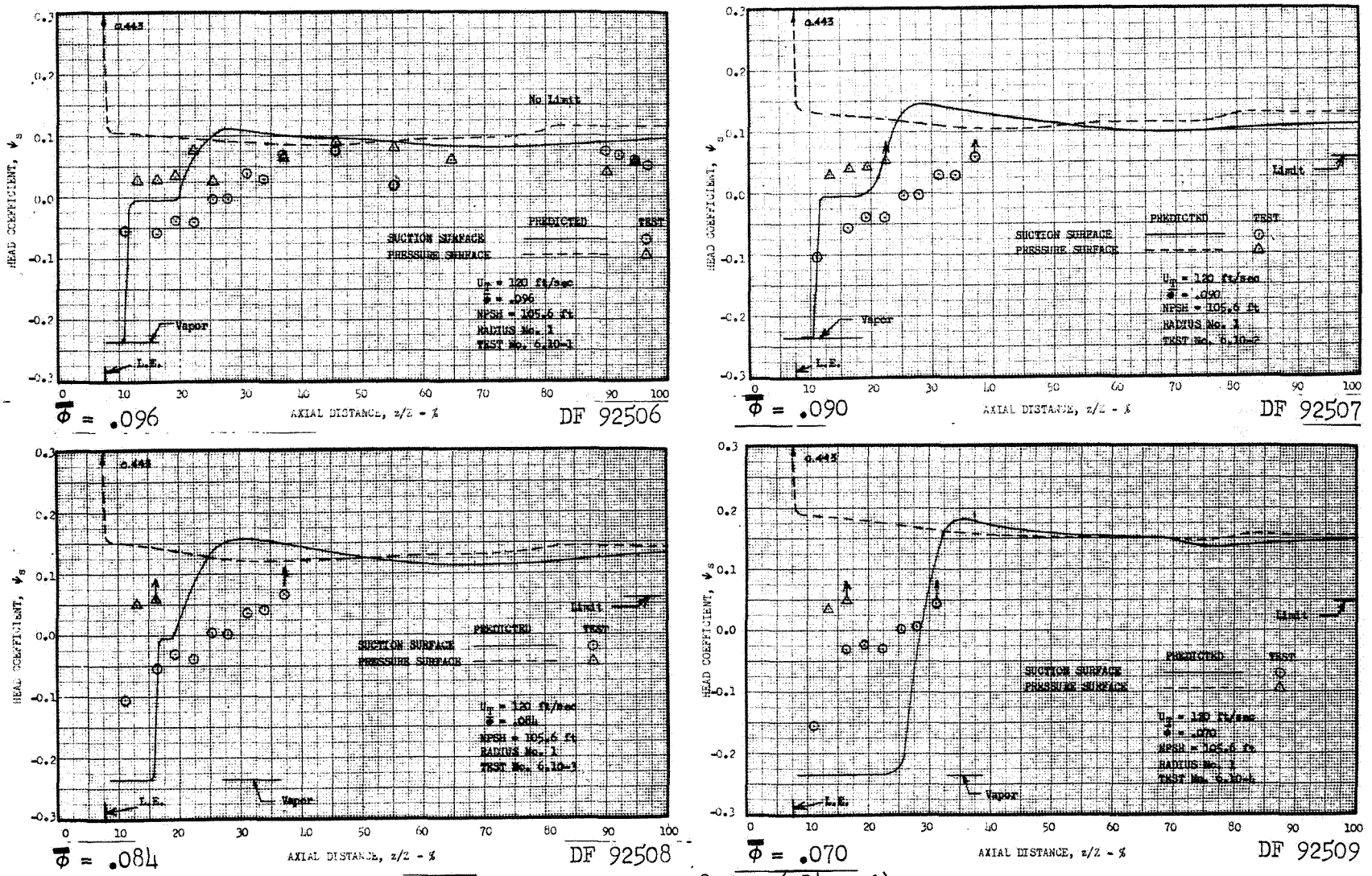

Figure 38. Noncavitating Blade Pressure Distribution; 8 deg (.14 rad) sweepback, Tip Streamline, U_T = 120 ft/sec (36.4 m/s), NPSH = 106 ft. (32.3 m).

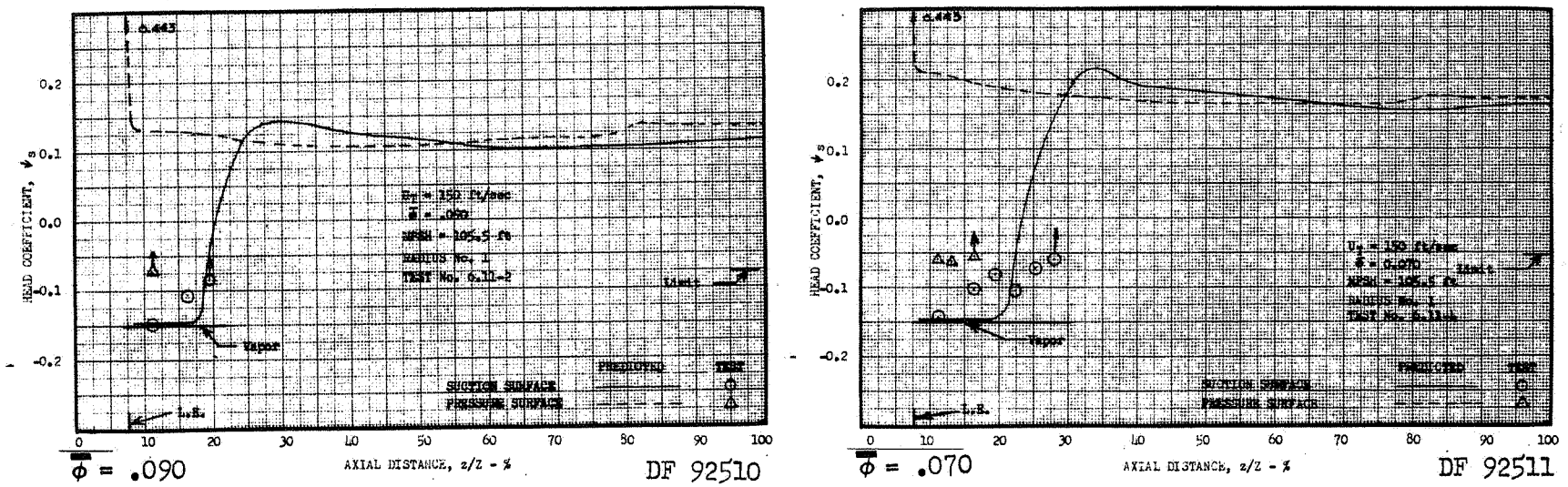

Figure 39. Noncavitating Blade Pressure Distribution; 8 deg (.14 rad) sweepback, Tip Streamline, U_T = 150 ft/sec (45.6 m/s), NPSH = 106 ft. (32.3 m).

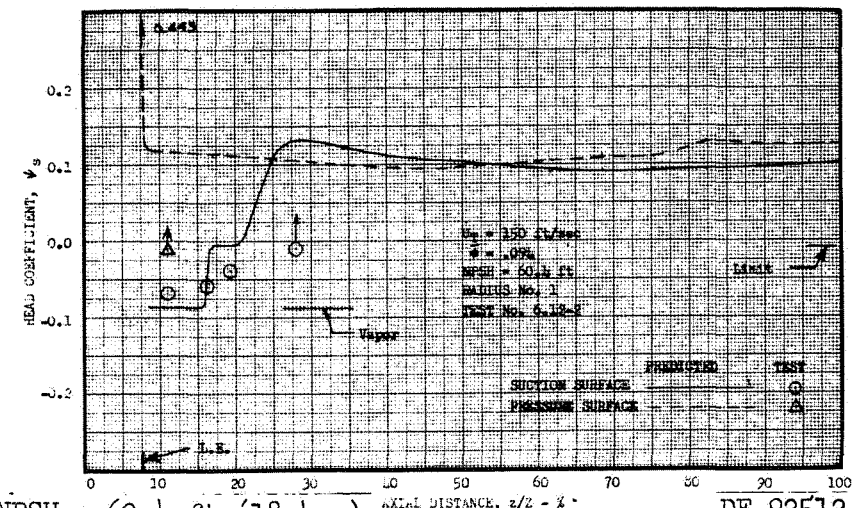

NPSH = 60.4 ft (18.4 m) DF 92512

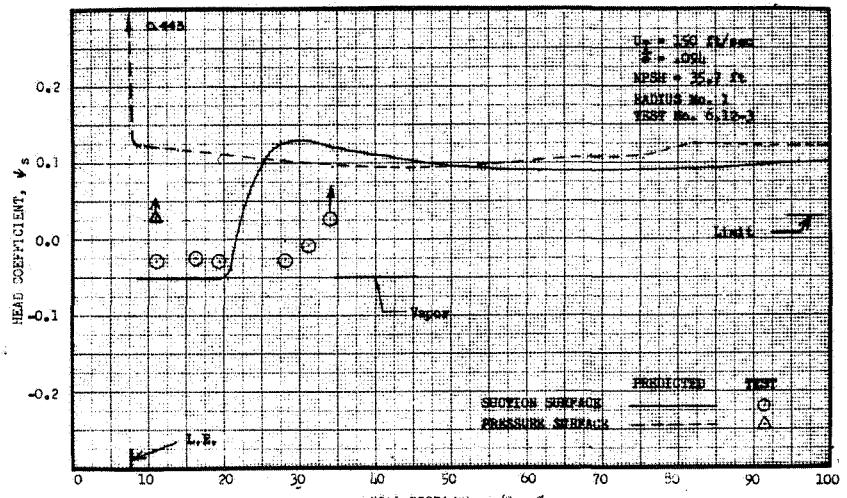

NPSH = 35.7 ft (10.9 m) DF 92513

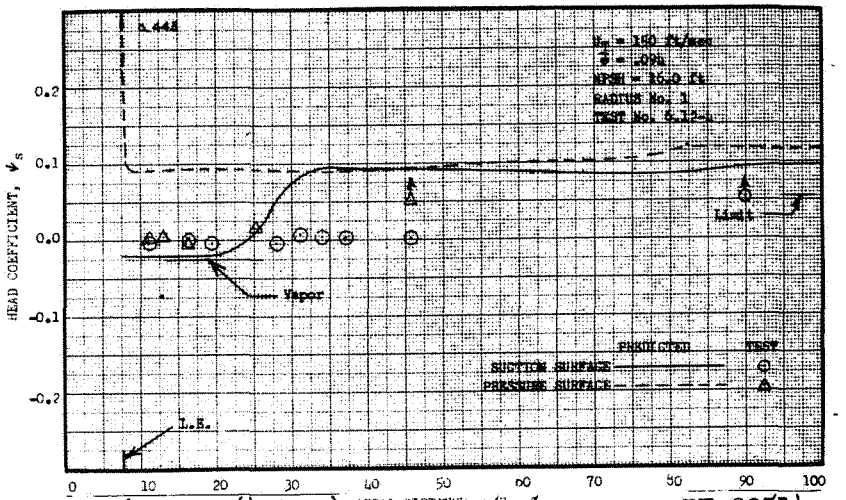

NPSH = 16.0 ft (4.9 m) DF 92514

Figure 40. Cavitating Blade Pressure Distribution; 8 deg (.14 rad) sweepback, Tip Streamline, U_T = 150 ft/sec (45.6 m/s), $\bar{\Phi}$ = .094.

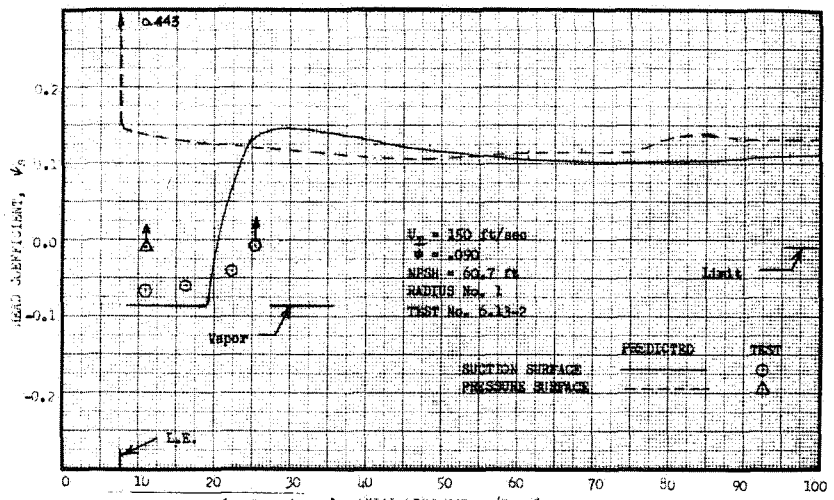

NPSH = 60.7 ft (18.5 m) DF 92515

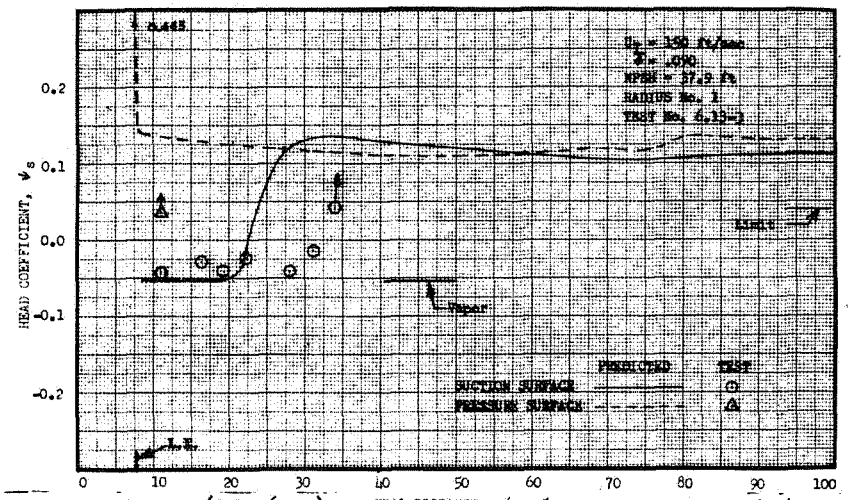

NPSH = 37.9 ft (11.6 m) DF 92516

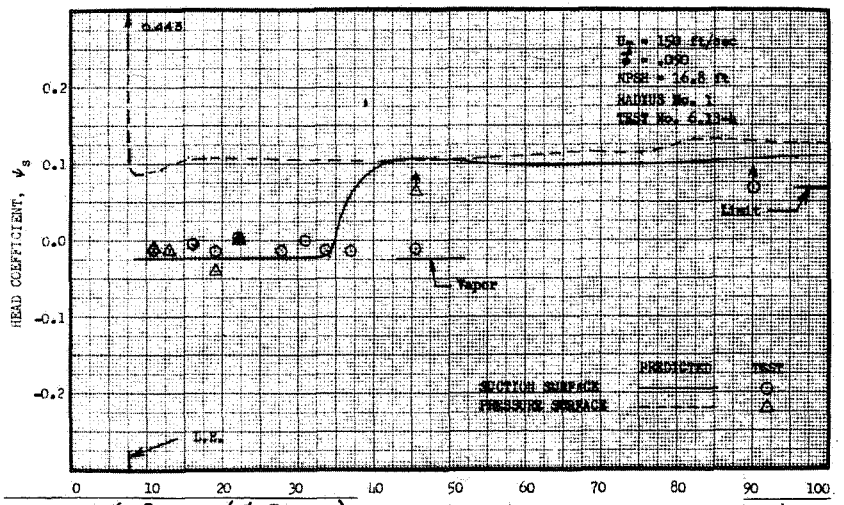

NPSH = 16.8 ft (5.12 m) DF 92517

Figure 41. Cavitating Blade Pressure Distribution; 8 deg (.14 rad) sweepback, Tip Streamline, U_T = 150 ft/sec (45.6 m/s), $\bar{\Phi}$ = .090.

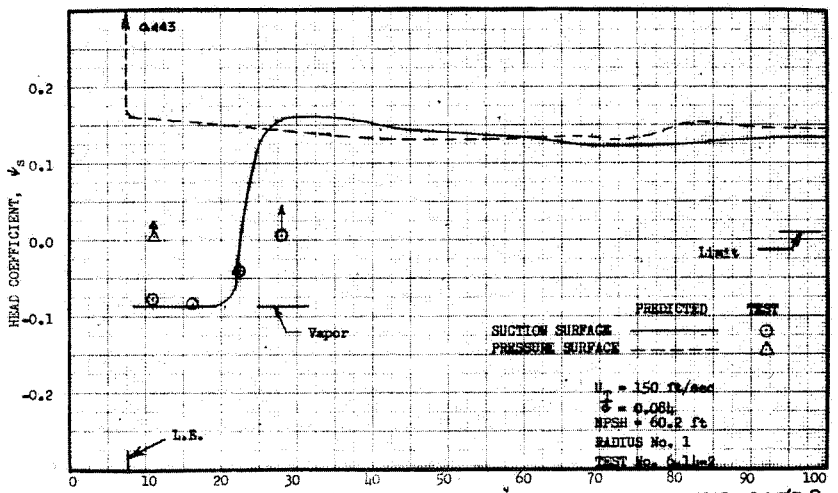

NPSH = 60.2 ft (18.3 m) DF 92518

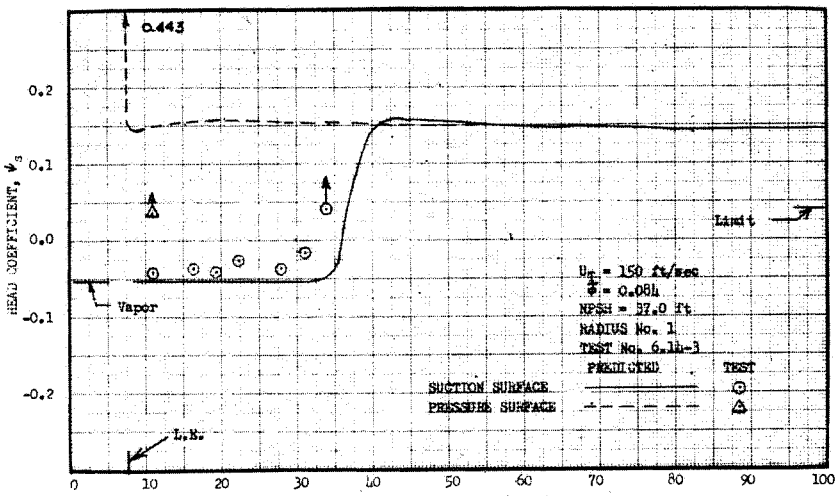

NPSH = 37.0 ft (11.3 m) DF 92519

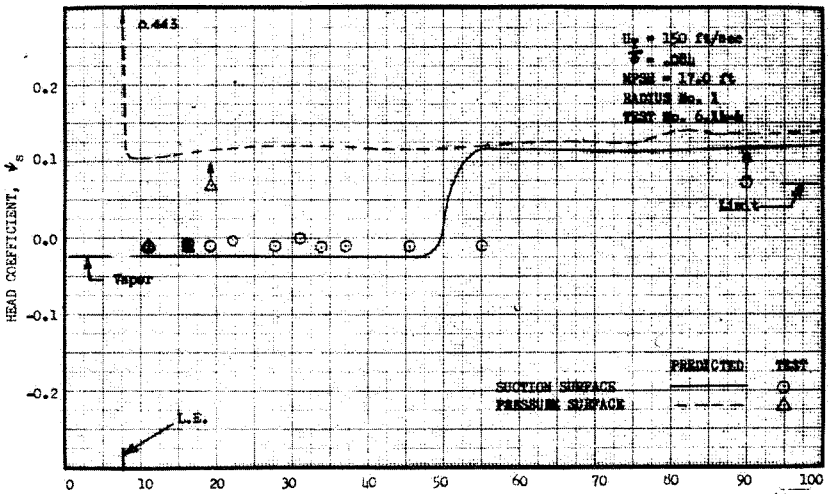

NPSH = 17.0 ft (5.2 m) DF 92520

Figure 42. Cavitating Blade Pressure Distribution; 8 deg (.14 rad) sweepback, Tip Streamline, U_T = 150 ft/sec (45.6 m/s), $\bar{\Phi}$ = .084.

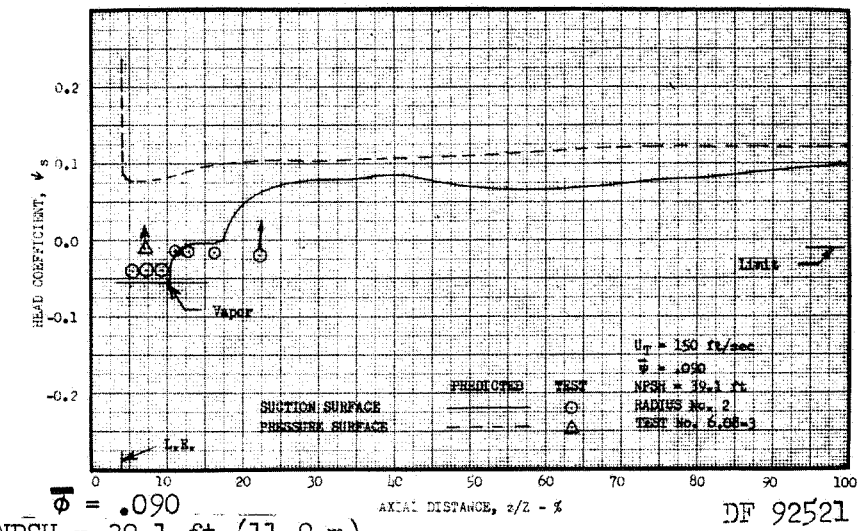

$\bar{\Phi}$ = .090
NPSH = 39.1 ft (11.9 m)

DF 92521

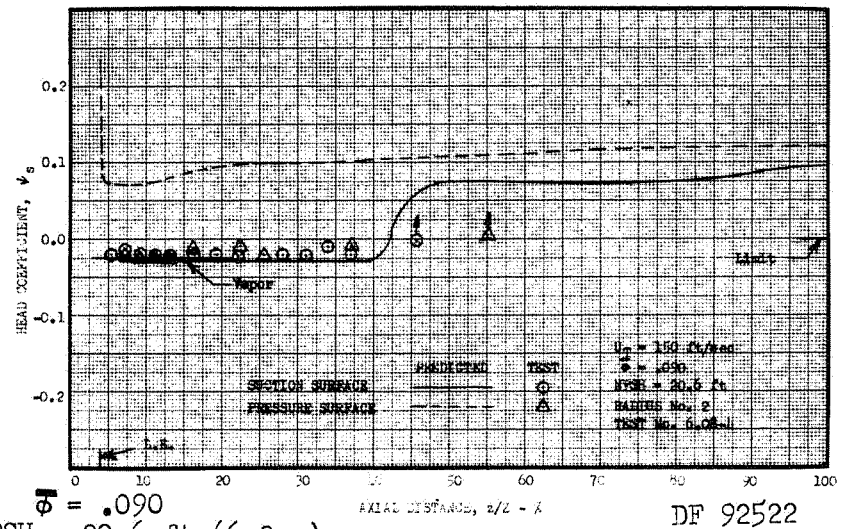

$\bar{\Phi}$ = .090
NPSH = 20.6 ft (6.3 m)

DF 92522

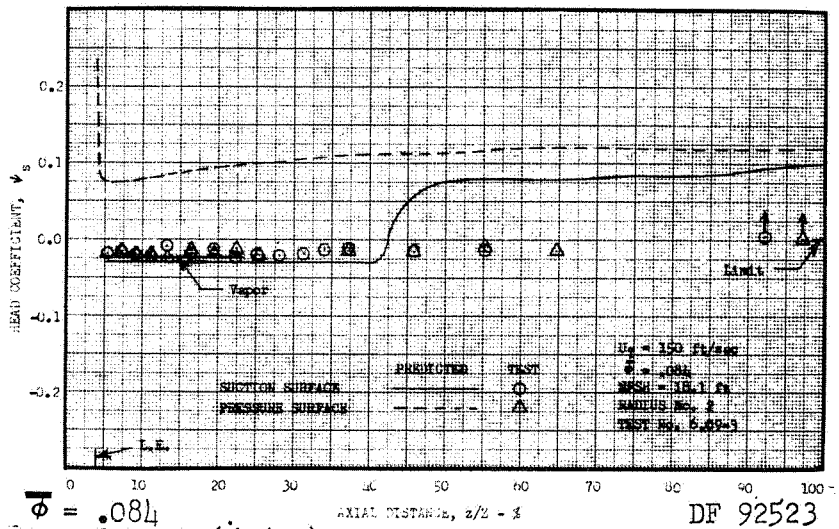

$\bar{\Phi}$ = .084
NPSH = 18.1 ft (5.5 m)

DF 92523

Figure 43. Cavitating Blade Pressure Distribution; 8 deg (.14 rad) sweepback, Midspan Streamline, U_T = 150 ft/sec (45.6 m/s).

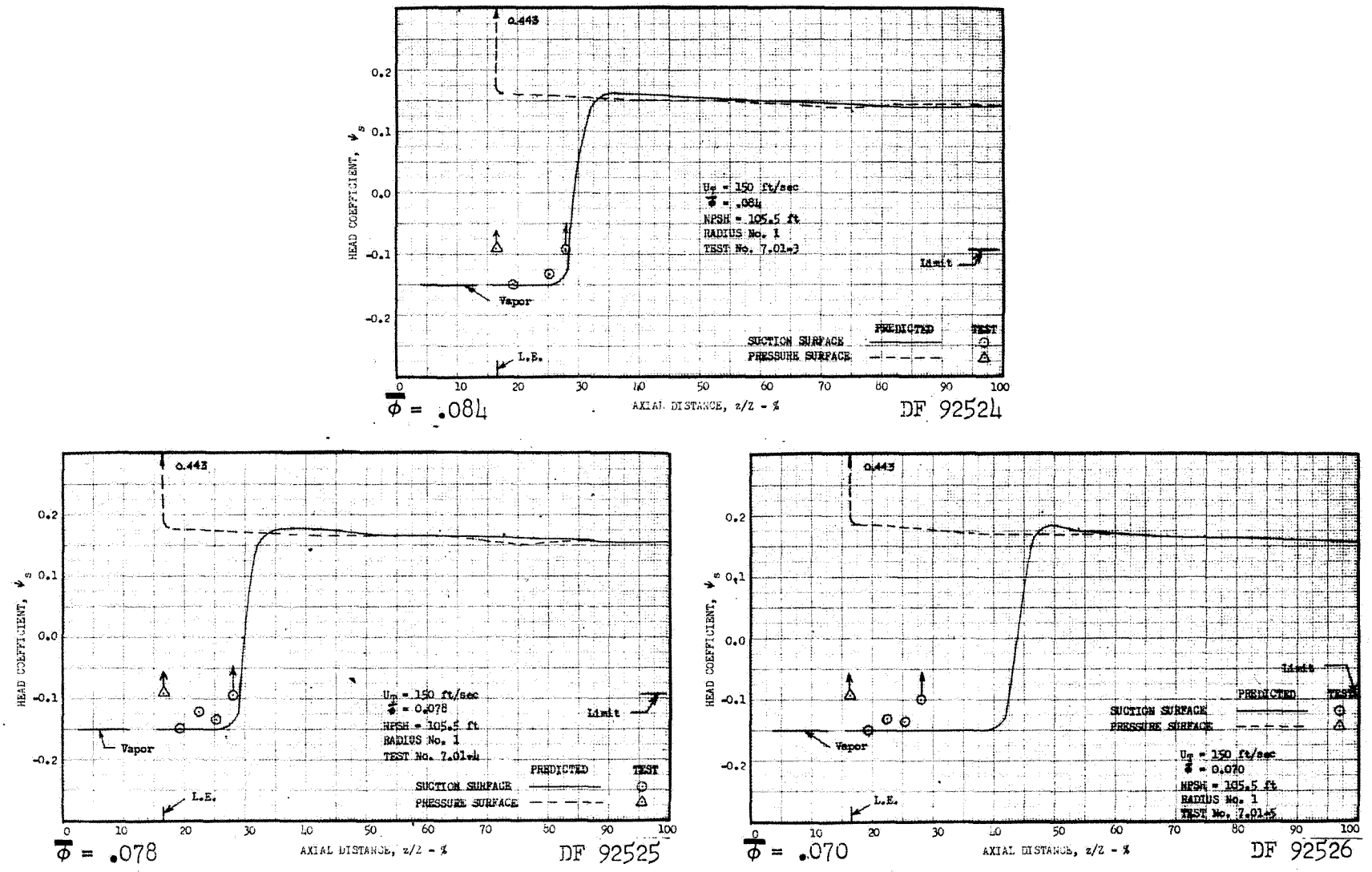

Figure 44. Noncavitating Blade Pressure Distribution; 16 deg (.28 rad) sweepback, Tip Streamline, U_T = 150 ft/sec (45.6 m/s), NPSH = 106 ft (32.3 m).

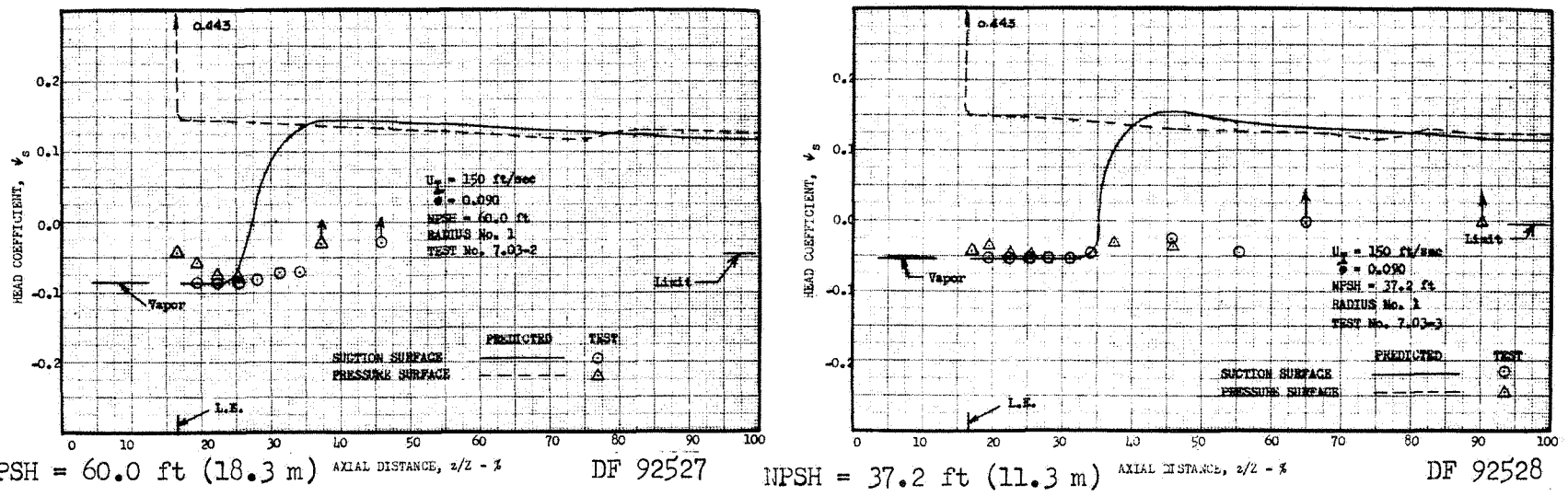

Figure 45. Cavitating Blade Pressure Distribution; 16 deg (.28 rad) sweepback, Tip Streamline, U_T = 150 ft/sec (45.6 m/s), $\bar{\Phi}$ = .090.

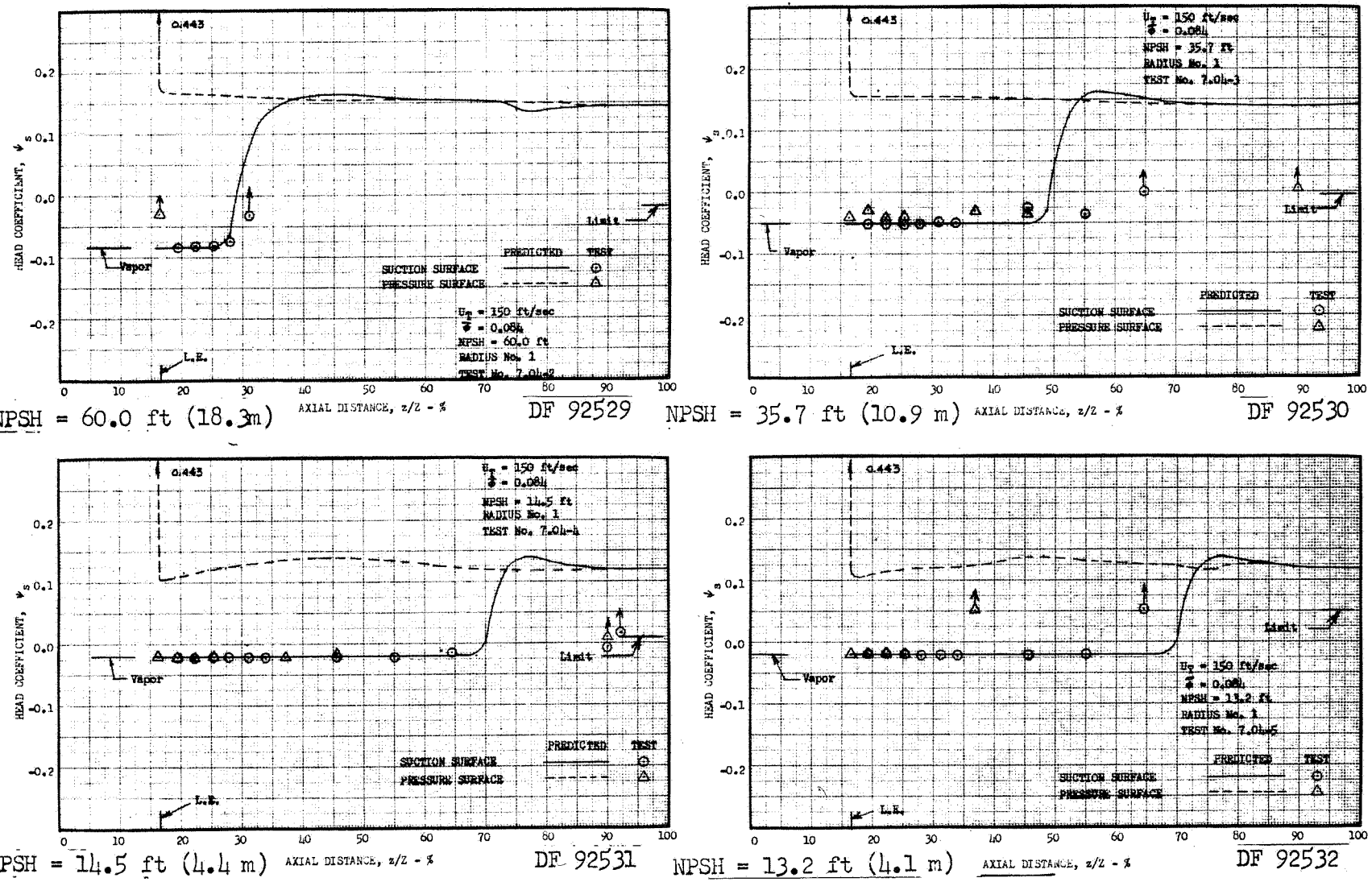

NPSH = 60.0 ft (18.3m) DF 92529 NPSH = 35.7 ft (10.9 m) DF 92530

NPSH = 14.5 ft (4.4 m) DF 92531 NPSH = 13.2 ft (4.1 m) DF 92532

Figure 46. Cavitating Blade Pressure Distribution; 16 deg (.28 rad) sweepback, Tip Streamline, U_T = 150 ft/sec (45.6 m/s), $\bar{\Phi}$ = .084.

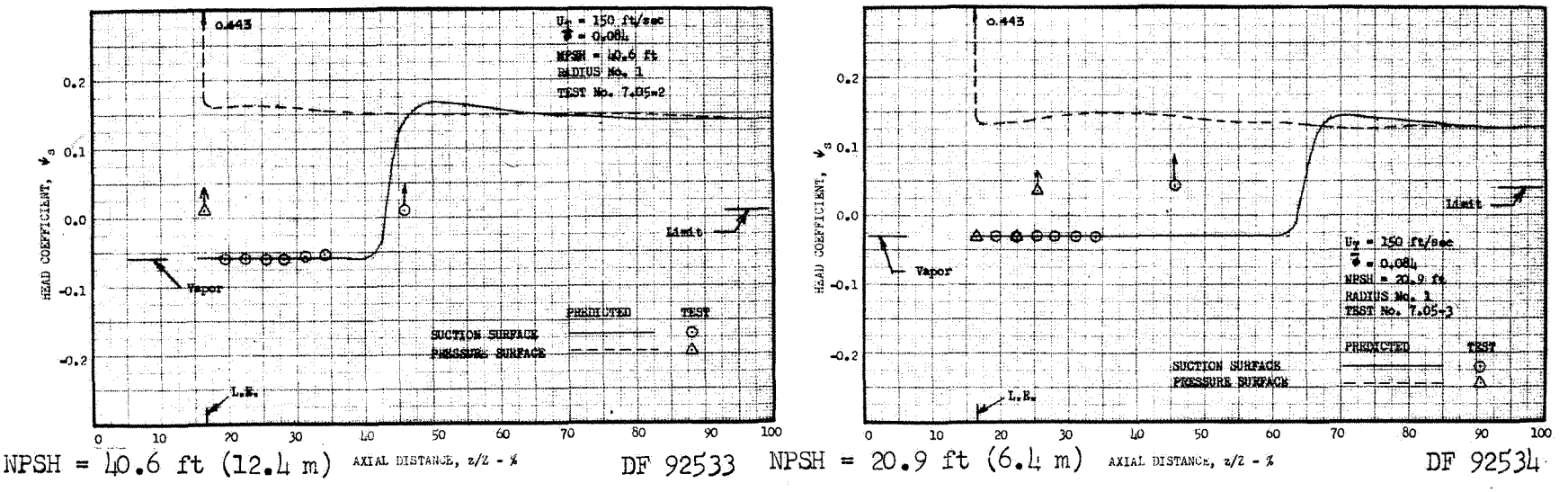

Figure 46. Cavitating Blade Pressure Distribution (Continued).

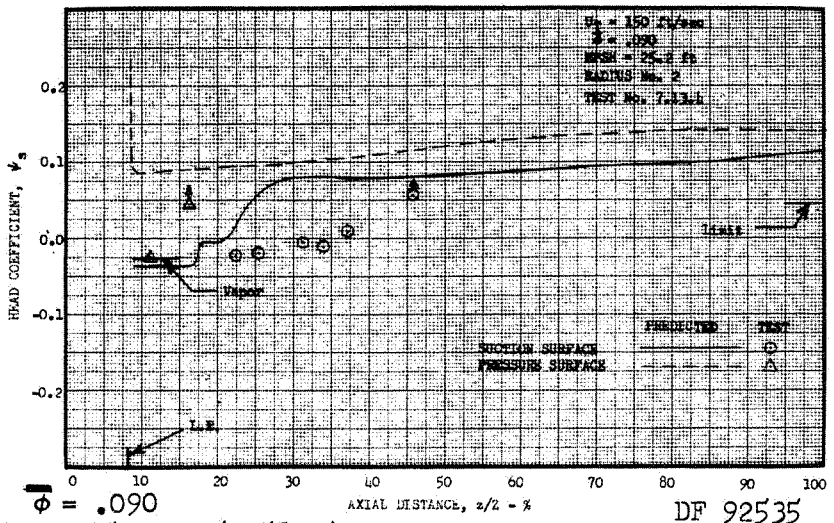

$\bar{\Phi}$ = .090
NPSH = 25.2 ft (7.68 m)
DF 92535

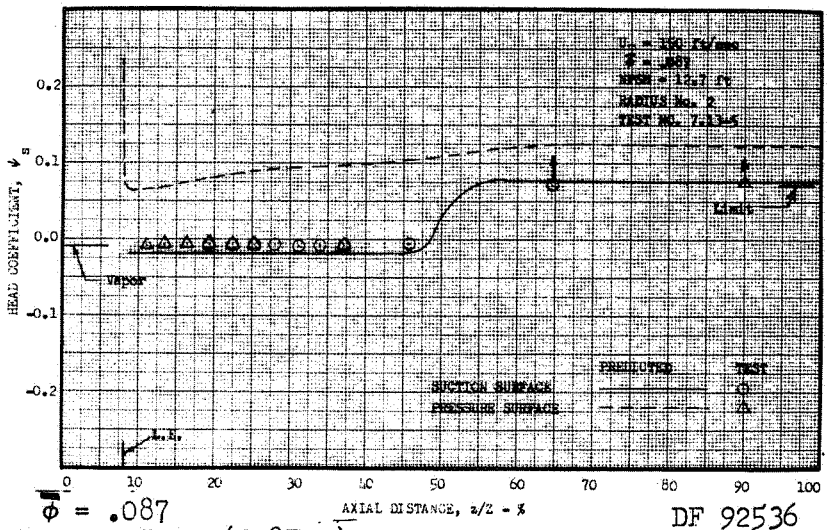

$\bar{\Phi}$ = .087
NPSH = 12.7 ft (3.87 m)
DF 92536

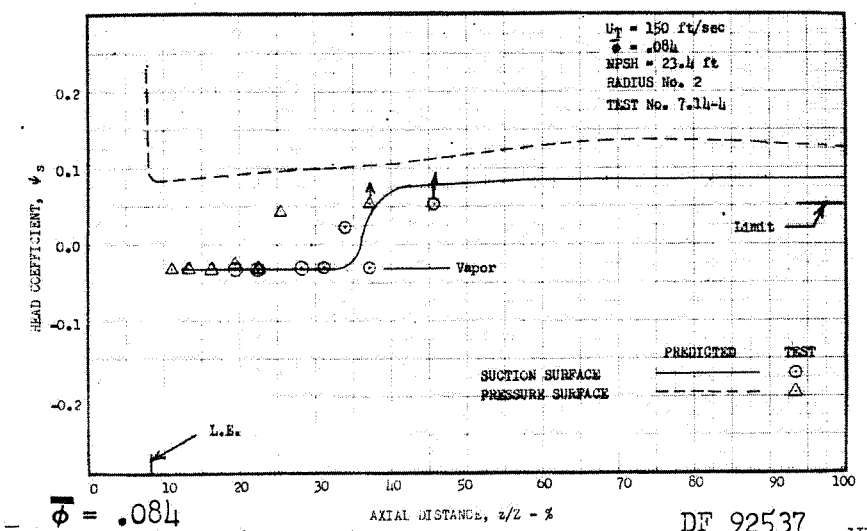

$\bar{\Phi}$ = .084
NPSH = 23.4 ft (7.13 m)
DF 92537

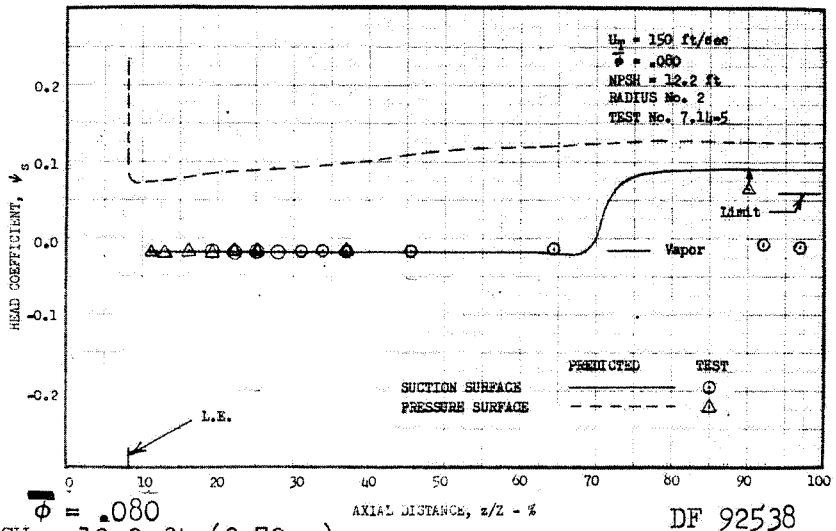

$\bar{\Phi}$ = .080
NPSH = 12.2 ft (3.72 m)
DF 92538

Figure 47. Cavitating Blade Pressure Distribution; 16 deg (.28 rad) sweepback, Midspan Streamline, U_T = 150 ft/sec (45.6 m/s).

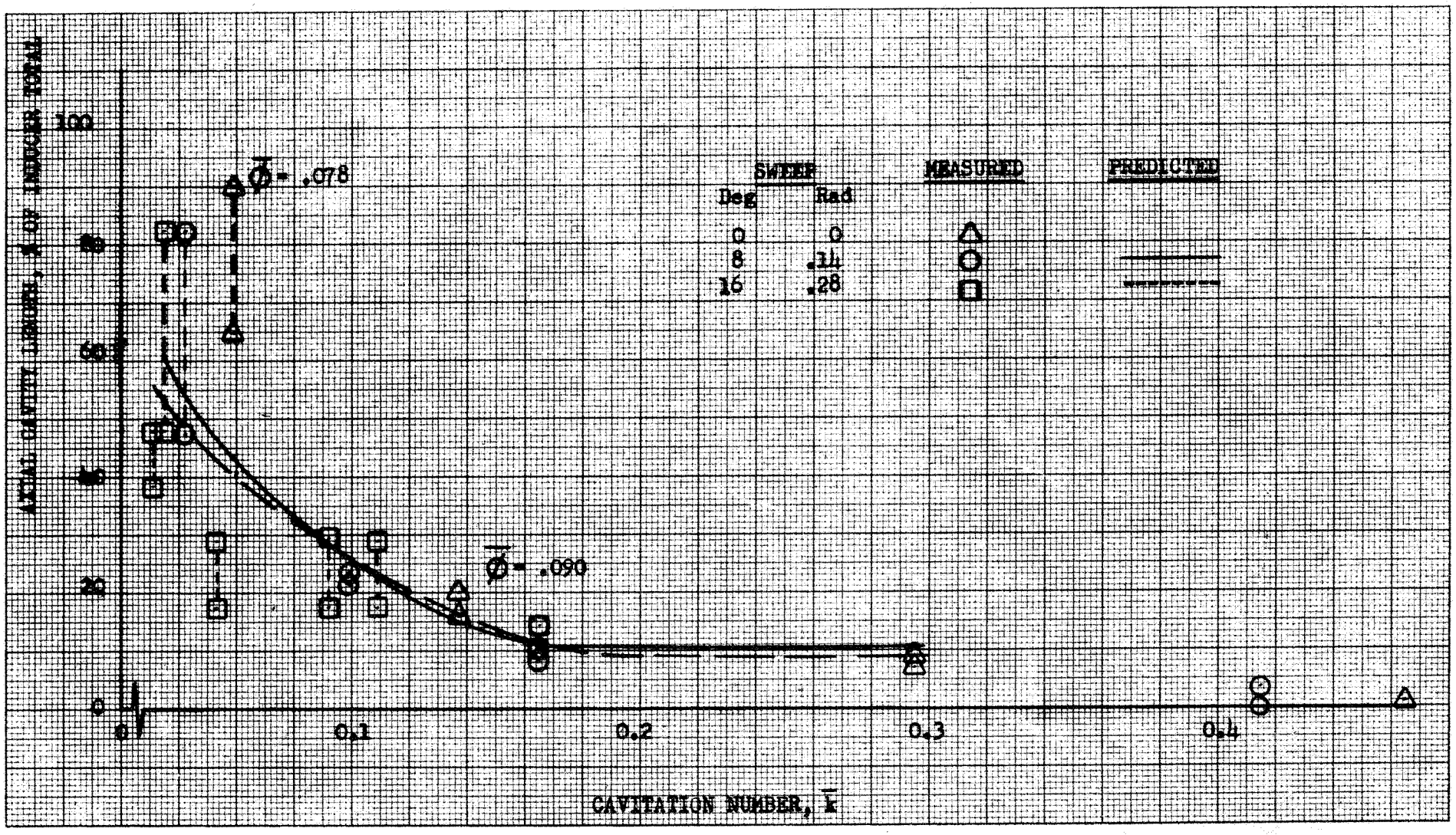

Figure 48. Comparison of Predicted with Measured Cavity Length Data (Tip Streamline). DF 92704
$\bar{\phi}$ = .084

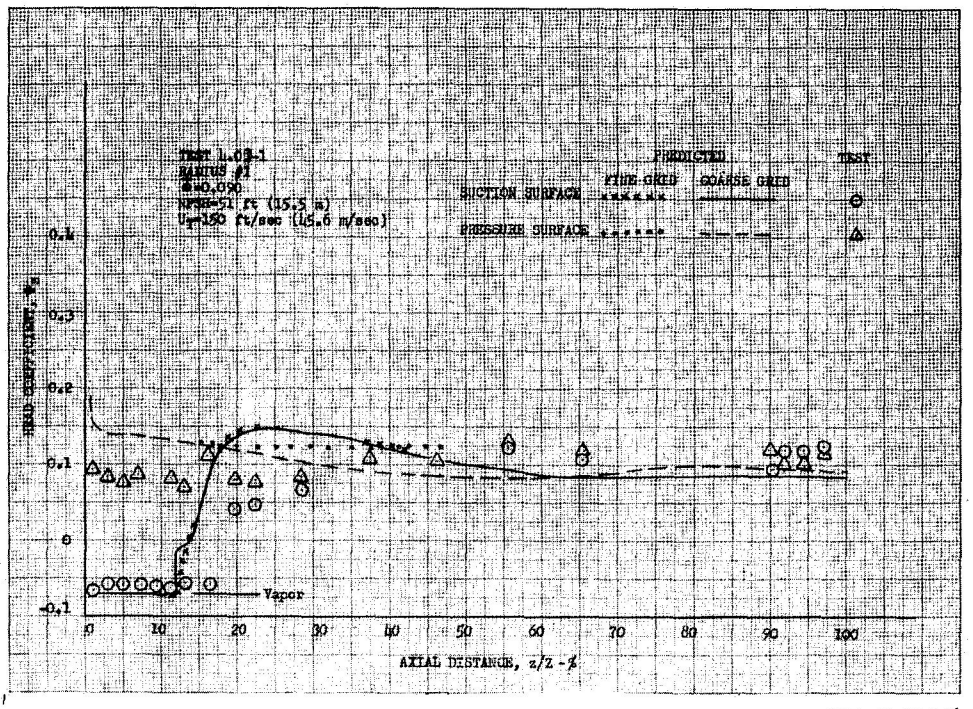

DF 92705

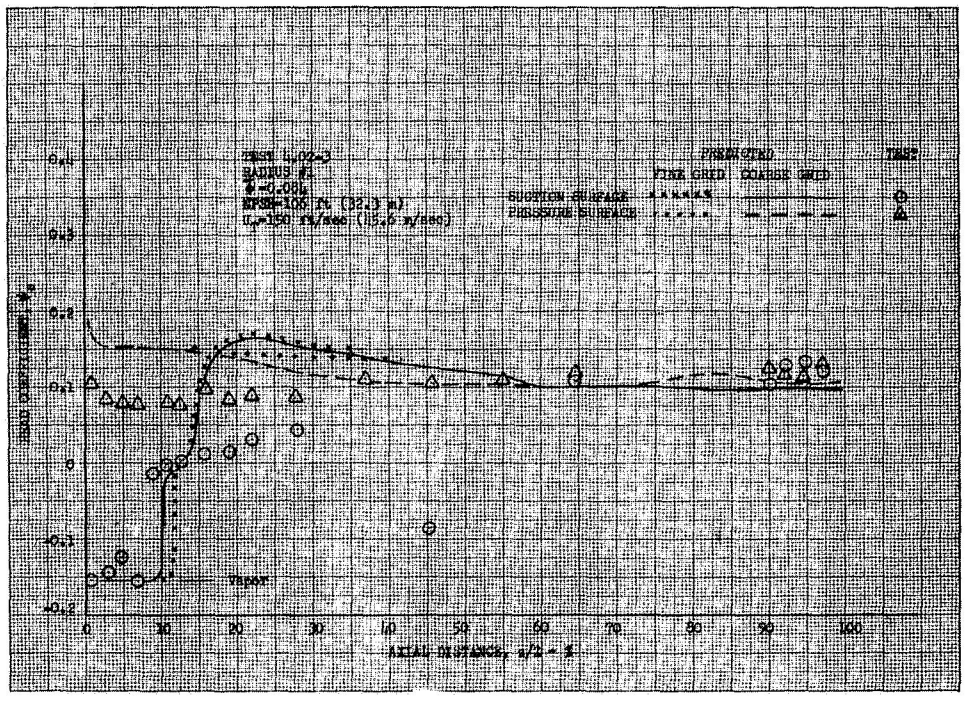

DF 92706

Figure 49. Effect of Grid Size on Blade Pressure Predictions, Radial Inducer.

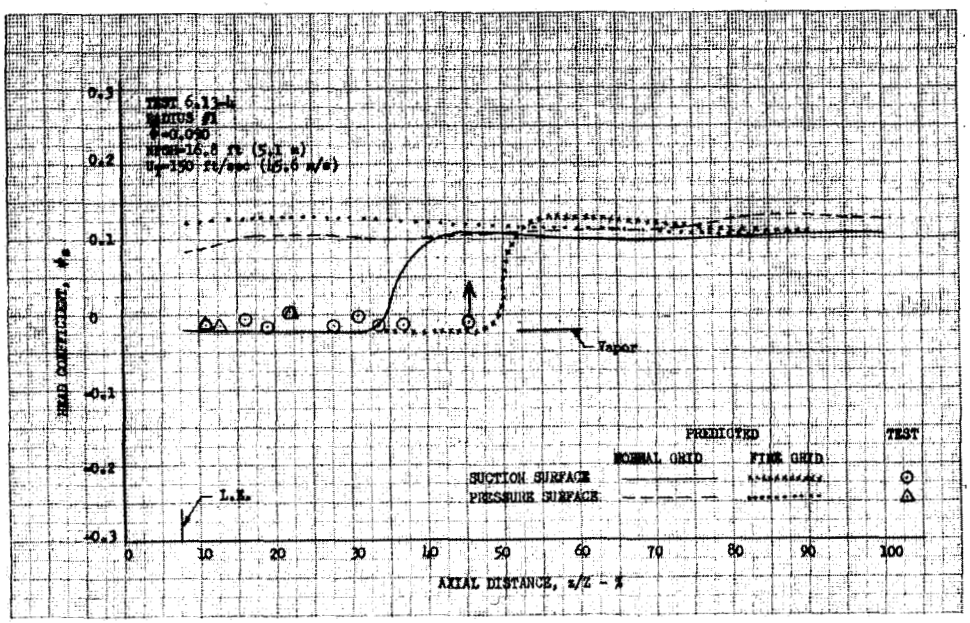

DF 92707

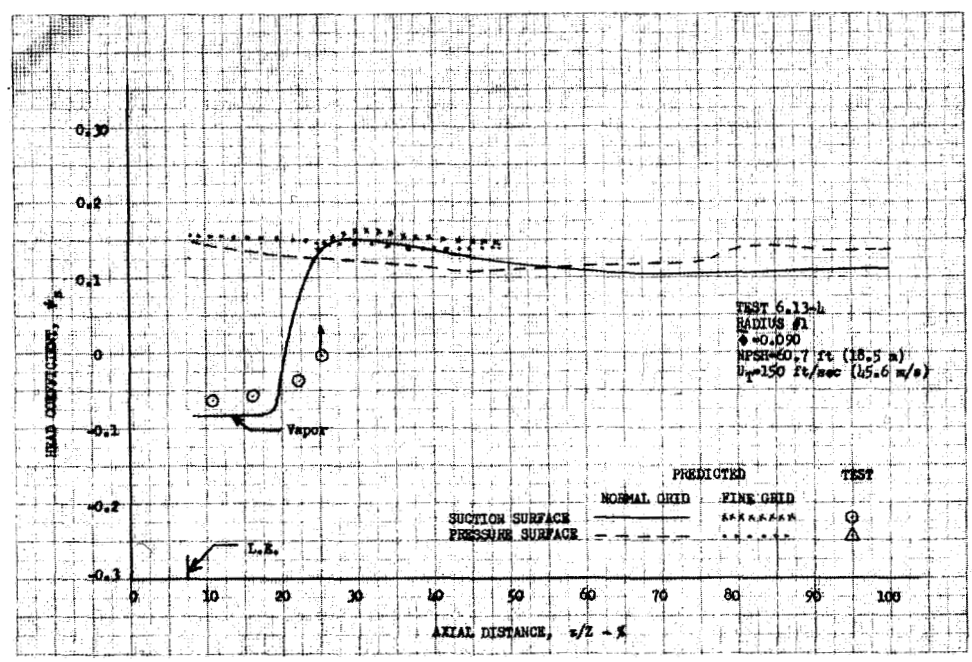

DF 92708

Figure 50. Effect of Grid Size on Blade Pressure Predictions, 8 deg (.14 rad) Sweepback Inducer.

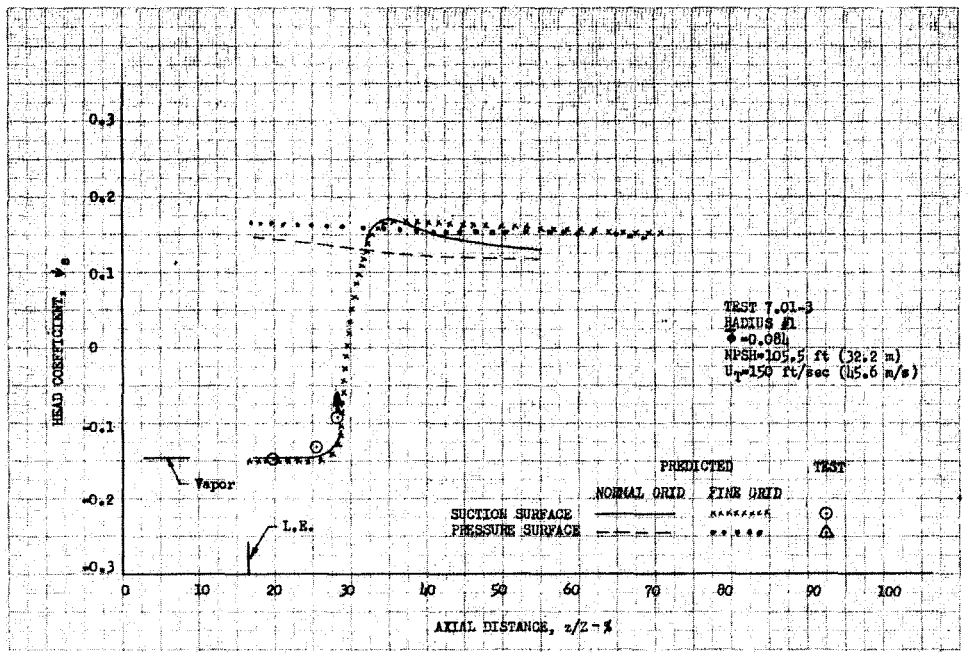

DF 92709

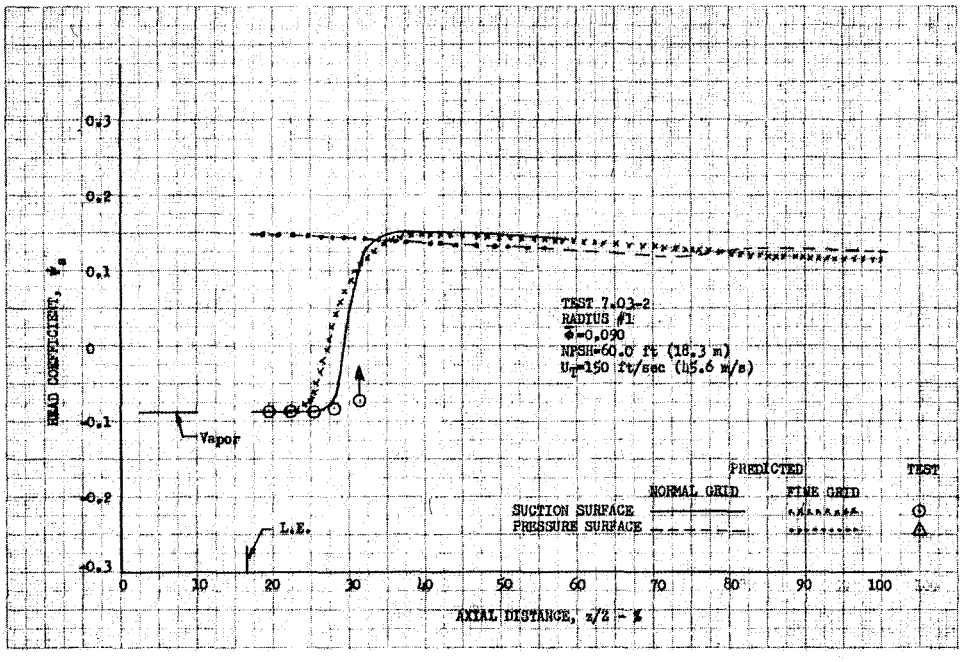

DF 92710

Figure 51. Effect of Grid Size on Blade Pressure Predictions, 16 deg (.28 rad) Sweepback Inducer.

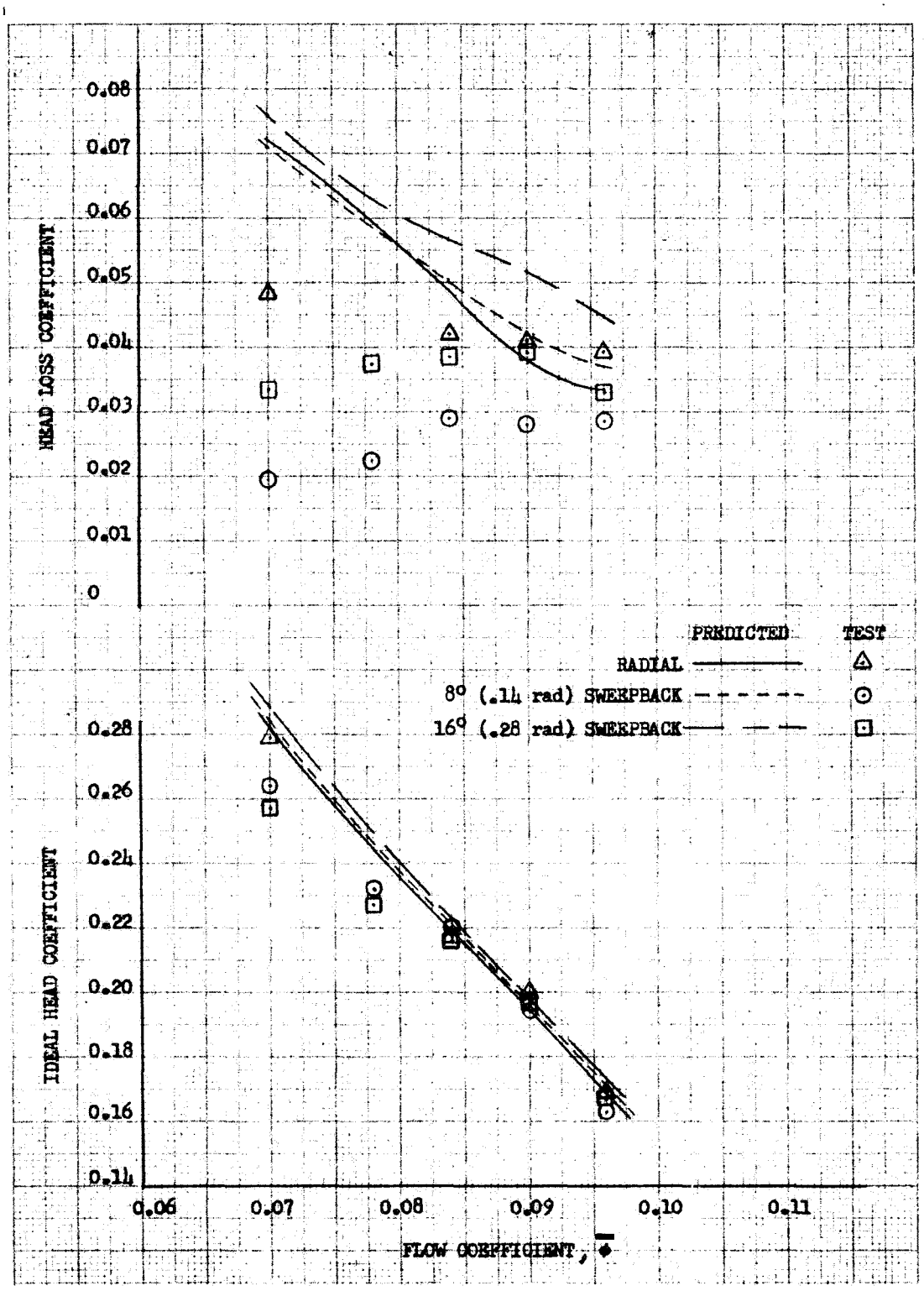

DF 92711

Figure 52. Measured and Predicted Variation of Ideal Head and Head Loss with Flow Coefficient (Noncavitating).

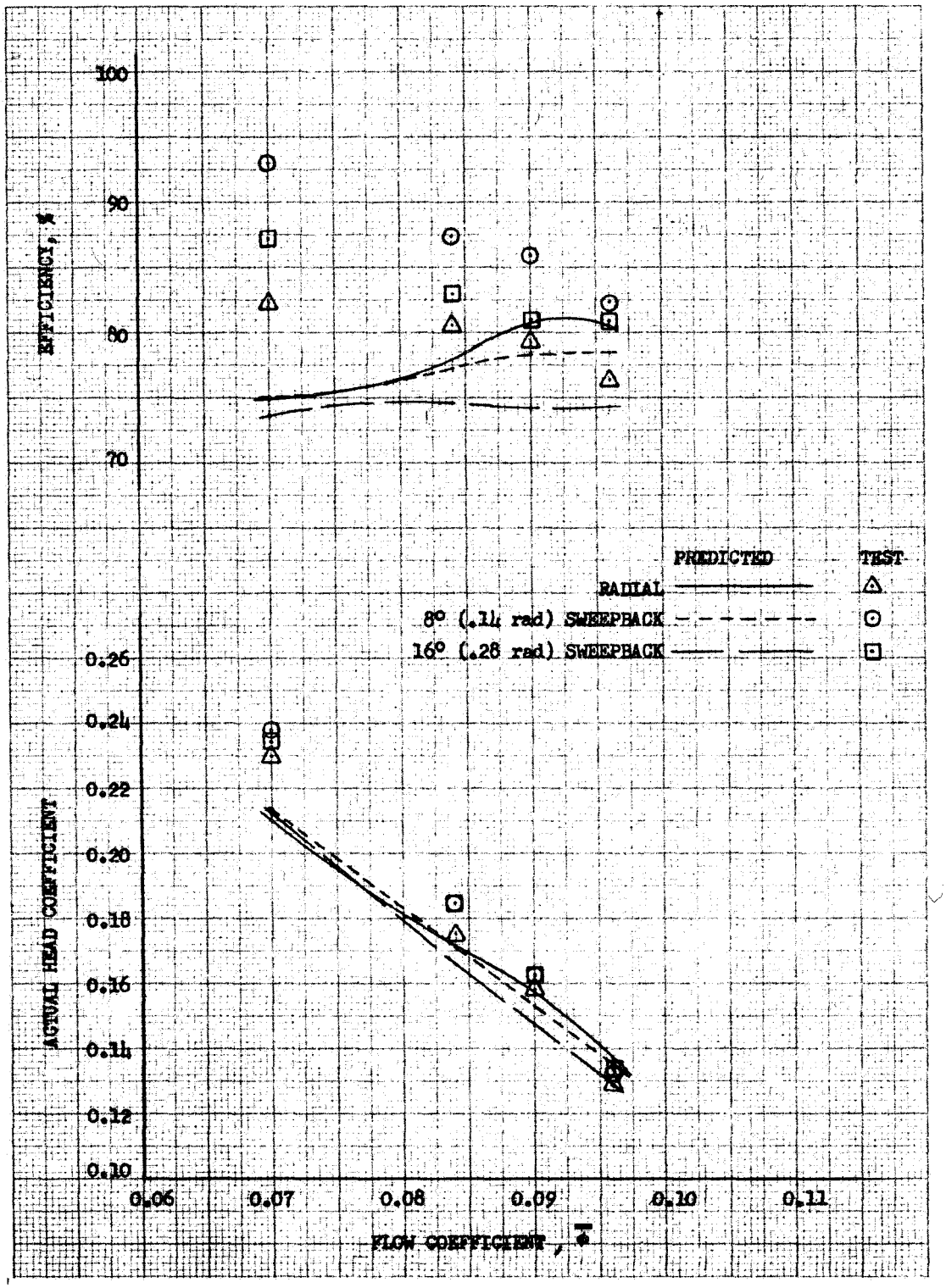

DF 92712

Figure 53. Measured and Predicted Variation of Efficiency and Actual Head with Flow Coefficient (Noncavitating).

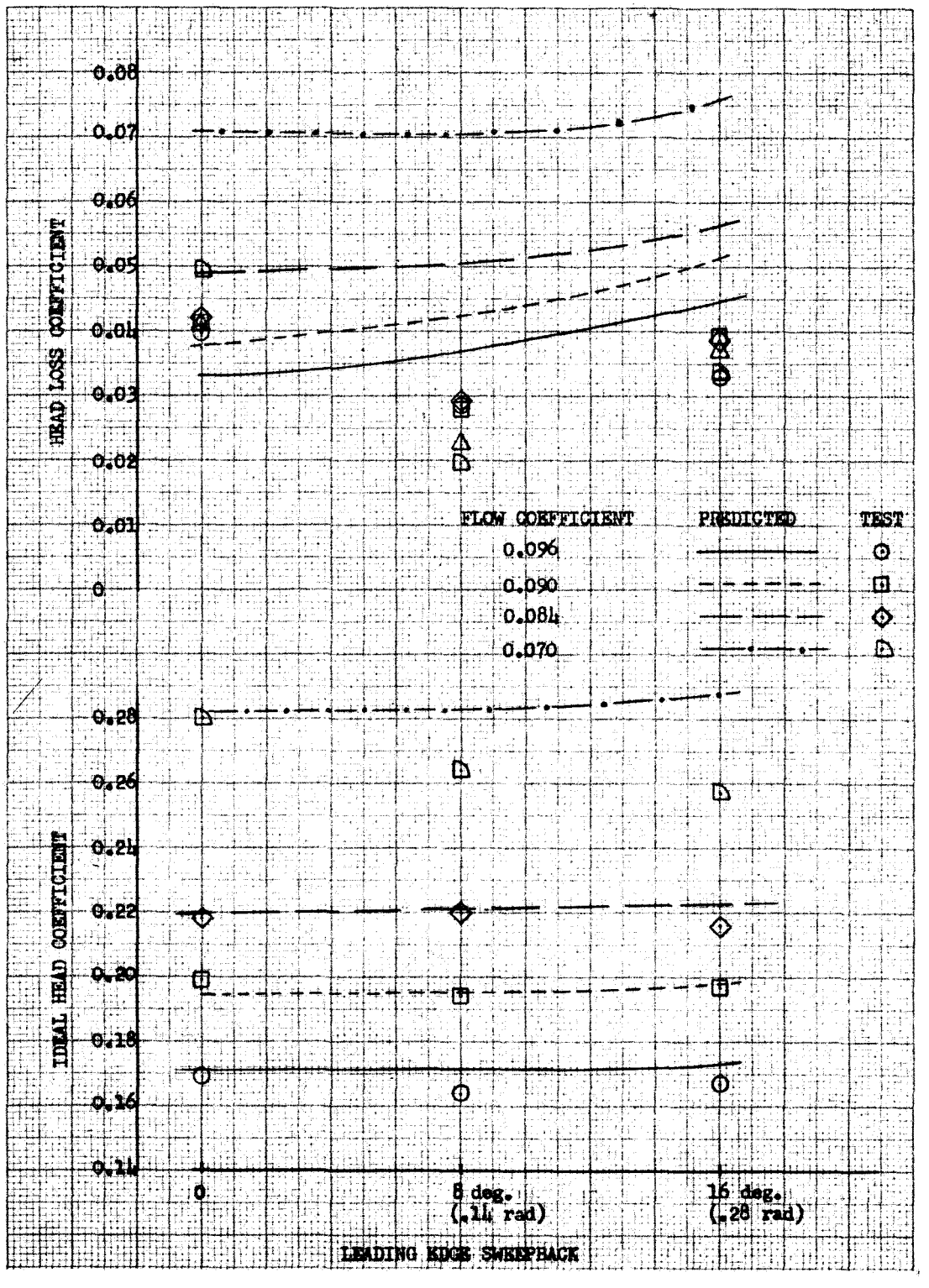

DF 92713

Figure 54. Measured and Predicted Variation of Ideal Head and Head Loss with Sweepback (Noncavitating).

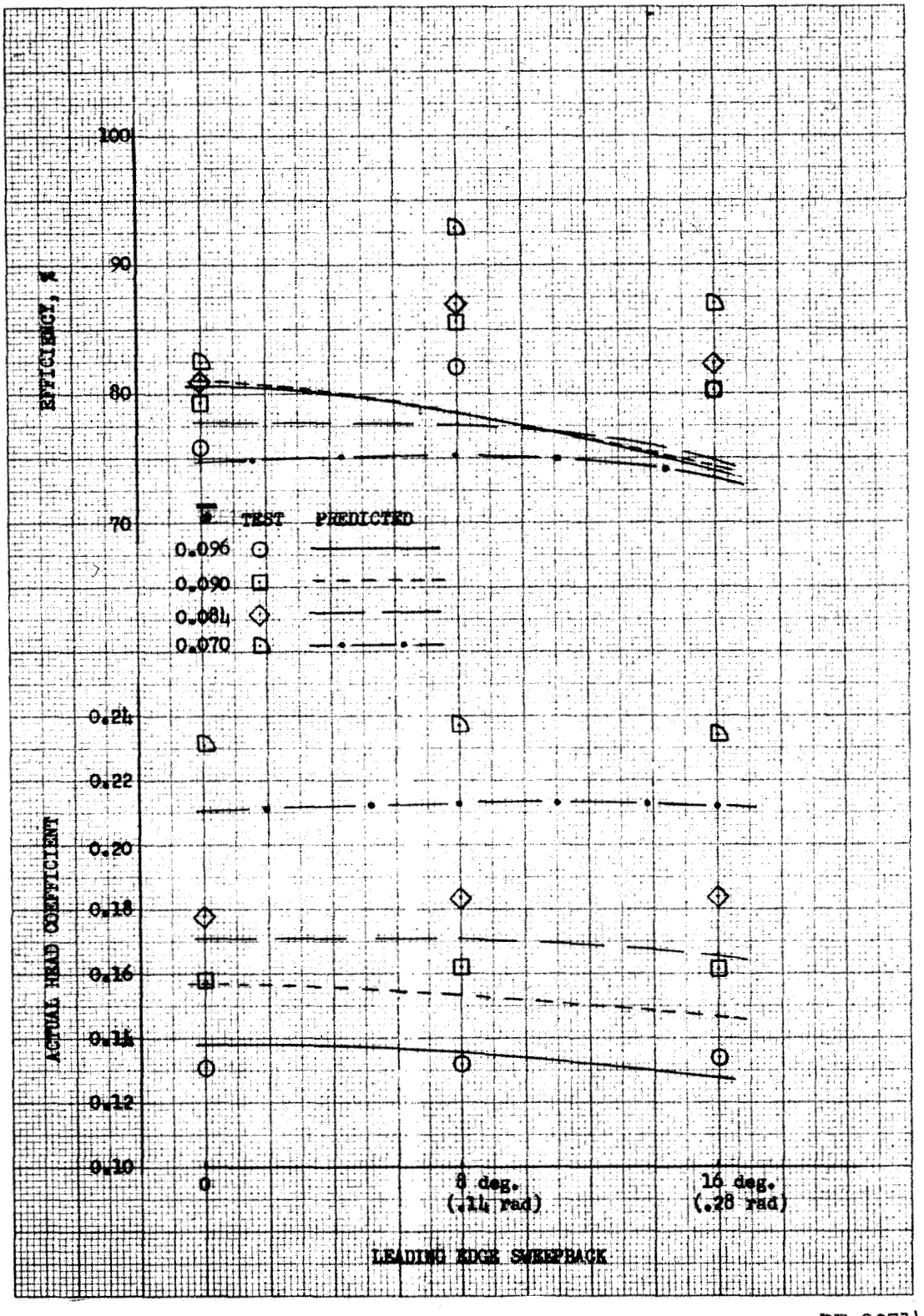

DF 92714

Figure 55. Measured and Predicted Variation of Efficiency and Actual Head with Sweepback (Noncavitating).

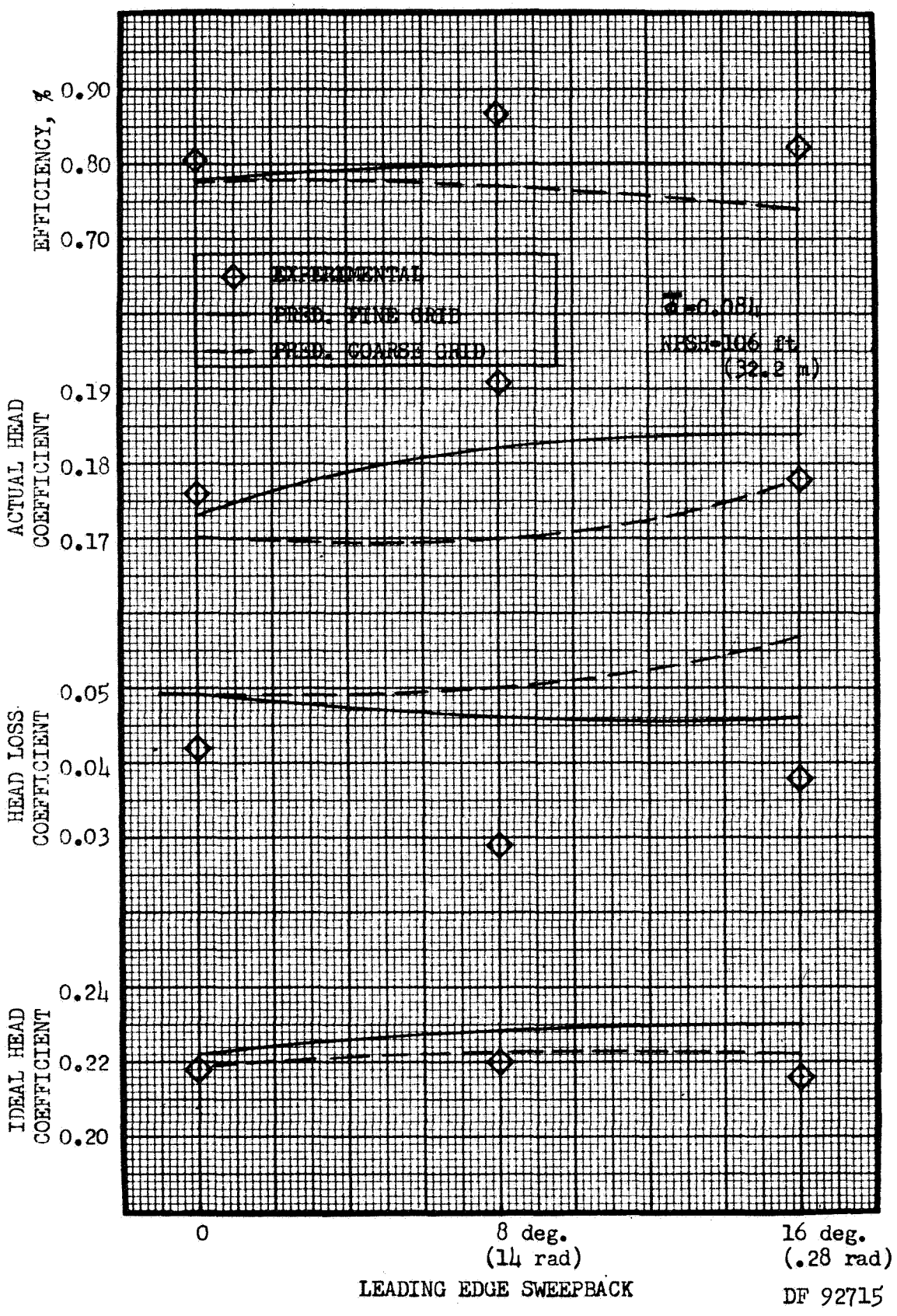

Figure 56. Effect of Input Grid Size on Predicted Inducer Performance.

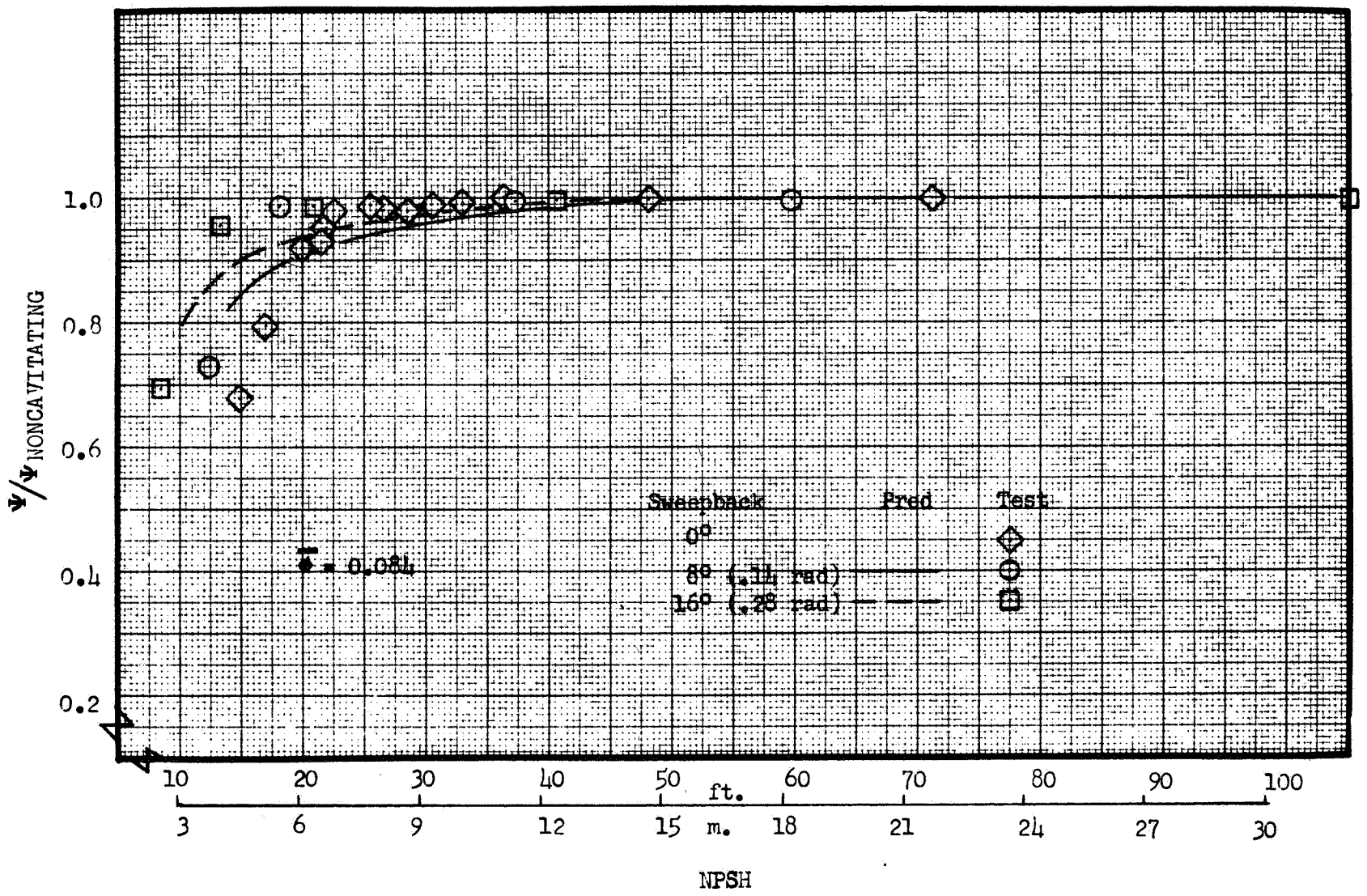

Figure 57. Comparison of Predicted and Measured Cavitating Performance Data.

DF 92716

SECTION VI
CONCLUSIONS AND RECOMMENDATIONS

A. Conclusions

1. The tip clearance flow model is an improvement to the hydrodynamic computer program. Ideal head vs. clearance predictions were in excellent agreement with the measured data. Loss (and efficiency) correlations were improved relative to previous, no-tip-clearance correlations but there is apparently room for further improvement in the loss predictions. The measured data show a loss "bucket" indicating an optimum clearance while the flow model cannot predict such a bucket.

2. Blade pressure loading data were not strongly effected by leading edge sweepback at inlet pressures where cavitation cavities were relatively small and blade loadings highest. Differences between predicted and measured data were also small in this region. Predicted data differs considerably from the measured when cavities are relatively large (greater than 30% of inducer axial length) and the predicted data shows a trend of decreasing cavity size with sweepback. This predicted trend is in agreement with the measured trend. Differences between predicted and measured data may be associated with inlet flow prerotation.

3. The sweepback model does not adequately account for the effects of sweepback on noncavitating performance. Ideal head predictions are in good agreement with the measured data but loss predictions differ considerably. The measured data indicate the existence of an optimum sweepback but predicted loss gradually increases with sweep. Differences between predicted and measured data may be associated with prerotation which was not accounted for in the analysis and/or with cavity losses.

4. The sweepback model adequately predicts the effects of sweepback on cavitating performance. Measured and predicted suction specific speed capability increase as sweepback increases.

B. Recommendations

1. The inducer computer program convergence should be improved to permit more accurate predictions for swept, cavitating inducers.

2. The inducer cavity model should be refined, to improve blade loading and loss predictions. This could be accomplished by conducting additional inducer tests over a wide range of inlet pressures and flows, determining cavity geometries through static pressure measurements and/or laser velocimetry, and correlating the data against predictions.

3. A model for the prediction of inlet prerotation flow profiles should be developed. The model could be empirical and based on previous inducer test data.

SECTION VII
REFERENCES

1. Pratt & Whitney Aircraft, "Study of Inducer Load and Stress", Final Report NASA Contract NAS3-11216, CR72712 Vol. I, Dec, 1970.

2. Pratt & Whitney Aircraft, "Study of Inducer Load and Stress", Final Report NASA Contract NAS3-11216, CR72712 Vol. II, November, 1972.

3. Young, W. E., R. Murphy, and J. M. Reddecliff, "Study of Cavitating Inducer Instabilities, Final Report", Pratt & Whitney Aircraft FR-5131, Contract NAS8-27625, August, 1972.

4. Rains, D. A., "Tip Clearance Flow in Axial Flow Compressors and Pumps", Calif. Instit. of Tech. Report No. 5, June 1954.

5. Lakshminarayana, B., "Methods of Predicting the Tip Clearance Effects in Axial Flow Turbomachinery," ASME Paper No. 69-WA/FE-26, September 1970.

6. Lakshminarayana, B. and J. H. Horlock, "Tip Clearance Flow and Losses for an Isolated Compressor Blade", Great Britian ARC R&M No. 3316, June 1962.

APPENDIX

Nomenclature

Symbol	Description	Units
A	Channel flow area	L^2
a	Vortex radius	L
AR	Aspect ratio, average blade height/tip chord	D'less
b	Length of vortex sheet rolled up	L
C	Tip clearance	L
g	Gravitational constant	LT^{-2}
H	Total head	L
h	Static head	L
h_v	Fluid vapor head	L
HI	Ideal head rise	L
k	Fraction of lift retained at the blade tip	D'less
$\bar{k}$	Blade tip cavitation number	D'less
ℓ	Distance along tip vortex axis	L
m	Distance normal to the ℓ direction	L
M	Defined in text	
N	Defined in text	
Nss	Suction specific speed (conventional $\frac{RPM\sqrt{GPM}}{NPSH^{.75}}$)	
NI	Number of radial stations or streamlines	D'less
NJ	Number of axial stations	D'less
NPSH	Net positive suction head	L
P_T	Total Pressure	$F\,L^{-2}$
Q	Volume flow	$L^3\,T^{-1}$
QI	Integrated volume flow from traverse	$L^3\,T^{-1}$
R	Radius	L
UT	Inducer tip velocity	LT^{-1}
V	Fluid absolute velocity	LT^{-1}
W	Fluid relative velocity	LT^{-1}
Z	Axial distance	L
α	Sweepback cone angle or flow angle from tangential	Deg. or Rad
$\Delta\beta$	Induced relative flow angle	Deg. or Rad
β^*	Blade angle from tangential	Deg. or Rad
Γ	Circulation	$L^2\,T^{-1}$
γ	Vortex Strength	LT^{-1}
η	Efficiency	D'less
λ	Angle between suction and pressure side relative velocities at the tip	Deg. or Rad
ρ	Fluid density	
ϕ	Flow coefficient	D'less
ψ	Head coefficient	D'less
ψ_a	Actual head coefficient	D'less
ψ_i	Ideal head coefficient	D'less
ψ_ℓ	Head loss coefficient	D'less
ψ_s	Blade static head coefficient	D'less
ω	Angular velocity	T^{-1}
σ	Blade solidity	D'less
τ	Blade tangential spacing	L

Superscripts:

′	Previous value
-	Average value

Subscript

e	Inducer exit
F	Forced vortex
H	Inducer hub
I	Induced flow field
i	Radial station
j	Axial station
NC	Induced velocity
o	Inducer inlet
p	Pressure surface
s	Suction surface
T	Inducer tip
TC	Tip clearance
u	Tangential component
z	Axial component
∞	Upstream

Distribution List
For Report No. CR-72712
Volume III

		Copies
National Aeronautics and Space Administration Lewis Research Center 21000 Brookpark Road Cleveland, Ohio 44135		
Attn:	T. J. Flanagan Mail Stop 500-313	1
	Technical Report Control Office Mail Stop 5-5	1
	Technology Utilization Office Mail Stop 3-19	1
	AFSC Liaison Office Mail Stop 501-3	2
	Library Mail Stop 60-3	1
	M. J. Hartmann Mail Stop 5-9	1
	D. W. Drier Mail Stop 21-4	1
	R. L. Lantz Mail Stop 21-4	1
	W. E. McKissock Mail Stop 21-4	1
	D. D. Scheer Mail Stop 500-203	6
	J. C. Montgomery Mail Stop 54-5	1
	R. E. Connelly Mail Stop 500-116	1

	Copies
National Aeronautics and Space Administration Washington, D. C. 20546	
Attn: Code RPX	2
RPL	1
Scientific and Technical Information Facility P. O. Box 33 College Park, Maryland 20740	
Attn: NASA Representative Code CRT	6
National Aeronautics and Space Administration Ames Research Center Moffett Field, California 94035	
Attn: Library	1
National Aeronautics and Space Administration Flight Research Center P. O. Box 273 Edwards, California 93523	
Attn: Library	1
National Aeronautics and Space Administration Goddard Space Flight Center Greenbelt, Maryland 20771	
Attn: Library	1
National Aeronautics and Space Administration John F. Kennedy Space Center Kennedy Space Center, Florida 32899	
Attn: Library	1
National Aeronautics and Space Administration Langley Research Center Langley Station Hampton, Virginia 23365	
Attn: Library	1

		Copies
National Aeronautics and Space Administration Manned Spacecraft Center Houston, Texas 77058		
Attn:	Library	1
National Aeronautics and Space Administration George C. Marshall Space Flight Center Marshall Space Flight Center, Alabama 35812		
Attn:	Library	1
	Keith Chandler	1
	Loren Gross	1
Jet Propulsion Laboratory 4800 Oak Grove Drive Pasadena, California 91103		
Attn:	Library	1
U. S. Atomic Energy Commission AEC-NASA Space Nuclear Propulsion Office Washington, D. C. 20546		
Attn:	F. C. Schwenk	1
Chemical Propulsion Info. Agency Applied Physics Laboratory 8621 Georgia Avenue Silver Spring, Maryland 20910		1
Defense Documentation Center Cameron Station Alexandria, Virginia 22314		1
Office of the Director of Defense Research and Engineering Washington, D. C. 20301		1
Advanced Research Projects Agency Washington , D. C. 20525		
Attn:	D. E. Mock	1
Research and Technology Division Air Force Systems Command Bolling Air Force Base Washington, D. C. 20332		
Attn:	RTD (RTNP)	1

	Copies
Arnold Engineering Development Center Air Force Systems Command Tullahoma, Tennessee 37389	
Attn: AEOIM	1
Air Force Aero Propulsion Laboratory Research and Technology Division Air Force Systems Command United States Air Force Wright Patterson AFB, Ohio 45433	
Attn: APRP	1
Aeronautical Systems Division Air Force Systems Command Wright Patterson Air Force Base, Dayton, Ohio 45433	
Attn: Library	1
Air Force Missile Test Center Patrick Air Force Base, Florida 32925	
Attn: L. J. Ullian	1
Air Force Systems Command Andrews Air Force Base Washington, D. C. 20332	
Attn: SCLT	1
Air Force Rocket Propulsion Laboratory (RPR) Edwards Air Force Base, California 93523	1
Air Force Office of Scientific Research Washington, D. C. 20333	
Attn: SREP, Dr. J. F. Masi	1
Office of Research Analyses (OAR) Holloman Air Force Base, New Mexico 88330	
Attn: Library	1
Commanding Officer U. S. Army Research Office (Durham) Box CM, Duke Station Durham, North Carolina 27706	1

	Copies
U. S. Army Missile Command Redstone Scientific Information Center Redstone Arsenal, Alabama 35808	
Attn: Chief, Document Section	1
Bureau of Naval Weapons Department of the Navy Washington , D. C. 20360	
Attn: J. Kay, Code RTMS-41	1
Commander U. S. Naval Missile Center Point Mugu, California 93041	
Attn: Technical Library	1
Commanding Officer Office of Naval Research 1030 E. Green Street Pasadena, California 91101	1
Director (Code 6180) U. S. Naval Research Laboratory Washington, D. C. 20390	
Attn: H. W. Carhart	1
Picatinny Arsenal Dover, New Jersey 07801	
Attn: Chief, Liquid Propulsion Laboratory	1
Aerojet-General Corporation P. O. Box 296 Azusa, California 91703	
Attn: Librarian	1
Aerojet-General Corporation 11711 South Woodruff Avenue Downey, California 90241	
Attn: F. M. West, Chief Librarian	1

		Copies
Aerojet-General Corporation P. O. Box 1947 Sacramento, California 95809		
Attn:	Tech. Library 2484-2015A	1
	K. R. Collins	1
	R. Jones	1
	J. Farquhar	1
	F. Viteri	1
	M. Huppert	1
	B. Lindley	1
	L. Severud	1
Aerospace Corporation P. O. Box 95085 Los Angeles, California 90045		
Attn:	Library-Documents	1
Allis Chalmers Mfg. Co. Box 512 Milwaukee, Wisconsin 53201		1
Battelle Memorial Institute 505 King Avenue Columbus, Ohio 43201		
Attn:	Report Library Room 6A	1
Bell Aerospace Company Box 1 Buffalo, New York 14240		
Attn:	Technical Library	1
	M. Messina	1
The Boeing Company Aero Space Division P. O. Box 3707 Seattle, Washington 98124		
Attn:	Ruth E. Peerenboom, Library Processes Sup. (1190)	1
Brown Engineering Co., Inc. Research Park Huntsville, Alabama 35807		
Attn:	Library	1

		Copies
Chrysler Corporation Space Division New Orleans, Louisiana 70150		
Attn:	Library	1
Curtiss-Wright Corporation Wright Aeronautical Division Woodridge, New Jersey 07075		
Attn:	Library	1
Fairchild Stratos Corporation Aircraft Missiles Division Hagerstown, Maryland 20740		
Attn:	Library	1
The Franklin Institute Research Laboratories Benjamin Franklin Parkway Philadelphia, Pennsylvania 19103		
Attn:	Library	1
The Garrett Corporation AiResearch Manufacturing Co. 9851 Sepulveda Blvd. Los Angeles, California 90009		
Attn:	Library	1
General Dynamics/Astronautics P. O. Box 1128 San Diego, California 92112		
Attn:	Library and Information Services (128-00)	1
General Electric Company Flight Propulsion Laboratory Dept. Cincinnati, Ohio 45215		
Attn:	D. Suichu	1
	P. R. Gliebe	1
General Motors Corporation Allison Division P. O. Box 24013 Indianapolis, Indiana 46206		
Attn:	Library	1

	Copies
Grumman Aircraft Bethpage Long Island New York 11714	
Attn: Library	
Hydronautics, Incorporated Pindell School Road Laurel, Maryland	1
IIT Research Institute Technology Center Chicago, Illinois 60616	
Attn: Library	1
Lockheed Missiles & Space Company Propulsion Engineering Division (D. 55-11) 1111 Lockheed Way Sunnyvale, California 94087	1
Lockheed Propulsion Company P. O. Box 111 Redlands, California 92374	
Attn: Library	1
Marquardt Corporation 16555 Saticoy Street Box 2013 - South Annex Van Nuys, California 91404	
Attn: Library	1
McDonnell Douglas Aircraft Corporation P. O. Box 516 Lambert Field, Missouri 63166	
Attn: Library	1
McDonnell Douglas Astronautics Company Western Division 5301 Bolsa Avenue Huntington Beach, California 92647	
Attn: Library	1

		Copies
Pesco Products Division of Borg-Warner Corp. 24700 N. Miles Road Bedford, Ohio 44146		1
Rocketdyne, A Division of North American Rockwell Corporation 6633 Canoga Avenue Canoga Park, California 91304		
Attn:	Library, Dept. 596-306	1
	J. Hale	1
	K. Rothe	1
	R. K. Hoshide	1
	J. A. King	1
	J. K. Jacobsen	1
Rocket Research Corporation 520 South Portland Street Seattle, Washington 98108		1
Sundstrand Corporation Hydraulics Division Rockford, Illinois 61101		1
Sundstrand-Denver Industrial Products Group 2480 W. 70th Street Denver, Colorado 80221		1
TRW Systems One Space Park Redondo Beach, California 90278		
Attn:	STL Tech. Lib. Doc. Acquisitions	1
United Aircraft Corporation Corporation Library 400 Main Street East Hartford, Connecticut 06118		
Attn:	Library	1
United Aircraft Corporation Pratt & Whitney Fla. Res. Development Center P. O. Box 2691 West Palm Beach, Florida 33402		
Attn:	Library	1
	J. Hill	1

	Copies
United Aircraft Corporation United Technology Center P. O. Box 358 Sunnyvale, California 94088	
Attn: Library	1
Worthington Corp. Advanced Products Division Harrison & Worthington Avenues Harrison, New Jersey 07029	1
Dr. George F. Wislicenus 4641 E. Coronado Drive Tuscon, Arizona 85718	1
California Institute of Technology Pasadena, California	
Attn: Dr. A. Acosta	1
Iowa State University Ames, Iowa	
Attn: Dr. George Serovy	1
Pennsylvania State University State College, Pennsylvania	
Attn: Dr. B. Lakshminarayana	1
Scanivalve Corp. P. O. Box 20005 San Diego, California 92120	
Attn: J. C. Pemberton	1